Small-scale Instability Driven Electron Transport in Hall Thrusters

by

Zachariah A. Brown

A dissertation submitted in partial fulfillment
of the requirements for the degree of
Doctor of Philosophy
(Aerospace Engineering)
in The University of Michigan
2024

Doctoral Committee:

Associate Professor Benjamin A. Jorns, Chair
Professor John E. Foster
Professor Alec D. Gallimore
Professor Christopher Limbach

Zachariah A. Brown
brownzac@umich.edu

ORCID iD: 0000-0001-8349-0153

To my family.

Acknowledgements

I've bounced probably 20 different versions of this acknowledgements around with nothing coming out quite right. There are far too many people to thank properly for enabling me to reach this point in my life, but as the submission deadline encroaches upon me in these waning hours I think it best to keep this short, sweet, and to the point. My time at Michigan was an adventure full of enjoyment, stress, great friendships, long nights, and countless memories. The path to finishing my degree would not have been possible without the support of great friends, labmates, mentors, and frankly everyone in the Aero department. Everyone at PEPL means the world to me and without them it wouldn't have been possible for me to succeed. As cliche as it is, PEPL really was like a second home for me during my time there. In particular, I would not have survived my years at Michigan without the enduring friendship of Shadrach Hepner, Joshua Woods, Matt Byrne, and Ben Wachs. Our shared suffering will forever bond us. Lastly, I would like to thank everyone, and in particular my patient advisor Dr. Benjamin Jorns, for putting up with all my shenanigans.

Table of Contents

List of Figures

Figure

ABSTRACT

There is an increasing demand for efficient electric propulsion technologies for orbital station keeping and deep-space missions. Hall effect thrusters, as a leading form of electric propulsion, exhibit superior propellant efficiency through high specific impulse values, resulting in significant reductions in mission costs and propellant mass. This has led to their extensive utilization for spacecraft applications, including orbit-raising maneuvers, attitude control, and interplanetary propulsion. However, despite their widespread use the underlying physics governing the operation of Hall thrusters are not fully understood. Due to the lack of understanding of key physical processes, currently Hall thrusters cannot be readily simulated, and the development of new systems heavily relies on costly and time-consuming experimental testing.

Our research aims to delve into the first principles of Hall thruster physics and address several deficiencies in our understanding that impede predictive simulations. Notably, the transport of electrons across the magnetic field lines of Hall thrusters is orders of magnitude greater than predicted by simple fluid models. The Hall thruster modeling community has recently reached a consensus that plasma turbulence is the most likely cause of this anomalous cross-field transport. In this work, we experimentally validate the role of electron drift instability (EDI) in electron transport within Hall thrusters. Despite widespread consensus on its significance, this topic has predominantly relied on numerical simulations with limited experimental validation. These simulations exhibit notable disparities concerning the formation of the EDI, relevant oscillation frequencies and wavelengths, and the extent of the resulting electron transport. Such uncertainties impede the development of precise and universally

applicable low-fidelity models that accurately represent electron transport. To address these ambiguities, we employ experimental methodologies, including the direct measurement of EDI using electrostatic probes inserted into a Hall thruster. These probes measure high-speed plasma density oscillations, and subsequent spectral analyses of these measurements offer insights into the dispersion relation of the EDI, its growth and saturation patterns, and the level of induced electron transport. Our measurements identified the presence of plasma waves characteristic of the electron drift instability. Furthermore, through bispectral analysis, an inverse energy cascade was identified whereby the EDI initially grows following its linear dispersion relation at discrete resonance frequencies. Subsequently, the resonances couple together, transferring energy from high frequency and small wavelength to low frequency and long wavelength. This energy cascade occurs as the waves propagate downstream of the Hall thruster, where eventually most of the wave energy belongs to the long-wavelength component. These experimental findings serve as validation for several simulation and modelling effort the first proposed these mechanisms. Moreover, we utilized these measurements of plasma wave properties to calculate the wave-driven anomalous cross-field transport and validated these calculations through laser-based measurement of the true cross-field transport levels. This provides the first experimental proof that the EDI is the mechanism controlling electron transport in Hall thruster plasma plumes. Overall, this investigation enhances the understanding of the EDI's characteristics, advances electron transport models, and brings the field one step closer to predictive Hall thruster modeling.

CHAPTER I

Introduction

1.1 Problem Statement

In the last few decades, there has been growing interest in electric propulsion for use in spacecraft for orbital station keeping and deep-space missions. As the demand for high-performance space missions continues to rise, electric propulsion technologies like Hall thrusters are increasingly being utilized for their remarkable capabilities. One key aspect that sets electric propulsion apart from traditional chemical propulsion systems is the ability to achieve high specific impulse values, which translates to a more efficient use of propellant mass. This results in significant reductions in overall mission costs and propellant mass fractions, making electric propulsion particularly well-suited for long-duration satellite station-keeping and ambitious deep-space exploration endeavors.

One of the key driving electric propulsion technologies pushing forward space flight is the Hall effect thruster. Hall thrusters have gained considerable attention within the electric propulsion domain due to their unique combination of operational simplicity, scalability, and robust performance. These thrusters operate by ionizing a propellant gas, typically xenon, within a magnetic field, and then accelerating the resulting ions to generate thrust. The magnetic field configuration used in modern Hall thrusters leads to efficient ion acceleration and minimal wall erosion, thereby

promoting extended thruster lifetimes and high thrust-to-power ratios. As a result, Hall thrusters have become an attractive choice for a broad range of satellite and spacecraft applications, including orbit-raising maneuvers, attitude control, and interplanetary propulsion.

Hall thrusters have been in use since the 1970s but recently have become the workhorse of electric propulsion systems with over several thousand currently in orbit, mostly part of SpaceX's Starlink constellation, providing station keeping and orbit-raising capabilities on both LEO and GEO satellites. These systems are also being implemented on long-duration deep-space missions, such as NASA's Psyche mission[80], and could potentially be used for human transport to Mars. However, the widespread adoption of Hall thrusters has also highlighted the critical need for a deeper understanding of the underlying physical processes governing their operation. In particular, the development of accurate predictive models is essential for refining thruster designs, optimizing performance parameters, and ensuring mission success and reliability. The ability to accurately model Hall thruster physics would enable engineers and mission planners to make informed decisions when selecting and implementing propulsion systems, ultimately leading to more efficient and cost-effective space missions. However, due to the lack of understanding of key aspects of the underlying physics, currently, the development of new Hall thruster systems heavily relies on experimental testing.

Generally, this experimental testing is a long and costly process, and there are significant uncertainties regarding how well ground testing represents the on-orbit environment and differences in operation[17, 77, 18]. In the development cycle of adjacent fields, such as aircraft and rockets, there is significant use of simulations that can reliably predict performance and operation from first principles and geometry design, thereby rapidly accelerating the time between design iterations. While there is a strong desire for these same capabilities in Hall thruster development, the

lack of fundamental understanding about the underlying physics has thus far prevented the use of any fast and reliable predictive models. Typically, Hall thruster models used in testing new designs employ low-fidelity fluid-based codes due to their low computation cost and high speed. These low-fidelity codes are similar in principle to the CFD programs used in aerodynamics, but electric and magnetic forces must be considered. These codes, such as Hall2DE[75], are capable of reproducing many key features of Hall thruster operation, but only through the use of adjustable parameters determined through experimental data. These empirically determined parameters are needed because the fluid model does not properly predict the transport of electrons across magnetic field lines, the so-called "anomalous electron transport" problem. The origin of the anomalous transport is thought to come from kinetic effects that are impossible for fluid codes to resolve and can only be observed with higher-fidelity codes such as particle-in-cell (PIC) or direct kinetic simulations. While there are many PIC simulations that have been able to accurately resolve cross-field electron transport, due to the significantly higher computational power required for these high-fidelity simulations, they often only operate in 1D or 2D and require long run-times[93, 84]. Despite their inability to model a full thruster geometry for use in predictive design, these high-fidelity codes provide insight about the underlying physics governing electron transport. The increased understanding of the underlying physics is being used to create lower-fidelity models that capture the relevant kinetic effects but can be used in a fluid-based framework[71].

Despite several recent advancements, an adequate model for electron transport in Hall thrusters remains elusive. Classically, the cross-field transport due to particle collisions should scale with the inverse of the squared magnetic field ($1/B^2$), but numerous experiments have demonstrated that this scaling does not apply to Hall thrusters[7]. Various theories have been proposed to explain the phenomenon of anomalous electron transport in Hall thrusters, each attempting to shed light on the

intricate mechanisms responsible for the observed behavior. Among these theories, Bohm diffusion, particle-wall interactions, and instability-driven transport stand out as the most prominent explanations.

Bohm diffusion is a theoretical model that has been widely considered in the context of anomalous electron transport in many E×B devices such as Hall thrusters. Originally formulated to explain plasma behavior in fusion devices, Bohm diffusion predicts the cross-field transport is enhanced due to small-scale thermal fluctuations and overall results in a weaker $1/B$ scaling compared to particle collision-based transport. In the case of Hall thrusters, the Bohm diffusion coefficient has been considered in many studies. While it is often found to be in reasonable agreement with experimental observations in certain regions of the thruster plume, it thus far has not been able to accurately reproduce electron transport[35, 50, 62].

Particle-wall interactions represent another proposed mechanism for anomalous electron transport in Hall thrusters. In this theory, the presence of nearby walls in the thruster discharge chamber influences the behavior of charged particles, leading to enhanced electron transport rates[53]. The increased proximity of electrons to the walls results in more frequent collisions, which in turn facilitate the diffusion of electrons across the magnetic field. While particle-wall interactions undoubtedly contribute to electron transport in Hall thrusters, their relative importance in the overall transport process is not yet fully understood, and it remains unclear whether they can solely account for the observed anomalous behavior.

The growing consensus in the community points toward the enhanced transport being driven by small-scale instabilities present in the Hall thruster plume, and in particular an instability known as the electron drift instability (EDI)[48]. Much of the research surrounding the EDI and its impact on electron transport has focused on numerical methods, and there have been extremely limited experimental results demonstrating the presence of the EDI in Hall thrusters and its influence on transport.

Furthermore, despite the extensive numerical research performed over the last two decades, there remains a lack of consensus about many aspects of the EDI. The focus of this work, which we outline in the next section, is to resolve several uncertainties about the EDI in Hall thrusters through experimental techniques. With experimental data, various models can be more accurately constructed and may finally produce a fully predictive Hall thruster simulation.

1.2 Objectives

Our primary objectives for this work are to justify, or reject, the role of the EDI in Hall thruster electron transport. As discussed in the previous section, despite the wide-spread agreement concerning the importance of the EDI on Hall thruster operation most of these conclusions are borne from numerical simulations and have limited experimental validation. Furthermore, while nearly all recent simulations demonstrate the formulation of the EDI and its impact of cross-field transport, there remains many disagreements between simulations as to how the EDI forms, what oscillation frequencies and wavelengths are most important to the instability, and the magnitude of any induced electron transport. This uncertainty regarding the exact nature of the EDI limits the ability to produce accurate and thruster agnostics low-fidelity models that model electron transport. Our work aims to address several of the ambiguities through experimental techniques. This includes direct measurement of the EDI using electrostatic probes inserted into a Hall thruster to measure high-speed plasma density oscillations. Through various spectral analysis methods we use these plasma oscillation measurements to infer the EDI dispersion relation (how the EDI behaves as a function of wavelength), how the EDI grows and saturates, and the induced electron transport levels.

1.3 Organization

This thesis is organized as follows, In Chapter II, we provide an overview of electric propulsion and Hall thruster operation. We also present a framework for cross-field electron transport and a review of previous modeling efforts. In Chapter III, we outline the experimental techniques we used to study the EDI and electron transport in Hall thrusters. We provide details about the specific thruster used during experimentation, the test facility, and the probing methodology, and we review the main analysis techniques applied to our experimental data. Chapter IV details the results of an experimental campaign to measure the dispersion relation of the EDI in a Hall thruster plume. This information is used to address several of the uncertainties between various simulations about the nature of the EDI in Hall thrusters. In Chapter V, we apply an advanced bispectral analysis technique with plasma oscillation measurements that are used to determine fundamental properties of the EDI, such as the growth rate and non-linear energy exchange. These properties are then used to infer the electron transport induced by the EDI. Finally, in Chapter VI, we summarize our findings and provide possible avenues for future research.

CHAPTER II

Hall Thruster Operation

2.1 Overview

In this chapter, we first provide an overview of the role of electric propulsion in space propulsion systems. Next, we introduce the Hall thruster and discuss its core operating principles. We highlight the key research topics surrounding Hall thruster technologies, with a specific focus on Hall thruster modeling and simulation. We then present a framework for studying cross-field electron transport in Hall thrusters. We review previous attempts to explain the observed anomalous transport and the current prevailing theories. Finally, we discuss the specific gaps in knowledge that this work addresses.

2.2 In-Space Propulsion

All current space propulsion systems operate on the same fundamental principle of ejecting a reaction mass to generate a change in momentum by Newton's third Law. Therefore, the capabilities of any propulsion system are governed by how much reaction mass can be utilized and how fast it is launched. This basic relationship is

represented by Tsiolkovsky's rocket equation:

$$\frac{m_i}{m_f} = e^{\Delta V/u_{ex}}. \tag{2.1}$$

Here, m_i is the initial spacecraft mass, m_f is the final spacecraft mass after using its propellant, Δv is the change in velocity of the spacecraft, and v_{ex} is the velocity of the ejected propellant mass. Often, the exhaust velocity is defined in terms of specific impulse: $I_{sp} = v_{ex}/g_0$, where g_0 is the Earth's gravitational acceleration. This simple equation governs the design goals of all space propulsion systems. For a given mission that requires a fixed ΔV and maximum system mass—payload plus propellant mass—a higher specific impulse yields better ratios of payload mass to propellant mass. Due to the exponential relation in Eq. 2.1, it is extremely desirable to maximize the specific impulse of any propulsion system. For rocketry, the specific impulse is typically limited to the range of 200-400s due to the chemical energy density of the propellant/fuel. This results in a situation where most of the rocket's mass is taken up by the propellant, and only a small fraction of the rocket is delivered to orbit. Electric propulsion systems have the advantage of generating specific impulses of 1000-10000 (or higher), and allow for significantly more payload mass. From this perspective, electric propulsion systems are functionally more 'fuel efficient' and need less gas to perform the mission as compared to rockets. However, this efficiency is only one half of the picture. Despite the high specific impulse of electric propulsion systems, they are not capable of launching from Earth as they generate vastly insufficient thrust to escape Earth's gravity.

The thrust of a propulsion system is given by the product of the propellant mass flow rate $\dot{m}$ and exhaust velocity

$$T = \dot{m} u_{ex} \tag{2.2}$$

While electric propulsion systems generate high exhaust velocity, they are typically limited to thrusts measured in millinewtons. This limitation primarily stems from the restricted power available to the electric propulsion system. In rockets, the propellant doubles as the power supply where fuel and oxidizer combust to generate thermal energy. This energy is then converted into the kinetic energy of the reaction products by a nozzle to generate thrust. In electric propulsion systems, the propellant is typically composed of inert noble gases that only serve as the reaction mass. An external power source is needed to ionize the propellant and then electrostatically (or electromagnetically) accelerate ions to produce thrust. Rocket propellant is very energy-dense, and when the mass flow is high, the engines can provide enormous power output, if only for a limited time. For example, the Saturn V first-stage engine generates power on the order of gigawatts, but only operates for a few minutes. Most systems that use electric propulsion generate power using solar energy, and typically these systems only have power on the order of hundreds of watts to low kilowatts dedicated to the propulsion system. Compared to rockets, electric propulsion simply doesn't have the power to generate high thrust. While this does restrict electric propulsion from providing launch system capabilities, once in orbit, the drawbacks of low thrust are often outweighed by the increase in payload mass from high specific impulse.

In orbit or deep-space missions, the trade-off centers on how quickly the mission needs to be completed (thrust) and how much propellant can be brought to the mission (specific impulse). Typically, these missions have durations measured in years where electric propulsion systems can provide thrust over the entire mission versus combustion systems that only provide thrust on the order of minutes to hours. This allows for electric propulsion to be competitive propulsion systems even with their low thrust. Furthermore, the high specific impulse of electric propulsion systems provides significant economic benefits. Due to the high cost of launching mass into

orbit (>5000/kg) and limited overall launch payload mass, there is a strong incentive to limit the portion of spacecraft mass that will be used as propellant for in-orbit propulsion. The high specific impulse exhibited by electric propulsion allows for a significant increase in useful payload mass compared to combustion systems, or reduces the overall system cost by reducing the propellant mass required to be launched into orbit.

Electric propulsion systems also feature a much wider range of operating conditions that allow easy conversion between thrust and specific impulse depending on the mission requirements. The basic principle of electric propulsion thrusters is the acceleration of ionized gas by electric and/or magnetic forces. Several examples of modern electric propulsion technologies are found in Ref. [42], but for the purpose of this discussion, we shall limit our focus to two of the most widely utilized technologies: the gridded ion thruster and Hall effect thruster. Although we shall overlook differences in how ions are generated for now, both systems generate force through the acceleration of ionized gas with electric fields. Gridded ion thrusters use a pair of closely spaced semi-transparent electrode grids with a strong voltage applied between the grids. This voltage is often referred to as the discharge voltage V_d. The applied voltage generates a strong local electric field between the grids and any ions that encounter this electric field will be accelerated to high velocity:

$$u_{ex} = \sqrt{\frac{2qV_d}{m_i}} \tag{2.3}$$

where q is the fundamental electric charge and m_i is the ion mass. Typically voltages are on the order of 10s of kilo-volts and result in ion velocities over 100 km/s with a specific impulse of 10,000 s. The power of this system is governed by

$$P = \frac{\dot{m}u_{ex}^2}{2} = \frac{\dot{m}qV_d}{m_i}. \tag{2.4}$$

and the thrust by:

$$T = \dot{m}\sqrt{\frac{2qV_d}{m_i}} \tag{2.5}$$

For a fixed system power, gridded thrusters, and generally all electric propulsion systems, have the capability of increasing specific impulse by raising the discharge voltage and lowering the mass flow rate, but at the expense of reduced thrust. Historically, gridded ion thrusters have been used where very high specific impulse is needed, and low thrust levels are acceptable. Due to the physics of generating the electric field (see Ref. [42]), gridded ion thrusters have a maximum space-charge limited current and, for a given discharge voltage and grid size, a maximum possible thrust.

Hall thrusters are governed roughly by the same principles as gridded ion thrusters, where thrust is generated by accelerating ions across an applied discharge voltage. However, to first order, Hall thrusters do not have the same thrust limitations as gridded thrusters. Hall thrusters are not space-charge limited and can output more thrust at low discharge voltage and size while still achieving desirable levels of specific impulse (approximately 1000-3000s). Furthermore, these devices typically have simpler designs with fewer components and lower risk of faults. For these reasons, among others, Hall thrusters have quickly become the most widely used thrusters for in-space propulsion. Despite these successes, as we discuss in the next section, the fundamental physics governing Hall thruster operation are not fully understood. While this limitation has not impeded their adoption, it does limit the ability to simulate and rapidly iterate new designs. Most Hall thruster development is driven through experimental methods which are both expensive and time-consuming.

2.3 Hall Thruster Overview

In this Section, the Hall effect thruster, also known as stationary plasma thrusters (SPT) or thruster with anode layer (TAL), is introduced and its core operation ex-

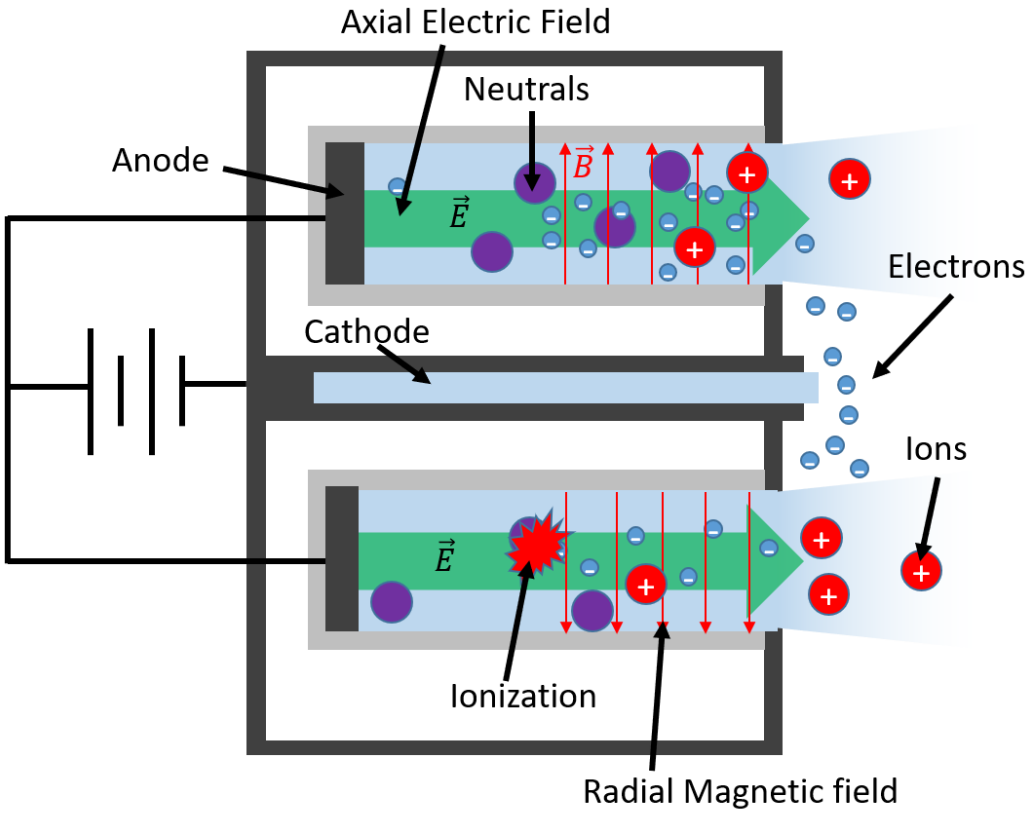

Figure 2.1: Overview of Hall Thruster operation.

plained. We start by providing an overview of the design of these thrusters including the core components. Then we review their principle of operation and thrust generation mechanisms. Finally, we outline several of the current research topics important to these devices, in addition to the main focus of this work that centers on electron transport.

The Hall thruster consists of only a few core components (see Fig.2.1 and Fig.2.2). An electrical circuit, consisting of a cylindrical anode (i) and downstream cathode (ii), uses an applied potential difference between the anode and cathode to accelerate ions and generate thrust. The cathode also serves as an electron source for ionization and for keeping the spacecraft electrically neutral. A magnetic circuit (iii) is used to create a magnetic field radially across the cylindrical channel to confine electrons and prevent them from reaching the anode, thus increasing electron residence time

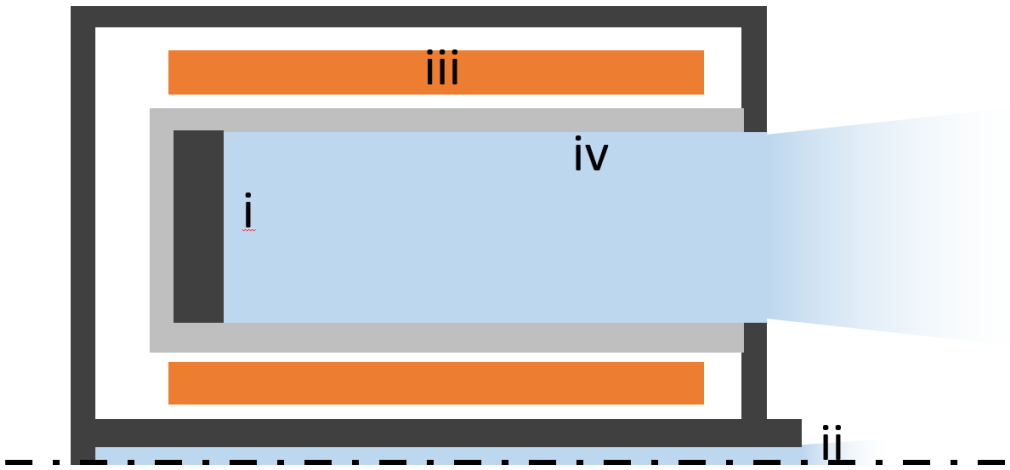

Figure 2.2: Cross-sectional view of a Hall thruster highlighting the primary components. i: Gas distribution/anode, ii: Hollow Cathode, iii: Magnetic circuit, iv: Discharge channel walls.

for efficient ionization. Lastly, the channel walls (iv) isolate the plasma from the thruster.

The anode can become very hot during operation, in excess of several hundred degrees, and is typically constructed out of a high-temperature metal such as stainless steel. This annular anode is hollow and features a series of baffles and small orifices facing the channel of the Hall thruster. In this way, the anode doubles as a gas distributor for the propellant in addition to supplying voltage to the system. In a similar manner, the hollow cathode flows a small fraction of the propellant, typically less than 10%, which is ionized using seed electrons thermally emitted from a low-work function material inside the cathode and the potential applied between the cathode and either the anode or an electrode just downstream of the cathode, known as the keeper. The potential at the keeper is only applied at thruster startup.

The magnetic circuit is typically create using two methods. For large Hall thrusters, typically $>$ 1kW, the field is generated by a pair of annular electromagnets. For lower power systems the power draw of the electromagnets could become a significant portion of the overall system and generally these smaller Hall thrusters use permanent magnets to create the field shape. Although common to both designs is the use of

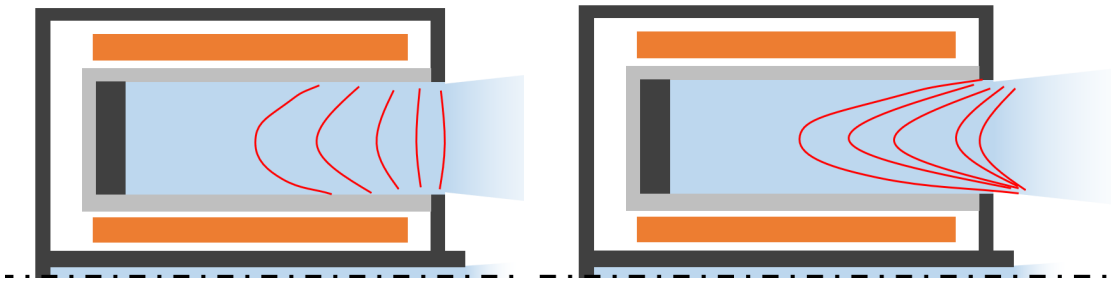

Figure 2.3: Example magnetic field shapes for unshielded (a) and shielded (b) Hall thruster designs

cylindrical ferromagnetic components behind the Hall thruster channel walls. These components assist in shaping the magnetic field to achieve a field such as the one in Fig 2.3a. This field shape representative of historical Hall thruster designs where main objective was to create a radial field across the channel. Recent advancements in Hall thruster design have lead to so-called 'shielded' magnetic field topologies such as those in Fig. 2.3b[25, 26, 49]. The magnetic field in shielded designs curves along the edge of the channel walls deep in the channel before wrapping out along the opposite channel face. The field shape shields the channel walls for the plasma and eliminates the major erosion and failure mechanism for these devices[27].

Now, with a basic overview of the major Hall thruster components, we return to a more in-depth discussion of the Hall thruster operating principles. A potential difference applied between the anode and cathode creates an electric field that attracts electrons emitted from the cathode to travel upstream toward the anode, as depicted in Fig. 2.1. Electrons collide with neutral gas, typically Xenon or Krypton, emitted from the anode, and generate ions that are accelerated across the potential difference to generate thrust. The radial magnetic field is applied with sufficient field strength to magnetize the electrons such that they are trapped in $E \times B$ drift, moving azimuthally around the channel. The magnetic field strength is tailored so that only the electrons are magnetized, while the much more massive ions are unmagnetized and travel out

of the thruster solely due to electric forces. By trapping the electrons in this $E \times B$ Hall current, from which the device gets its name, the electron current reaching the anode is drastically reduced, lowering the necessary system power to continue the ionization process. However, some electron current does make it to the thruster due to electrons being knocked across field lines during ionization collisions. Additionally, as the ions travel out of the thruster, some electrons follow from the cathode, so the thruster remains electrically neutral.

While this description generally captures the operating principle of Hall thrusters, there are several important nuances not addressed by this simplified view. Perhaps most importantly, the electric field generated by the discharge is not evenly distributed across the channel as shown in Fig. 2.1. The electric field is concentrated at the exit plane of Hall thruster where most acceleration occurs across only a few centimeters, see Fig.2.4. Generally, the electric field at the physical electrodes are weak and unlike gridded ion thrusters the thrust generation mechanism cannot be viewed reaction electric forces on the physical thruster. As highlighted in Ref. [42], the force mediation occurs via the electromagnetic Lorentz force created by the electron Hall current and the thruster's magnetic field. Despite this nuance, Hall thrusters are still considered electrostatic devices due to the ion acceleration, which can be thought of as a reaction force to keep the electrons stationary.

Despite the addition of electric and magnetic forces, it might seem straightforward to model a Hall thruster in a fluid simulation similar to CFD in aerodynamics, following these principles. However, this is not the case. The Hall thruster hosts numerous instabilities[24] that complicate the situation. For example, due to differing rates of ions leaving the thruster and the neutral gas replenishing it, a predator-prey-like instability occurs[35, 4, 28]. This leads to the thruster oscillating between periods of high and low current, typically on the order of 10kHz. The various oscillations and instabilities present in Hall thrusters play a crucial role in both thruster opera-

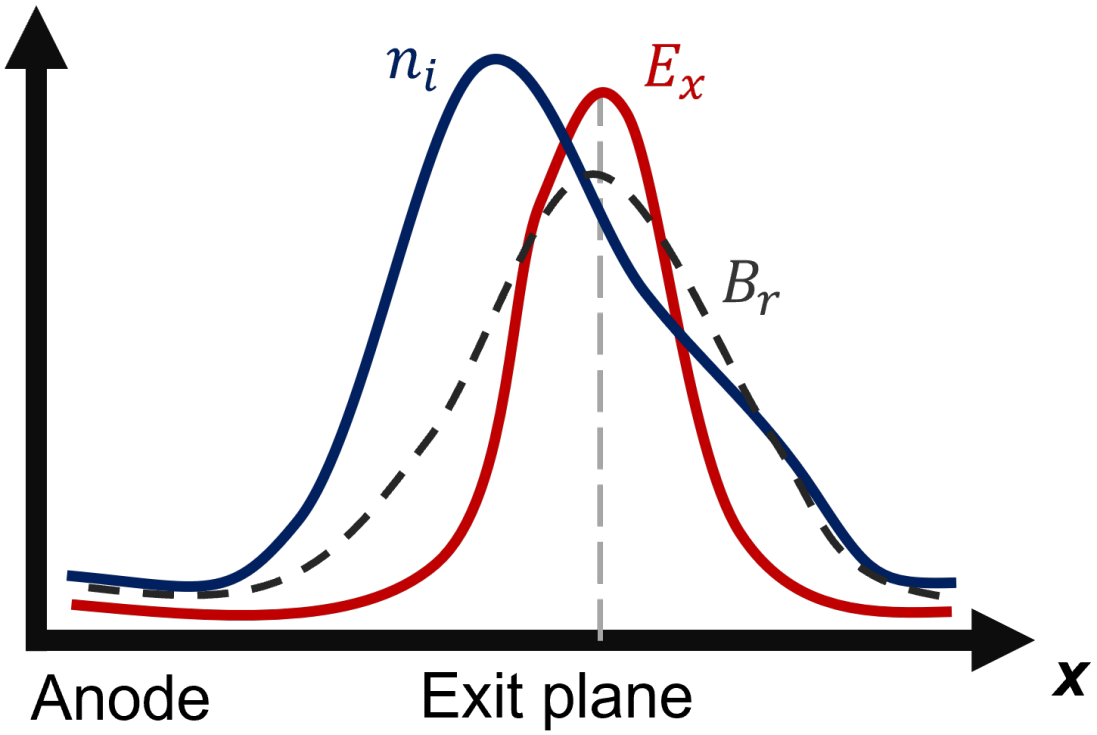

Figure 2.4: Example distribution of plasma parameters inside a Hall thruster discharge channel.

tion and performance. Many of these aspects of Hall thruster operation have been captured by numerical simulations capable of modelling the thruster geometry, but with one major exception: the transport of electrons across magnetic field lines. As discussed above, classically, electrons travel across field lines due to particle collisions, but experimental measurements have shown that the axial electron current is orders of magnitude larger than could be explained by collisions[54]. As we discuss in depth in the next section, the leading theory for this behavior is the presence of a small-scale instability, the electron drift instability (EDI), which acts as an anomalous drag force. The origin of this instability is kinetic in nature; it requires resolving the electron population as individual particles instead of as a bulk fluid. While there are simulation techniques—such as particle-in-cell—that can resolve the required level of detail such that the instability is observed along with enhanced anomalous electron transport, these high-fidelity codes are extremely computationally expensive. They either take too long or only simulate limited dimensions of the Hall thruster geometry, making them unsuitable for rapid iterative design in a new thruster development cycle. While the timescale of plasma instabilities is often on the scale of microseconds, Hall thrusters must be designed to operate for thousands of hours. Increasingly, there is a desire to develop reduced-fidelity simulations that capture anomalous transport due to instabilities through simplified models that predict the instability's effect based on local bulk plasma properties. In pursuit of this goal, significant research efforts have focused on analyzing the instability using simulations, but there has been little experimental verification of both the instability and its impact on transport. Chapters V and VI cover our experimental efforts to address these concerns. However, before that, the next section will present a model for electron transport in a Hall thruster discharge.

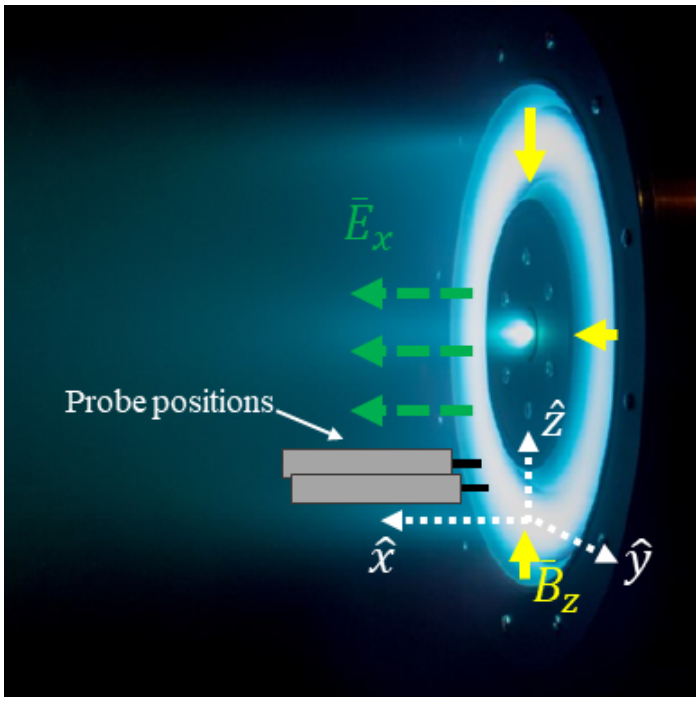

Figure 2.5: Coordinate system used for modelling cross-field transport in a Hall thruster.

2.4 Electron Transport Model

In Hall thrusters electron transport generally describes the process where electrons are extracted from the cathode and travel upstream toward the anode. In an ideal situation electrons would be perfectly constrained to magnetic field lines and only one so-called 'golden electron' would be needed from the cathode to start the ionization process. Taking into account particle collisions—electrons with ions, neutrals, or walls—there would an electron current toward the anode as the electron loses energy from the collision as drops into an $E \times B$ orbit closer to the anode. This collision based framework of electron mobility across magnetic field lines is often referred to as "classical transport". Following the classical derivations of cross-field transport—such as those found in [21]—the electron transport process can be described by an equation of motion for electrons in an axial electric field along the 'x-axis' ($\vec{E} = E_x\hat{\vec{x}}$)

and a radial magnetic field along the 'z-axis'($\vec{B} = B_r\hat{\vec{z}}$):

$$m_e n \frac{d\vec{v_e}}{dt} = qn(\vec{E} + \vec{v_e} \times \vec{B}) - \nabla p - m_e n_e \nu_c \vec{v} = 0. \tag{2.6}$$

This equation describes the change in momentum for electrons. In order, the terms on the right hand side represent the electric force, Lorentz force, electron pressure (∇p), and force due to collisions at frequency ν_c. Following the typical procedure for determining motion across field lines we ignore electron inertial (assume the left-hand-side is zero) and the pressure can be describe an equation of state where temperature is assumed constant $\nabla p = k_B T_e \nabla n$). Solving this equation for electron particle flux across field lines ($\Gamma_{e\perp} = n v_{e\perp}$) yields:

$$\Gamma_{e\perp} = n_e \mu_\perp \vec{E}_\perp - D_\perp \nabla n. \tag{2.7}$$

Here $\mu_\perp$ and $D_\perp$ are the cross-field mobility and diffusion coefficients respectively. These are given by

$$\mu_\perp = \frac{\mu}{1 + \omega_{ce}^2/\nu_c^2} \tag{2.8}$$

$$D_\perp = \frac{D}{1 + \omega_{ce}^2/\nu_c^2} \tag{2.9}$$

where $\omega_{ce} = eB/m$ is the electron cyclotron frequency and μ and D are the classical mobility and diffusion coefficients defined as

$$\mu = \frac{e}{m_e \nu_c} \tag{2.10}$$

$$D = \frac{k_B T_e}{m_e \nu_c} \tag{2.11}$$

Physically, this equation demonstrates that electrons travel across field lines due to the axial electron field and density gradients, but are impeded by the magnetic

field and enhanced by collisions. This dependence on magnetic field strength versus collisions is reflected in the term ω_{ce}/ν called the Hall parameter Ω. In the ideal case, neglecting collisions, both transport coefficients go to zero and there no cross-field electron current. In terms of Hall thruster design, the magnetic field is sized such that the Hall parameter is large: $\Omega^2 >> 1$. This corresponds to the situation where the electrons make many cyclotron orbits in between collisions, if this were not the case then collisions would lead to a demagnetization of the electrons. In this limited the cross-field diffusion and mobility coefficients can be expressed as

$$\mu_\perp \approx \frac{m_e \nu_c}{eB^2} \tag{2.12}$$

$$D_\perp \approx \frac{k_B T_{eV} m_e \nu_c}{e^2 B^2} \tag{2.13}$$

This is the origin of the classical $1/B^2$ scaling originally predicted for electron transport in Hall thrusters. While this model is a simplistic way to describe Hall thruster operation and infer some design guidelines, it was quickly discovered that Hall thrusters exhibit a particle flux of electrons across magnetic fields that is orders of magnitude larger than could be explained by Equation 2.7[7, 54]. Much of the research on Hall thrusters has focused on trying to explain this so-called 'anomalous transport'. Most theories can be divided into two groups: wall interactions and turbulence-driven transport. While the major focus of this thesis centers around the turbulence transport model, we note that there have been many investigations into wall-interactions and their effect on cross-field transport[94, 96, 22, 23]. Generally, these research efforts have shown that while wall-interactions have a role in electron transport, particularly inside the channel of the thruster, they cannot fully model the observed transport. Considering that recent magnetically-shielded Hall thruster designs have acceleration zones outside of the channel[29], the growing consensus is that turbulence-induced mechanisms primarily drive the anomalous electron transport[48]. However, both wall

collisions and wave-driven turbulence have proven to be difficult to accurately represent in fluid codes/models. Ideally, an additional term could be added to Equation 2.7 that depends only on macroscopic properties, such as temperature and density, but these anomalous effects have been shown to be generally kinetic in nature and would require particle-in-cell (PIC) simulations or direct-kinetic (DK) simulations of the Boltzmann equation to properly evaluate anomalous transport. Therefore, there are generally two paths for numerically investigating electron transport that feed back on each other. The first path is to take the difficult and time-consuming route of PIC/DK simulations, often in vastly simplified geometry or system, to analyze the physics driving anomalous transport. Next, with a hopefully greater understanding of the first principles physics, a reduced fidelity model is generated that captures the relevant anomalous transport dynamics in a way that can be evaluated by a fluid model. This process has been ongoing for several decades now with significant advances, but the final result of a predictive Hall thruster simulation model has remained elusive[93]. We briefly review the previous body of work advancing the state of electron transport models in Hall thrusters.

2.4.1 Simulation and Modeling Efforts

The general methodology for including higher-order effects for electron transport in fluid models focuses on evaluating an anomalous collision frequency (ν_{AN}). The anomalous collision frequency would be a function of macroscopic properties that can then be added to the classical term in the fluid equations to calculate cross-field transport: $\nu = \nu_c + nu_{AN}$. Later in this chapter, we will present an example derivation of how azimuthal instabilities can be represented by an anomalous collision frequency, but the same principle applies regardless of the primary physical mechanism: the higher-order effects yield an additional path for electrons to lose momentum. Hence the common reduction to an effective collision frequency.

A logical next step to model a higher collision frequency than could be predicted by particle-particle collisions would be to include collisions with the thruster channel walls. This effect is often referred to as near-wall conductivity and was first proposed and studied heavily by Morozov during early Hall thruster development[53]. Although, the situation is more complicated than solely considering ballistic collisions with the walls because of stealth effects and secondary electron emissions(SEE)[4, 38]. Often, due to simplicity and speed these effects are collapsed to a single term where the wall interactions can described by an effective collision frequency $\alpha\nu_{ref}$, where α is a fitting parameter and ν_{ref} is a reference collision frequency. This type of approach solely empirical in nature and depends heavily on experimental data for tuning to a specific unit and generally is not effective as a predictive tool. When using more first principles based models for wall interactions the effective collision frequency typically reduces a function of the ion velocity to the walls, which is often assumed to satisfy the Bohm condition for sheaths and therefore a function of temperature, and also a function of the secondary electron emission yield which is material and electron energy dependent. Despite being rooted in the underlying physics, this methodology can yield simulations that are markedly less accurate than the empirical approach[38]. Though wall effects certainly play a role in Hall thruster dynamics, it has been demonstrated that it cannot explain the enhanced cross-field transport on its own[3]. Other mechanisms, primarily plasma turbulence are thought to be the more dominate source of anomalous transport.

One of the most common turbulence effects incorporated into fluid models to evaluate anomalous diffusion is the so-called Bohm Diffusion, name after its discoverer David Bohm while studying cross-field transport during the Manhattan Project. Based on observations, Bohm determined a semi-empirical representation for the

cross-field diffusion coefficient as

$$D_{\perp} = D_B = \frac{1}{16}\frac{k_B T_{eV}}{eB} \tag{2.14}$$

While Bohm's formula is not derived from first principles, notably the value of 1/16 is best-fit parameter, it has been shown to describe accurately the dynamics of several $E \times B$ plasma systems. Notably the diffusion scaling now goes as $1/B$ rather than $1/B^2$ and is generally several orders greater in magnitude than the classical value. This leads to increased difficulty in confining electrons to magnetic fields, a problem for Hall thrusters and to a much greater extent the fusion community. As succinctly discussed in Ref. [21], the physics governing Bohm diffusion in the context of $E \times B$ drift plasmas can be related to random fluctuations in the azimuthal electric field E_y which has a mean zero value. Here the cross-field flux is then assumed proportional to the induced $E_y \times B$ drift:

$$\Gamma_{ex} \propto n_e \frac{E_y}{B}$$

The maximum value of the fluctuating electric field is assumed to be bounded by Debye shielding:

$$E_y = \frac{k_B T_{eV}}{eL_c}$$

where L_c is the characteristic length of the plasma. Combining these equations yields the Bohm diffusion coefficient with a constant of proportionality (α):

$$\Gamma_{ey} = \alpha \frac{k_b T_{eV}}{eB}\frac{n_e}{L_c} = D_B \nabla n$$

Noting that α is typically assumed to be 1/16 based on historical data, but other values are often used to recreate the dynamics of specific systems.

Upon inspection of Equations 2.13 and 2.14 it is evident that the Bohm mobility

can be rearranged to be expressed as an effective collision frequency:

$$\nu_B = \alpha\omega_{ce} \tag{2.15}$$

This representation for anomalous collision frequency has been used on several occasions to model electron transport in Hall thruster, and often combined with electron-wall collision inside the discharge channel[35, 46, 47, 3, 61, 39].

In addition to turbulence due to random fluctuations, Hall thrusters exhibit many coherent oscillations and instabilities over a broad frequency domain (10kHz to >10MHz) that all could conceivably contribute to some extent to anomalous transport[24]. The most fundamental and well-known oscillation exhibited in Hall thrusters is the breathing mode oscillation[98, 8, 5, 28]. This mode is ubiquitous in all Hall thrusters and typically manifests between 10-100kHz as a global oscillation where the thruster uniformly rises and falls in total discharge current. This instability is often described as a predator-prey relationship where the neutral propellant gas is ionized and then accelerated out of the channel faster than the replenishment rate of the neutrals[36]. In this way, the ionization frequency will drop, as will the discharge current, then the discharge channel will be replenished with fresh neutrals. After sufficient neutrals accumulate, the ionization rate will increase once again leading to more ions and a higher discharge current. This process then repeats indefinitely.

Despite this common description, it is not physically accurate. While the predator-prey model reasonably predicts the oscillation frequency of the breathing mode, it does not produce a stability criterion. Modern research has pointed to a more complicated physics picture where the instability could be the result of variations in the size of the ionization zone and phase lag between ionization near the anode and the region near the thruster exit[28]. Furthermore, while this mode is not directly responsible for anomalous electron transport in Hall thrusters, it has been demonstrated that

the breathing mode oscillations play a role in the process[29]. The variation in plasma parameters during a breathing mode oscillation can affect the growth or saturation of other instabilities that directly influence the cross-field electron mobility.

The instabilities theorized to drive anomalous electron transport are generally considered to be azimuthal instabilities propagating in the $E \times B$ direction that exchange energy and momentum with the $E \times B$ drifting electrons. In the next section, we will present a framework for evaluating this interaction. The azimuthal instabilities present in Hall thrusters are commonly separated into high and low frequency oscillations. In the low frequency domain, the rotating spoke instability is the most prominent. This instability manifests at wavelengths on the order of the Hall thruster circumference, oscillating in a frequency range between 10 to 100kHz. The waves have been directly observed using high-speed camera footage of thruster discharges when the oscillations closely resembled bicycle spokes rotating around the channel, hence the classification as a spoke instability[33]. Significant research was directed to the study of these spokes, demonstrating that the spokes carry significant current and their amplitude is correlated with Hall thruster performance[73]. These spoke waves could influence electron transport through the interaction between azimuthal density and electric field oscillations that give rise to cross-field transport due to an $E \times B$ interaction, similar to the description for Bohm transport. However, despite some experimental backing for the role of this instability on anomalous transport, it was determined that these spokes are not ubiquitous in Hall thrusters. With the introduction of magnetically shielded Hall thrusters, the spoke modes did not manifest in these devices[88]. Similar to wall interactions, while the spoke mode likely plays a role in anomalous transport, it is not the primary source.

High frequency azimuthal instabilities increasingly appear to play the most significant role in anomalous transport. These instabilities are typically considered to have oscillation frequencies greater than 1 MHz and wavelengths on the scale of the

thruster circumference down to the Debye length, typically on the millimeter scale or smaller. Until recently, most of the investigations into these modes have come from modeling and simulations due to the difficulties in resolving oscillations at such high frequencies and potentially very small wavelengths. Kinetic simulations performed by Adam et al. in 2004 [2] suggested that a drift instability driven by the electron $E \times B$ current is responsible for this anomalous cross-field transport. This is the so-called electron drift instability. As we will review shortly, in the last decade, this instability has received a lot of attention from the modeling and experimental Hall thruster community as the origin of anomalous electron transport, and is the primary focus of this dissertation. In a following section, we will provide a historical overview of the recent investigation into the electron drift instability that led to our present work, but first, in this section, we will demonstrate how these azimuthal instabilities result in transport across magnetic field lines.

2.4.2 Wave-Induced Transport

The wave-driven cross-field transport of electrons can modeled by returning to the drift-diffusion equation for electrons where we neglect electron inertia:

$$0 = -\frac{q^2}{m_e} n_e(\vec{E} + \vec{v}_e \times \vec{B}) - \frac{q}{m_e}\nabla(p_e) + \vec{j}_e \nu_c \tag{2.16}$$

Here m_e is electron mass, n_e is electron density, $\vec{j}_e$ is the electron current density, $\vec{E}$ and $\vec{B}$ are local electric and magnetic fields, $p_e = q n_e T_e$ is electron pressure where T_e is expressed in units of energy, ν_c is the classical electron collision frequency, and q is fundamental charge. The first term is the Lorentz force, the second is the pressure force, and the third is the effective drag due to particle collisions. We introduce wave effects into this equation by representing the electrostatic wave as rapid perturbations in density, $n_e = \delta n_e + n_{e(0)}$ and electric field, $\vec{E} = \delta\vec{E} + \vec{E}_0$, where δx terms denote the

oscillating component against a background value x_0. Then we rearrange Eq. 2.16 to solve the axial and azimuthal electron current density.

$$j_{e(x)} = \frac{q^2}{m_e \nu_c}(\delta n_e + n_{e(0)}) \left[(\delta E_x + E_{x(0)}) - \vec{v}_{e(y)} \times B_r\right] - \frac{q^2}{m_e \nu_c} \nabla_x [(\delta n_e + n_{e(0)}) T_e] \tag{2.17}$$

$$j_{e(y)} = \frac{q^2}{m_e \nu_c}(\delta n_e + n_{e(0)}) \left[(\delta E_y + E_{y(0)}) + \vec{v}_{e(x)} \times B_r\right] - \frac{q^2}{m_e \nu_c} \nabla_y [(\delta n_e + n_{e(0)}) T_e] \tag{2.18}$$

Next we take a phase average, taking the average value of the oscillating terms over the period of the oscillations, of both equations. We assume the oscillations are sinusoidal such that taking the phase average will eliminate any individual oscillating components: $\langle n_e \rangle = n_{e(0)}$. Additionally we assume that there is no steady state azimuthal electric field ($E_y(0) = 0$) or density gradient $\langle \nabla_y(p_e) \rangle = 0$, and the instability primarily oscillates in the azimuthal direction ($\delta E_x = 0$). This yields

$$j_{e(x)} = \frac{q^2}{m_e \nu_c} \left[n_{e(0)} E_{x(0)} - \nabla_x (n_{e(0)} T_e)\right] - \frac{\omega_{ce}}{\nu_c} j_{e(y)} \tag{2.19}$$

$$j_{e(y)} = \frac{q^2}{m_e \nu_c} \langle \delta n_e \delta E_y \rangle + \frac{\omega_{ce}}{\nu_c} j_{e(x)} \tag{2.20}$$

In these equations, phase averaging has eliminated the oscillating components of n_e and $\vec{E}$ except for the term containing the product $\langle \delta n_e \delta \vec{E} \rangle$. If the density and azimuthal electric field oscillations are in phase this term will be non-zero.

We now solve for the axial electron current density by combining Eq. 2.19 and 2.19 and assume the large Hall parameter $\Omega = \omega_{ce}/\nu_c >> 1$:

$$j_{e(x)} = \frac{q^2 n_{e(0)}}{m_e \omega_{ce}^2} \left(E_{0(x)} + \frac{\nabla_x (n_{e(0)} T_e)}{q n_{e(0)}}\right) \left(\nu_c - \omega_{ce} \frac{\langle \delta n_e \delta E_y \rangle}{n_{e(0)} E_{x(0)} + \nabla_x (n_{e(0)} T_e)}\right). \tag{2.21}$$

As we will show later for the instability under investigation $\langle \delta n_e \delta E_y \rangle < 0$ is less than

zero and the effect of the azimuthal oscillations is to add to the classical collision frequency and enhance cross field transport. For this reason, the wave-driven is often related to an anomalous collision frequency ν_{AN} that adds to the classical term for the overall effective collision frequency $\nu_e = \nu_c + \nu_{AN}$:

$$j_{e(x)} = \frac{q^2 n_{e(0)}}{m_e \omega_{ce}^2} \left(E_{0(x)} + \frac{\nabla_x (n_{e(0)} T_e)}{q n_{e(0)}} \right) (\nu_e), \tag{2.22}$$

where the effective anomalous collision frequency is defined as

$$\nu_{AN} = -\omega_{ce} \frac{\langle \delta n_e \delta E_y \rangle}{n_{e(0)} E_{x(0)} + \nabla_x (n_{e(0)} T_e)}. \tag{2.23}$$

This definition underscores the fact that from a fluid, phase-averaged perspective, the propagation of the instability can be represented as an enhanced transport coefficient for the electrons. Similarly, per the definition, we see that as the relative fluctuations in electric field and density from the waves increase, the wave-induced cross-field transport on the electrons will be higher. Physically, this scaling stems from the fact that the growth of the instability can be interpreted as an effective drag on the azimuthal drift in the plasma, which in turn promotes cross-field current.

2.5 The Electron Drift Instability

In previous section we demonstrated that an azimuthal wave can give rise in enhanced cross-field dependence the phase and amplitude of the electric field and density perturbations. In this section we provide an in-depth review of the instability considered most likely to govern the anomalous transport phenomenon, the electron drift instability(EDI). While research on the EDI dates back several decades with the development of analytical models for fusion plasmas, most studies of this instability as it applies to Hall thrusters have occurred in the last two decades. Much of this

work has focused on theoretical analysis or particle-in-cell simulations, but in recent years there have been an growing set of experimental studies giving insight into the nature of the EDI in Hall thrusters. The major results from our research builds on the tremendous layer of knowledge built by the research community. In order to provide proper context for our work, in this section we will provide the theoretical framework for the EDI in Hall thrusters, review the results of major simulation projects that studied the EDI, and discuss the limited experimental data that existed for the EDI prior our research.

2.5.1 EDI Simulations and Analytical Treatment

Spurred by the inability of wall effects to explain anomalous transport and growing evidence of micro-turbulence in Hall thrusters significant effort was placed on developing high-fidelity models that could resolve small-scale instabilities that were theorized to drive anomalous transport. The first major simulation that demonstrated azimuthal micro-turbulence in Hall thrusters was the 2004 2D kinetic simulation of Adam et. al[2]. This axial-azimuthal simulation treated the simulation domain as a linear box was with periodic boundary conditions along the azimuthal direction with an overall length of only a couple millimeters and the axial direction was only a few centimeters. In with this massive reduction in geometry extent of the future Hall thruster the computational cost as the time was extreme. Despite these limitations, without any artificial tuning this kinetic model was able to resolve several key features of Hall thruster operation, such as the Hall thruster breathing mode, spatial variations in density and electric field, and relatively accurate magnitudes of the various plasma parameters. A remarkable accomplishment for the field at the time. Furthermore, and perhaps even more importantly, this simulation demonstrated the formation of a strong high frequency and small wavelength azimuthal instability. It was this instability that was responsible for the enhanced diffusion across magnetic

field, which the authors strongly attribute to small wavelength of the instability which was on the order of the electron Larmor radius. The instability appeared to develop using the high speed $E \times B$ drift as an energy source for wave growth. This instability would later be classified as the electron drift instability.

Following the promising work of Adam, effort turned towards classifying the instability observed in the kinetic simulations. These works aimed at developing an analytical dispersion relation for an instability that develops along an $E \times B$ drift with frequency and wavelength matching those seen by Adam. The dispersion relation for a plasma describes how an instability behaves as a function of oscillation wavelength, both in terms in oscillation frequency and growth rate. This is a gross simplification of the importance and complexity of plasma dispersion relations and we direct the reader to the works of Stix[91] and Swanson[92] for a thorough description of plasma waves. The dispersion relation is typically described as a complex function with a real part that denotes the frequency ($\omega(k)$) of oscillations at a particular wavenumber (k), and an imaginary component that represents the growth rate ($\gamma(k)$), that is the rate the amplitude of an oscillation increases. The dispersion is determined by solving the dielectric plasma function, which for all but very simplified situations is only possible through numerical techniques, again we direct the reader to resources such those previously highlighted for a proper introduction these methods as it is well beyond the scope of this dissertation. For the Hall thruster plasma, the linear dielectric function was developed by Ducrocq et.al[32] and later refined by Cavalier et. al[19]:

$$\epsilon^{(1)} = 1 + k^2\lambda_{De}^2 + g\left(\frac{\omega - k_y V_d}{\omega_{ce}}, (k_x^2 + k_y^2)\rho^2, k_z^2\rho^2\right) - \frac{k^2\lambda_{De}^2\omega_{pi}^2}{(\omega - k_x v_{di})^2}, \tag{2.24}$$

where $g(\Omega, X, Y)$ is the Gordeev function defined as

$$g(\Omega, X, Y) = i\Omega \int_0^{+\infty} e^{-X[1-cos(\varphi)]-\frac{1}{2}\varphi^2+i\Omega\varphi} d\varphi. \tag{2.25}$$

where ω is the oscillation frequency, ω_{ce} is the electron cyclotron frequency, ω_{pi} is the ion plasma frequency, $k = \sqrt{k_x^2 + k_y^2 + k_z^2}$ is the oscillation wavenumber, k_x is the wavevector component traveling in the axial direction, k_y is the component in the $E \times B$ direction, k_z is the component in the radial direction (along magnetic field lines), V_D is the azimuthal electron drift velocity, v_{di} is the ion beam velocity in the axial direction, λ_{De} is the Debye length, and $\rho = V_{th}/\omega_{ce}$ is the electron Larmor radius at thermal velocity $V_{the} = \sqrt{T_e/M_e}$ where T_e is expressed in terms of energy. The main assumptions invoked in this dispersion relation are

- The steady state electric field is only in the axial direction ($\boldsymbol{E} = E\hat{\boldsymbol{x}}$).
- The magnetic field is pure radial ($\boldsymbol{B} = B\hat{\boldsymbol{z}}$).
- Electrons are magnetized and have an azimuthal drift velocity of $\boldsymbol{V_D} = V_D\hat{\boldsymbol{y}}$.
- Ions are unmagnetized.
- Magnetic field and density gradients are ignored
- The electron velocity distribution is assumed to be maxwellian.
- The instability is purely electrostatic with a perturbed potential of the form $\phi = \phi_0 \exp[i(\boldsymbol{k} \cdot \boldsymbol{r} - \omega t)]$.

While these assumptions can differ significantly for true Hall thrusters, and in several ways also is restricting the variety of possible plasma waves, it is necessary to apply these restrictions else the problem quickly becomes intractable.For plasma parameters typical of Hall thrusters, this dispersion yields oscillations with frequencies

in the megahertz domain and resonant wavelengths on the order of millimeters or smaller; these occur at $k \approx m\omega_{ce}/V_d$ where m is the mode number. These are the so-called cyclotron resonances that appear in Ω term of the Gordeev function: $(\omega - k_y V_d)/\omega_{ce}$. This is the inverse Larmor radius of electrons traveling azimuthally with $E \times B$ velocity V_d. Physically, this can be described as Bernstein waves being Doppler-shifted to frequencies lower than the cyclotron frequency by the high electron drift velocity such that they merge with the ion acoustic wave[40]. Characteristic dispersion relations for the EDI are shown in Figure 2.6 highlighting several key features. When the radial wavenumber is small distinct cyclotron resonances are evident in both the real and imaginary components of the solution. Growth becomes peaked at the resonance frequencies and the real frequency exhibits sharp changes in azimuthal group velocity around the harmonics. In literature, this type of solution to the EDI dispersion relation is often called the electron cyclotron drift instability (ECDI). Although it is important to note that the first peak growth rate occurs around $k_y \lambda_{De} \approx 0.1$ is not the fundamental cyclotron resonance mode ($m = 1$). This low frequency portion of the EDI dispersion is associated with an instability known as the modified two-stream instability (MTSI)[56]. While the growth rate at these large wavelengths is much smaller the cyclotron resonances, as well be discussed in more detail later, the MTSI likely plays an important role in the non-linear saturation of the overall EDI instability.

If there axial component of the wave ($k_x = 0$) then the real frequency is bounded by the ion plasma frequency. When there is wave propagation in the axial direction the real frequency is Doppler-shifted by the term $k_x v_p$. As the radial wavenumber increases the instability trends toward a so called modified ion acoustic instability where the resonances have been smoothed out in both real frequency and growth rate. This ion acoustic like solution results in a drastically simpler dispersion relation

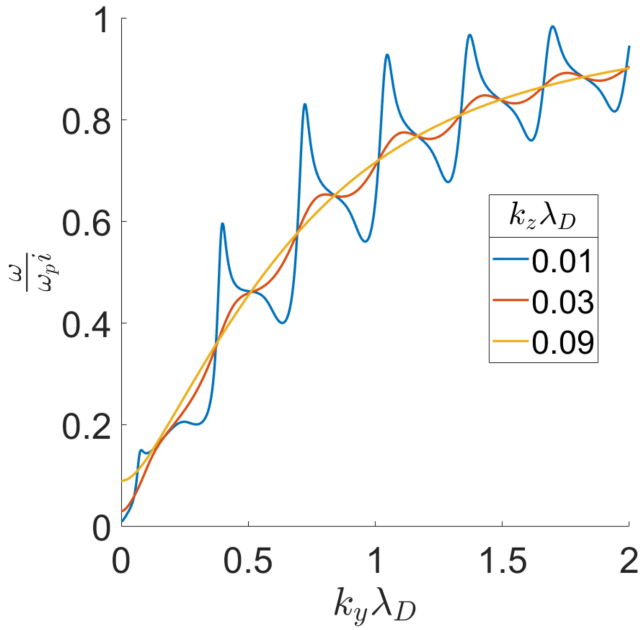

(a)

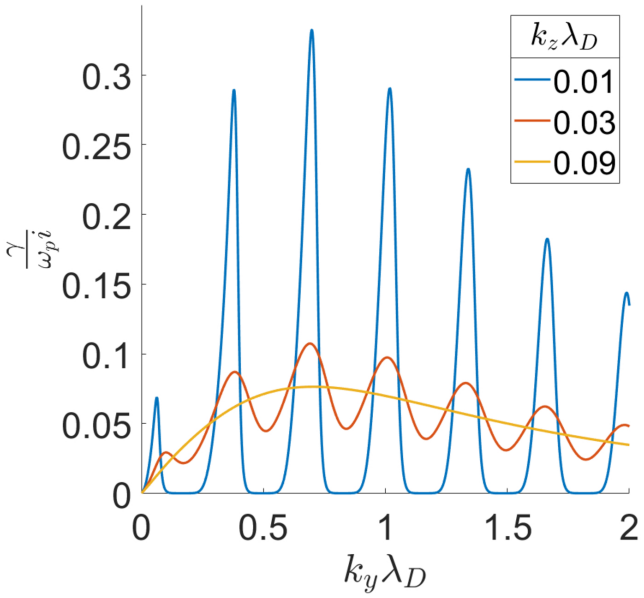

(b)

Figure 2.6: Solutions of the EDI dispersion relation, adapted from Cavalier et al[19] with different radial wave components (k_z). Frequency (a) and growth rate (b) are normalized by the ion plasma frequency (ω_{pi}) and wavenumber is normalized by the Debye length(λ_{De}).

given by

$$\omega_r = \boldsymbol{k} \cdot \boldsymbol{v_{di}} \pm \frac{k c_s}{\sqrt{1 + k^2 \lambda_{De}^2}} \tag{2.26}$$

$$\gamma = \pm \sqrt{\frac{\pi M_e}{8 M_i}} \frac{\boldsymbol{k} \cdot \boldsymbol{v}_D}{(1 + k^2 \lambda_{De}^2)^{3/2}}, \tag{2.27}$$

with peak growth at the wavenumber $k_{max} = 1/\lambda_{De}\sqrt{2}$. There is currently no consensus as to what exact flavor of instability (ECDI, MTSI, ion-acoustic) the EDI manifests itself as in Hall thruster plasmas and for the rest of the this work we will refer to these different solutions of the dispersion relation collectively as the EDI.

Over the last decade many high fidelity Hall thruster simulations have resolved the EDI instability and typically demonstrate that it results in the anomalous electron transport. While it is not possible adequately cover every single reference[63, 55, 56, 81, 9, 52, 60, 32, 19, 64, 1, 59], we summarize here several of the major findings from the last two decades of kinetic and particle-in-cell simulations and then highlight a key works:

- Most simulations showed the ion acoustic form of the EDI where the oscillations were dominated by a nearly monochromatic wave at the wavenumber of peak growth estimated from Equation 2.27[63, 65].
- The EDI was shown to effectively enhance cross-field mobility
- The saturation mechanism, which determines the final amplitude of the instability, was mostly commonly observed as ion wave trapping in the azimuthal direction and axial wave energy convection[65, 66]
- In direct contrast to the first point, a few very recent and high resolution simulations show an ECDI like instability with discrete resonances[55, 56].

Despite the substantial simulation work that occurred over the last two decades, there have been little to no experimental evidence to confirm or reject any of the

conclusions listed above. The primary focus of this dissertation centers around provide this knowledge gap and resolve many of the ambiguities and disagreements seen across the various models, but first in the following section we provide an overview the current experimental evidence support the existence and role of the EDI prior to our research efforts.

2.5.2 Experiential Work

Following the seminal work of Adam's 2004 kinetic simulations, there were a handful of experiments that attempted to investigate high frequency oscillations in Hall thruster plumes. In particular, Litvak[69] and Lazurenko[67] utilized high-speed electrostatic probes situated in the Hall thruster walls and plume to investigate plasma oscillations. Their techniques were very similar to those outlined in Chapter 3, but with limited capabilities and resolution due to hardware restrictions. Litvak et al. measured oscillations with appreciable amplitude in the 1-15MHz domain, but they inferred the wavelength was on the order of the Hall thruster channel circumference, substantially larger than the EDI, and attributed the waves to a Rayleigh-type instability driven by gradients in density, magnetic fields, or drift velocities[34, 68]. Lazurenko et al. measured a similar frequency domain as Litvak and also saw high amplitude content in the 1-30MHz domain. Notably from their work, they measured the wave properties in the axial and azimuthal directions and determined the wave was propagating in both directions, with phase velocities on the order of the electron $E \times B$ drift velocity. Additionally, the dispersion relation was linear, like the ion acoustic results for the EDI, but the phase velocities were well above the predictions of the EDI, which would be close to the ion sound speed. While these works demonstrated the existence of high-frequency oscillations in Hall thrusters, they implied the waves were not from the EDI. Though as we discuss in later chapters, there were several limitations to these experiments that likely limited the detection of the EDI,

such as limited wavelength resolution due to probe design, and a limited measurement domain due to hardware restrictions.

The first substantial experimental evidence for the existence of the EDI in Hall thrusters came from the collective Thomson scattering (CTS) experiments of Tsikata et al.[101, 100, 99]. This breakthrough experiment differed significantly from previous experimental investigations by not relying on electrostatic probes that can distort the thruster plasma and have several limitations on spatial and wavelength resolutions. Instead, these experiments utilized laser-based diagnostics to infer the frequency, wavelength, and strength of oscillations based on how they scatter electromagnetic waves. While this diagnostic system is regularly used in the fusion plasma community, it is extraordinarily difficult to develop a diagnostic for Hall thruster plasmas due to their relatively low density and therefore weaker detection signal. The experimental apparatus itself represents a significant achievement, and the experiments yielded substantial new insights into the high-frequency oscillations in Hall thrusters and the nature of the EDI. In the measured wavenumber domain of 5000-12000 rad/m (wavelengths between 0.5 and 1.2mm), the wave had a linear dispersion with oscillation frequencies between 2 and 6 MHz and a group velocity close to the ion sound speed. This strongly resembled the ion-acoustic form of the EDI and had the correct length scales and frequency. Furthermore, the experiment revealed the wave was not purely azimuthal and was oriented 10 degrees axially towards the thruster and 4.6 degrees radially outward. This data was compared against the theoretical dispersion relation, and it was determined that the necessary plasma parameters required for the EDI were within reasonable expectations for the Hall thruster plume. However, there were some disagreements between theory and experiment, the most significant of which relates to the amplitude of EDI oscillations. Firstly, the ion-acoustic form of the EDI predicts the strongest oscillations should occur at the wavelength corresponding to maximum growth, $k_{max} = 1/\lambda_{De}\sqrt{2}$. Despite this being within the measurement do-

main of the CTS diagnostic, no peak was observed in the experiment; in fact, the wave amplitude was increasing exponentially at lower frequencies and larger wavelengths. Furthermore, the magnitude of the oscillations was appreciably smaller than the levels predicted to be necessary to cause anomalous cross-field transport. Despite the remarkable success of this experiment, the role of the EDI and its exact dispersion relation remained inconclusive. These concerns, in addition to the numerous ambiguities among Hall thruster simulations of the EDI, spurred much of the motivation for the experiments carried out in this work.

Overall, the body of knowledge prior to this work strongly suggested that the electron drift instability was the primary mechanism resulting in anomalous transport of electrons across magnetic field lines in Hall thrusters. Much of the evidence supporting this theory was rooted in numerical simulations. However, due to the numerous simplifications and assumptions employed in these simulations, there was no consensus that the results accurately represented the real Hall thruster plasma. Moreover, the simulations from different research groups showed several important disagreements, and there was minimal experimental evidence validating these models. Despite the promising CTS experiment that strongly pointed toward the existence of the EDI in Hall thrusters, there was still no definitive description of the EDI in Hall thrusters or its role in anomalous transport. The need for more experimental efforts was apparent.

2.6 Conclusions

Hall thrusters are quickly becoming the dominant workhorse of the electric propulsion industry. Despite the technological maturity of these systems and their widespread adoption, several fundamental aspects of their operation are not yet fully understood. This gap in knowledge of the underlying physics greatly impedes the pace of development for new systems and forces the Hall thruster community to rely primarily on

lengthy and costly experimental test campaigns for design validation. Although Hall thruster modeling efforts and simulation techniques have made great strides in the last decade, they still cannot be reliably and expediently used as predictive design tools. The primary knowledge gap holding back these efforts is the lack of understanding about the anomalously high transport of electrons across magnetic field lines. High-fidelity simulations can directly calculate this anomalous transport term by resolving the instability-induced oscillations in density and electric field. However, as highlighted earlier, these simulations often do not resolve the full Hall thruster geometry, meaning they cannot be used to validate Hall thruster designs. Nevertheless, they are extremely useful in learning about the governing physics of instability-driven transport. This leads to modeling techniques where the anomalous collision frequency is estimated by a simplified model that does not simulate the instability and attempts to capture its effect at a macroscopic level. A common method assumes the anomalous collision frequency scales approximately with the cyclotron frequency $\nu_{AN} = \alpha\omega_{ce}$, where α is a tunable parameter or a function of multiple variables. This ad hoc term can be used to include wall interactions, Bohm diffusion, and wave-driven transport, but these types of models heavily depend on experimental data to adjust the free parameters introduced through the simplified model and are often only valid for a unique thruster. While many in the Hall thruster modeling community have looked to the electron drift instability to explain anomalous transport, at the start of our research, there was no definitive evidence proving these hypotheses. Outside of simulations, wave-induced anomalous collision frequency can be directly evaluated with experimental data using Eqn. 2.23, provided that the fast density and electric oscillations can be measured. In practice, it is not possible to measure both of these quantities simultaneously at the same position. Therefore, the technique is simplified by measuring only density fluctuations and using an assumed dispersion relation for the EDI to estimate the electric field perturbations. It is this method that we exploit in this

work to evaluate anomalous cross-field transport in Hall thrusters. However, to do so, the dispersion relation must be known, and numerical simulations have not reached a consensus on the proper form of the dispersion relation. Our research efforts aim to resolve these critical deficiencies. In Chapter III, we review the technique used to experimentally measure high-speed density fluctuations in Hall thruster plumes and determine the dominant instability. In Chapter IV, we present experimental data demonstrating that the primary instability relevant to anomalous transport is the Electron Drift Instability, and we estimate the correct dispersion relation. Finally, in Chapter V, we combine all of this data to evaluate electron transport for comparison to models and simulations.

CHAPTER III

Experimental Techniques

3.1 Introduction

In this chapter, we describe the techniques used for investigating anomalous electron transport in Hall Thrusters. First, we present the thruster used for study and the vacuum facility utilized for our experiments. Next we discuss the analysis techniques employed used to infer characteristics of the electron drift instability and its influence of cross-field transport. The analysis in broken into two main aspects, the first covers the wide-breadth of methods that fall under the umbrella of spectral analysis. The spectral analysis primary involves Fourier analysis, Beall analysis that outputs an instability wavenumber, frequency, and amplitude from measured waveforms, and also bispectral techniques that use advanced mathematical methods to infer the growth and non-linear aspects of any measured instabilities. Then we describe the probing methods used to generate the data applied to the aforementioned analysis techniques. Finally, outline the specific implementation of these techniques in our experimental campaigns.

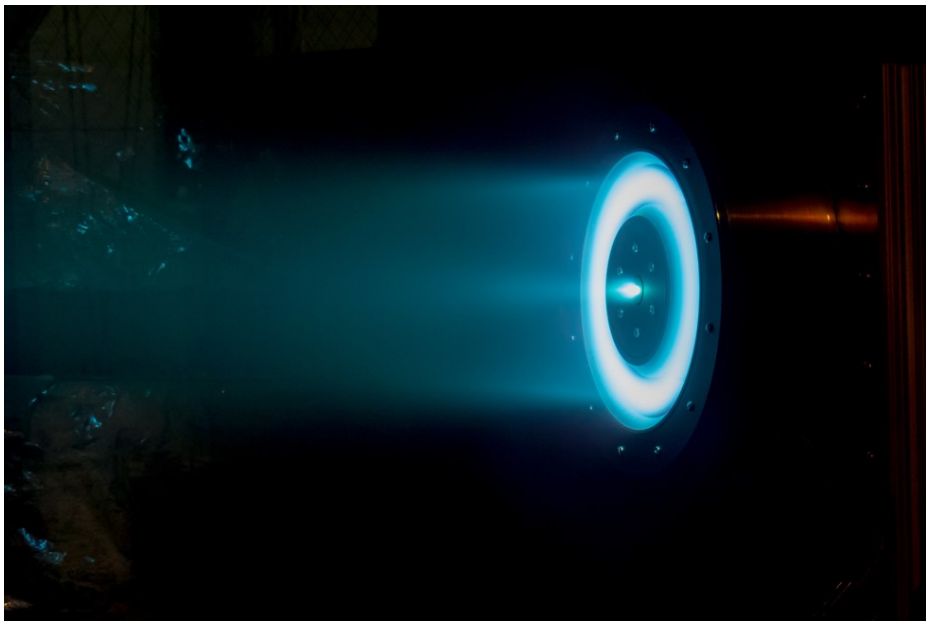

Figure 3.1: The H9 magnetically shield Hall thruster

3.2 The H9 Hall Thruster

For our experimental campaigns, we solely employed the H9 Hall thruster as the test apparatus. The H9 is a relative new state-of-the-art Hall thruster developed jointly by NASA's Jet Propulsion Laboratory, the University of Michigan, and the Air Force Research Laboratory [49, 25]. It features a center-mounted LaB_6 hollow cathode and operates with a 7% cathode flow fraction. The thruster body was electrically connected to the cathode. It is designed to operate over many different operating conditions ranging from approximately 1kW to 9kW, but most experiments covered in work utilized a 4.5kW operating condition with nominally 300V discharge voltage and 15A discharge current. The propellant is 99.9995% pure xenon and the flow rate is commanded using a set of Alicat MC series mass flow controller, calibrated with a Drycal Bios Definer fine-volume measurement unit.

The thruster is relatively unique, compared to many previous Hall thruster designs, as it employs a magnetically shielded topography [76]. This shielding technology shapes the magnetic field lines such that curve along edge of the channel walls and

far into the channel toward the anode. For conditions typical of Hall thrusters, magnetic field are assumed to be isothermal and as such the potential along field lines scale approximately as $\phi = \phi_0 + T_e \ln n_e/n_{e0}$, where ϕ_0 and n_{e0} are notionally the plasma potential and density at the channel centerline where it intersects with the field line. By having the magnetic field lines curve along the wall and deep into the channel the electron temperature on this field line is kept cold and the potential remains close the anode potential. These two characteristics result in significantly lower ion kinetic energy directed towards the walls and virtually eliminates erosion of the channel walls. This magnetic shielding has three additionally important effects that influence our experimental techniques and analysis of instability measurements. First, the acceleration zone–the small region of high axial electric field—shifts downstream relative to unshielded thrusters such that it lies just downstream of the thruster exit plane. The electron drift instability is expected to grow where the electric field is strongest, as it draws energy from the azimuthal electron $E \times B$ kinetic energy, therefore in shielded thrusters it much easier to probe the regions of the plasma relevant to the EDI formulation and growth. Second, the electron temperature in shielded thrusters has been measured significantly hotter than unshielded designs, and since the EDI dispersion relation is sensitive to this parameter there may be differences in the nature of the EDI measured with the H9 compared to previous thrusters. Although, given the ubiquitous nature of anomalous electron transport in Hall thrusters we expect the EDI to still be present and critical to all Hall thruster designs. Additionally, due to the advantages of shielded magnetic field topologies, we expect data from experiments on the H9 to be particularly relevant to future Hall thruster development. Finally, the dispersion relation of the EDI was derived assuming the magnetic field is purely radial and therefore there are important differences in the nature of the instability close to the walls compared to the centerline. All data in our experiments is collected along the channel centerline and therefore we do not consider this nuance in much of

Figure 3.2: Large Vacuum Test Facility at the University of Michigan

analysis and discussion.

3.3 Test Facility

All experiments were performed in the Large Vacuum Test Facility (LVTF) at the University of Michigan in the Plasmadynamics and Electric Propulsion Laboratory (PEPL). LVTF is a 6 m diameter by 9 m long chamber (Fig. 3.2). LVTF uses 19 cryogenic pumps to achieve a pumping speed of approximately 500,000 L/s on xenon including conductance losses. This results in a base pressure of 10^{-8} Torr-N2 and typical working pressures in the range of $5 \cdot 10^{-8}$ Torr-Xe. Following the guidelines outlined in Ref [30] pressure is measured with a xenon calibrated Stabil ion gauge mounted 1 meter offset from the thruster and in the same plane as the thruster exit plane.

3.4 Wave Probes

3.4.1 General Description

To measure plasma oscillations we made extensive use of so-called 'wave probe'. The wave probe consists of pairs of closely spaced Langmuir probe that are biased to collect ion saturation current, see Figure 3.3. Langmuir probes have been used extensively as critical plasma diagnostic to measure plasma density, potential, and temperature[70]. The basic principle of operation for the probe is as follows, an electrode is exposed to the plasma and collects some amount of ion and electron current. The collected current of each species is proportional to several plasma parameters and an applied potential to the electrode. By analyzing the collected current versus the applied voltage the various parameters can be isolated and calculated. For probes biased with a strong negative voltage all electrons are repelled and only the probe only collects ion current equal to the ion saturation current. In this ion saturated current ions impact the probe at the Bohm speed, $v_B = \sqrt{eT_e/m_i}$, and the total collected ion current therefore is a function of the electron temperature, plasma density, and collection surface area:

$$i_{sat} = -\exp -\frac{1}{2} e n_{i0} A_s \sqrt{\frac{eT_e}{m_i}}. \tag{3.1}$$

Here n_{i0} is background ion plasma density, A_s is the probe surface area, and $\exp -1/2$ is a correction factor based on assumptions about the probe sheath—primarily that the radius of the probe is significantly larger than the Debye length. If electron temperature oscillations are assumed to be small then oscillations in the ion saturation current are proportional plasma density oscillations:

$$\frac{\tilde{n}}{\overline{n}} \approx \frac{\tilde{i}_{sat}}{\overline{i}_{sat}}, \tag{3.2}$$

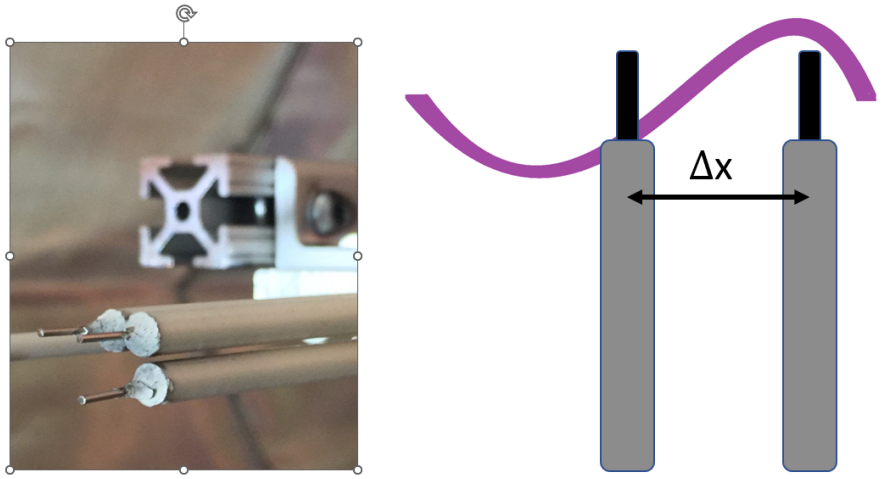

Figure 3.3: An example wave probe diagnostic consisting of closely space Langmuir probes biased to ion-saturation current.

Here $\tilde{x}$ denotes perturbations about a mean value $\overline{x}$: $x = \tilde{x} + \overline{x}$. Therefore high speed measurements of ion saturation current yield measurement of relative density oscillations and can be used to the detect the presence of instabilities through the use of the spectral analysis techniques we outline in the next several sections. Additionally, the constant temperature assumption is only a weak requirement, however, since as shown in Ref. [79], even large changes in electron temperature only marginally perturb the relationship between density and ion saturation current.

3.4.2 Fourier Analysis

The main analysis technique applied to the measured ion saturation current waveforms is the Discrete Fourier Transform (DFT or FFT). Given a waveform of length N: $x_k, k = 0...N-1$, the FFT produces a new vector of complex numbers $y_m, m = 0...N-1$, where

$$y_m = \sum_{k=0}^{N-1} x_k \exp\left(-2\pi i \frac{mk}{N}\right), m = 0...N-1. \tag{3.3}$$

For an input waveform of purely real numbers the vector y_m obeys the following property: $y_{N-m} = y_m^*$ where * denotes the complex conjugate, and if N is an even number then y_0 and $y_{N/2}$ are purely real. The values above $m = N/2$ are ignored due to their redundancy and for a time-dependent input waveform collected at a sampling rate f_s, each value at index m is representative of frequency bin given $f_m = mf_s/N, m = 0...N/2$. The FFT can be related to physical properties if we assume the plasma oscillations are composed of linear combinations such that

$$\delta n = \sum_f |\delta n_f| \exp(-i(2\pi f t)) \tag{3.4}$$

where $|\delta n_f|$ is the amplitude of the oscillation at frequency f. Subject to this assumption the y_m values are related to the oscillation amplitudes by

$$|\delta n_f| = \frac{2}{N}\sqrt{|y_m|^2}, m = 0...N/2. \tag{3.5}$$

This resulting vector can be thought of as the power spectrum of the oscillations, although strictly the definition of power spectrum (and power spectrum density) varies slightly. Nonetheless, by performing the FFT on a single ion-saturation probe, the strength of plasma oscillations as a function of frequency can be determined.

By using two ion saturation probes the wavelength can also be calculated using the FFT. We expanded Equation 3.4 to include variation in position as well as time:

$$\tilde{n} = \sum_f |\delta n_f| \exp(-i(2\pi f t - k_f x)) \tag{3.6}$$

where k_f is the wavenumber at frequency f. The term $k_f x$ can be treated as a phase difference (Θ_f) between a signal measured at two locations x_1 and x_2: $\Theta_{f2} - \Theta_{f1} = k_f(x_2 - x_1)$. By the properties of the Fourier transform the phase difference between

two signals n_1 and n_2 can be calculated using the cross-correlation:

$$\Theta_{f2} - \Theta_{f1} = \tan^{-1}\left(\frac{Im\left[y_{m1}^* y_{m2}\right]}{Re\left[y_{m1}^* y_{m2}\right]}\right) \tag{3.7}$$

where y_{m1} is the FFT of probe 1 and y_{m2} is the FFT of probe 2. If the distance between the two probes is known (Δx) then the wavenumber can be calculated by:

$$k_f = \frac{\Theta_{f2} - \Theta_{f1}}{\Delta x}. \tag{3.8}$$

The can also be visualized as measuring the delay between when a particular phase of the oscillation passes probe one and then later reachs probe 2, see Figure 3.3. Since the phase is bounded between $-\pi$ and π, this technique can only measure a maximum wavenumber of $k_{max} = \pi/\Delta x$. If wavenumbers greater than limit are present in the measurement they are aliased into the measurable wavenumber bin by $k_{measured} = k_{true} - nk_{max}$ where is an integer number denoting how many times multiples of $2k_{max}$ can be divided into the true wavenumber . For example if the maximum wavenumber directly measurable was 100 rad/m and there was a wave at 125 rad/m the FFT analysis would yield a calculated wavenumber of -75 rad/m and a wave at 275 rad/m would yield 75 rad/m. It is also important to note that in the context of 3D wave propagation this two-point analysis method only calculates the wavenumber along the vector connecting the two probe tips. To fully characterize the dispersion relation of a 3D instability this analysis must be repeated with measurements from probes taken in three separate configurations to measure the wavenumber along the x, y, and z-axes.

All together the FFT analysis yields three very important characteristics an instability: amplitude, frequency, and wavenumber (wavelength). In principle, this information could be used to identity the dispersion relation of any instabilities present in the plasma plume, but it is limited in a few key aspects. One major limitation of

this simple analysis is that it does not on its own produce a clear result due the noise environmental encountered in the plasma that distorts the measured waveforms. To filter out noise, any recorded waveform is subdivided into a set of several smaller waveforms, the Fourier analysis is applied on each sub-waveform and the results are averaged together to get yield the statistical average power spectrum and cross-correlation/wavenumber. For example, we show in Figure 3.4 a sample power spectrum density plot taken from a single wave probe tip where the sampling frequency was 100 MHz and two millions samples were recorded, if no averaging is performed the resulting power spectrum is extremely noise with the values jumping over several orders of magnitude every couple hundred Hertz. If the wave is subdivided into 1000 smaller waveforms with 2000 samples, the computed average power spectrum is very smooth function with little evident spurious noise. Although, by performing the FFT on individual sub-waveforms with fewer sample points the frequency resolution of the FFT is diminished, $f_{res} = f_s/N$. Therefore averaging should be performed until the resulting frequency resolutions starts approaching the frequency domain expected of the instability. This statistical averaging technique is further expanded upon to provide even more context about the uncertainty of the wavenumber calculation through a process called Beall analysis. Later, we will also detail an advanced Fourier based analysis method, generally referred to as bispectral analysis that can provide intricate detail about a measured instability's growth rate and non-linear properties.

3.4.3 Beall Analysis

Beall analysis is mostly an extension of the simple Fourier analysis discussed in the previous section. Instead of calculating the wavenumber as a function of frequency through the cross-correlation, the Beall method uses a binning technique to generate a probability chart where the axes are frequency and wavelength. The amplitude of each cell corresponding to the relative to its neighbors represents how likelihood that

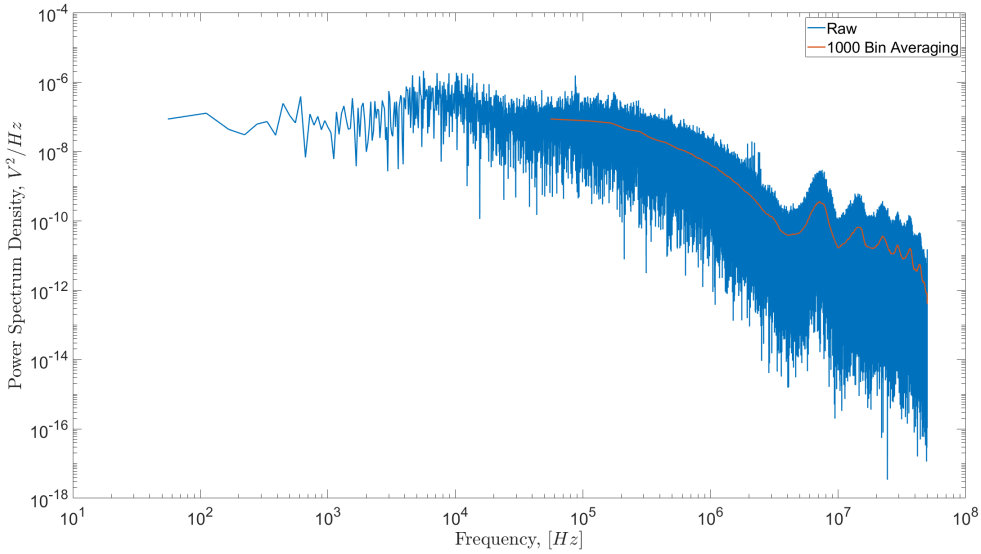

Figure 3.4: Sample power spectrum density plot demonstrating the effect of binning and averaging on signal-noise.

the particular combination of frequency and wavenumber exists in the experimental plasma. Mathematically, this is matrix is constructed as follows. The measured signal is subdivided into a set of smaller waveforms as in the simple Fourier analysis, then the power spectrum and wavenumber of oscillations are determined using the methods of the previous sections. Each waveform produces two vectors, both a function of frequency, representing the intensity of oscillations $|\delta n_f|$ and the wavenumber of the oscillations k_f. Next a wavenumber vector is proscribed that will form a set of l bins that the previous results will be averaged within. The final Beall matrix is composed of l columns and M rows, where M is determined by the frequency resolution from the Fourier analysis. For each Fourier result on the sub-waveforms, the value of $|\delta n_f|$ is added to a cell with the column corresponding to its frequency and row where the measure wavenumber falls with in the bin width of the set wavenumber array. Mathematically this can be expressed as

$$S(f,k) = \frac{1}{M}\sum_{j=1}^{M} I_{0,\Delta l}(k - k^j(f))|n^j(f)| \tag{3.9}$$

Here j indicates the sub-waveform number and $I_{0,\Delta k}(k - k^j(f))$ is a binning function defined by

$$I_{0,\Delta k}(k - k^j(f)) = 1 \text{ if}(k - k^J) < \Delta k, \text{ and 0 otherwise.} \tag{3.10}$$

This way power is only added into a wavenumber bin k if the measured wavenumber $k^j(f)$ falls within particular bin boundaries.The value at a particular frequency and wavenumber combination, $S(f, k)$, will continue to increase if it contains significant power in the majority of sub-waveforms. Due to noise, and potential time-dependence of the oscillation, any cell could get some amount of power added to it, but if there are plasma waves in the measurement data the cells corresponding to noise will contain significantly less power than those representing the wave. Two example Beall plots are shown in Figure 3.5a and 3.5b that were created using two artificial waveforms that represent a wave with linear dispersion ($f \sim k$) and power inversely proportional to frequency $|\delta n_f| \sim 1/f$. In these plots, the y-axis is frequency normalized by the sampling rate and the x-axis is wavenumber normalized by the probe radius. Here the aliasing effect described in the previous section is extremely evident with the linear dispersion wrapping around the sides of the plot twice. The added statistical information retained by the Beall analysis allows for aliasing to be more readily identified than simple cross-correlation analysis and even potential removed with further post-processing known as anti-aliasing.

Although the waveforms used in constructed these figures used the same artificial wave, the Beall plot in Fig. 3.5b was generated after adding broadband noise to the signal. While the dispersion is still visible at low frequency, where the wave power is higher, the high frequency component is obscured by the noise. When considering actual experimental data, noise can come from several sources such as 1) background electric noise that is generally broadband like the figure shown here 2) Spurious pick

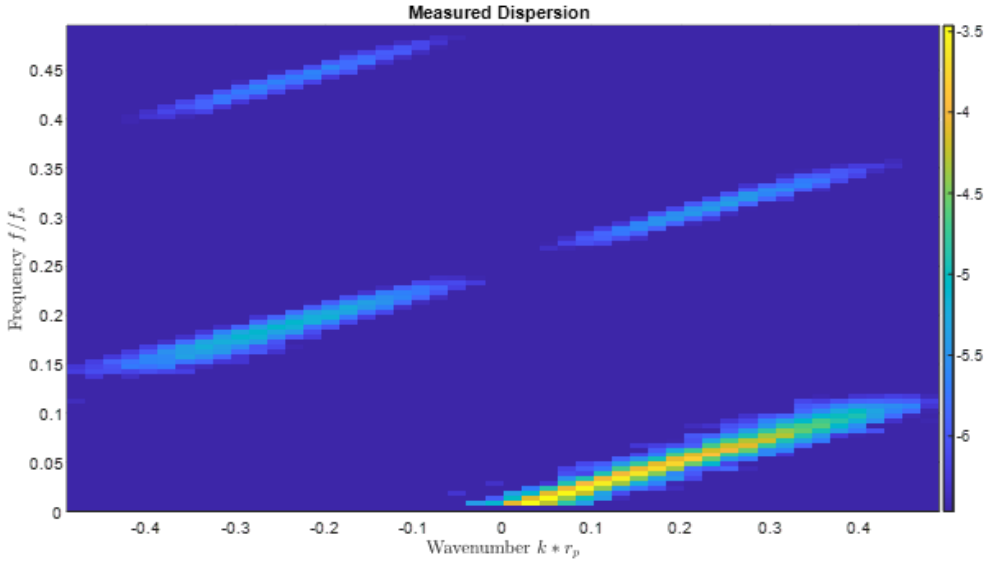

(a)

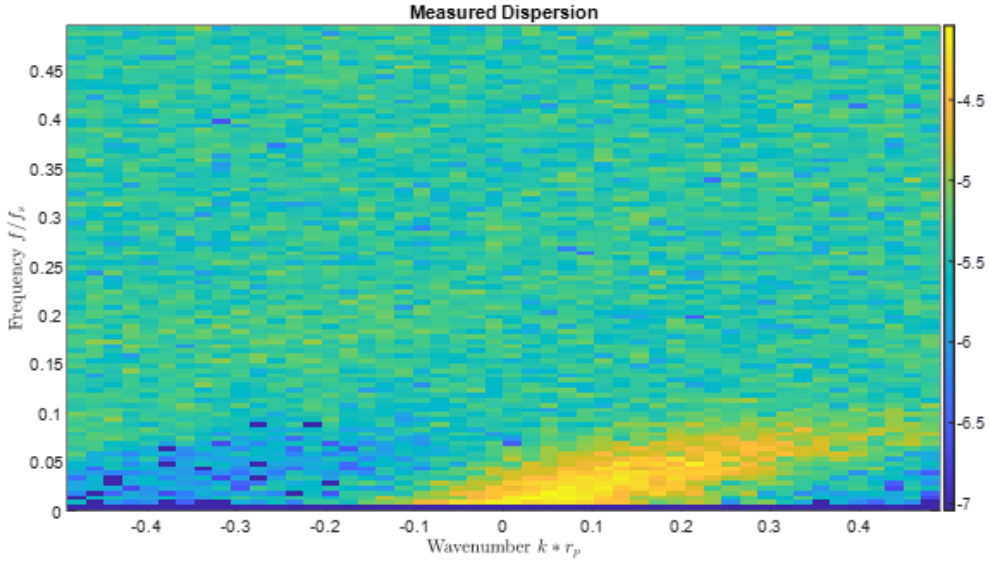

(b)

Figure 3.5: Examples of a Beall histogram chart constructed from artificial waveforms with a linear dispersion, (a) High signal to noise ratio (b) Low signal to noise. The x-axis is wavenumber, normalized by the probe radius to demonstrate aliasing, the y-axis is frequency normalized by the sampling rate.

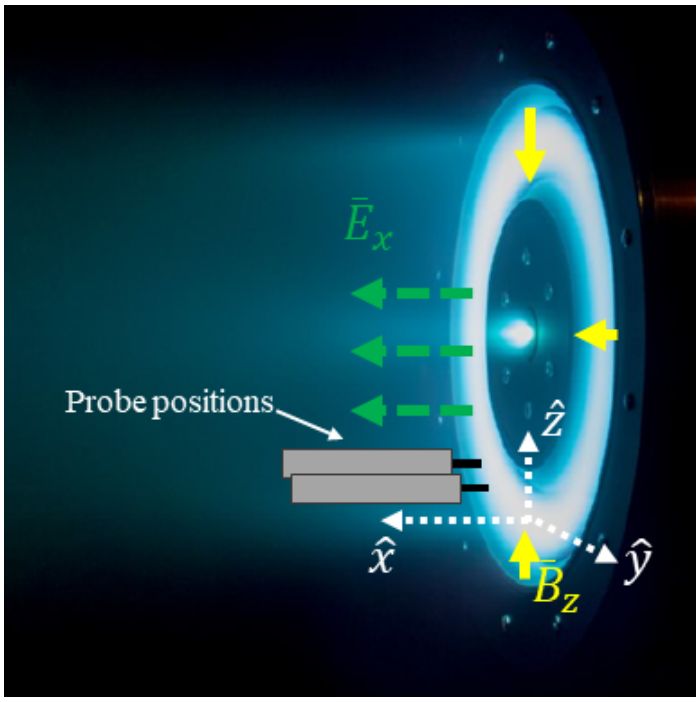

Figure 3.6: H9 Hall thruster shown with axial electric field ($\bar{E}$), radial magnetic field ($\bar{B}$), and probes placed in the $E \times B$ direction.

of EM waves by the signal cable 3) effective noise set by the limiting resolution of the measurement device, waves with amplitudes smaller than the resolution of the analog-digital converter will be eliminated.

3.4.4 Bispectral Analysis

Bispectral analysis encompasses a broad range of methods that involve measuring the phase correlation between three waves and generally is employed for investigating non-linear wave-wave interactions. Bispectral analysis has been used extensively in the fusion plasma community to quantity non-linear effects and to characterize the growth and saturation of fusion instabilities. In this work we apply bispectral analysis to the Hall thruster plasma to investigate potentially non-linear mechanisms governing the formulation of the EDI, and estimate the wave-driven anomalous transport through instability growth rate measurements.

Our approach to measuring the EDI wave dynamics is based on formulating a

governing equation for the evolution of EDI wave amplitudes. We then use experimental measurements of these amplitudes and a bispectral analysis method adapted from the works of Ritz [82] and Kim [86] to infer the parameters in the wave equation that represent linear and nonlinear growth. The Ritz and Kim method has been used extensively in the fusion community to great success to identity instabilities and determine non-linear processes relevant to the instability growth and saturation. While we follow the same general procedure of Ritz and Kim, our technique has some important differences. To that end, first we shall derive the analytical treatment of Ritz and Kim specific specific to our Hall thruster experiments.

First we consider oscillations that evolve in both time and space where each oscillation mode can be represented as

$$\phi(\vec{k},\omega,\vec{r},t) = \tilde{\phi}_0(\vec{k},\omega)\exp\left(-i(\omega_r + i\omega_i)t + i(\vec{k}_r - i\vec{k}_i)\cdot\vec{r}\right) \tag{3.11}$$

where $\tilde{\phi}_0(\vec{k},\omega)$ is the complex amplitude of the wave mode at a reference position and time. The mode is represented with complex frequency $\omega = \omega_r + i\omega_i$ and wavenumber $\vec{k} = \vec{k}_r + i\vec{k}_i$ where the imaginary components correspond temporary and spatial growth or damping and the real components denote the propagation of the wave in space and time. We implicitly assume that the complex contributions are small compared to the real components. This is the two-scale approximation in which we assume the evolution of the wave amplitude is gradual with respect to the evolution of the phase of the wave. With this approximation we can rewrite this equation as

$$\phi(\vec{k},\omega,\vec{r},t) = \tilde{\phi}(\vec{k},\omega)\exp\left(-i\omega_r t + i\vec{k}_r\cdot\vec{r}\right) \tag{3.12}$$

where we have grouped the complex terms with the amplitude:

$$\tilde{\phi}(\vec{k},\omega) = \tilde{\phi}_0(\vec{k},\omega)\exp\left(\omega_i t + \vec{k}_i\cdot\vec{r}\right) \tag{3.13}$$

This allows us to represent the temporal and spatially derivatives of $\phi(\vec{k},\omega,\vec{r},t)$ as

$$\frac{\partial\phi(\vec{k},\omega,\vec{r},t)}{\partial t} = \sum_k(\omega_i - i\omega_r)\tilde{\phi}(\vec{k},\omega)\exp\left(-i\omega_r t + i\vec{k}_r\cdot\vec{r}\right) \tag{3.14}$$

$$\frac{\partial\phi(\vec{k},\omega,\vec{r},t)}{\partial\vec{r}} = \sum_k(\vec{k}_i + i\vec{k}_r)\tilde{\phi}(\vec{k},\omega)\exp\left(-i\omega_r t + i\vec{k}_r\cdot\vec{r}\right) \tag{3.15}$$

Next following technique presented in Ref.[87] by Sagdeez and Galeev, we consider the general electrostatic dispersion expanded around the complex frequency and wavenumber. This equation governs the evolution of the complex amplitude of electrostatic oscillations:

$$\begin{aligned} 0 = \left[\epsilon_r^{(1)}(\omega_r,\vec{k}_r) + i\epsilon_i^{(1)}(\omega_r,\vec{k}_r)\right]\tilde{\phi}(\vec{k},\omega) + i\omega_i\frac{\partial\epsilon_r^{(1)}(\omega_r,\vec{k}_r)}{\partial\omega}\tilde{\phi}(\vec{k},\omega) \\ - i\vec{k}_i\cdot\frac{\partial\epsilon_r^{(1)}(\omega_r,\vec{k}_r)}{\partial\vec{k}}\tilde{\phi}(\vec{k},\omega) + \epsilon^{(2)}\tilde{\phi}(\vec{k},\omega) \end{aligned} \tag{3.16}$$

where $\epsilon^{(1)}$ and $\epsilon^{(2)}$ are the first and second order perturbations and the first order term has been broken into its real and imaginary components. Next we consider the imaginary components of this equation and divide by $\frac{\partial\epsilon_r^{(1)}(\omega_r,\vec{k}_r)}{\partial\omega}$ to give:

$$\omega_i\tilde{\phi}(\vec{k},\omega) + \vec{k}_i\cdot\vec{v}_g\tilde{\phi}(\vec{k},\omega) = \gamma_k\tilde{\phi}(\vec{k},\omega) - \epsilon_i^{(2)}\tilde{\phi}(\vec{k},\omega) \tag{3.17}$$

Noting that we have following the conventions defined in Ref.[87] where we the linear growth rate γ_k and group velocity are given by

$$\gamma_k = -\frac{\epsilon_i^{(1)}(\omega_r,\vec{k}_r)}{\frac{\partial\epsilon_r^{(1)}(\omega_r,\vec{k}_r)}{\partial\omega}}$$

$$\vec{v}_g = -\frac{\frac{\partial\epsilon_r^{(1)}(\omega_r,\vec{k}_r)}{\partial\vec{k}}}{\frac{\partial\epsilon_r^{(1)}(\omega_r,\vec{k}_r)}{\partial\omega}}$$

Then add $(-i\omega_i + i\vec{k}\vec{v}_g)\tilde{\phi}(\vec{k},\omega)$ to Eqn. 3.17, multiply by $\exp\left(-i\omega_r t + i\vec{k}_r \cdot \vec{r}\right)$, and use the definitions given in Eqns. 3.14 and 3.15 to recover:

$$\frac{\partial\phi(\vec{k},\omega)}{\partial t}+\vec{v}_g\cdot\frac{\partial\phi(\vec{k},\omega)}{\partial\vec{r}} = \gamma_\omega\phi(\vec{k},\omega)+i\left(\vec{k}\cdot\vec{v}_g-\omega\right)\phi(\vec{k},\omega)-\epsilon^{(2)}\exp\left(-i\omega_r t + i\vec{k}_r\cdot\vec{r}\right) \tag{3.18}$$

Finally, we make a substitution for the second order dielectric response that relates the term to wave-wave coupling[87]:

$$-\epsilon^{(2)} = \sum_{\substack{\omega=\omega_1+\omega_2\\ \vec{k}=\vec{k}_1+\vec{k}_2}} V^Q_{1,2}\phi(\vec{k}_1,\omega_1)\phi(\vec{k}_2,\omega_2) \tag{3.19}$$

This gives our primary governing equation:

$$\begin{aligned}&\frac{\partial\phi(\vec{k},\omega)}{\partial t}+\vec{v}_g\cdot\frac{\partial\phi(\vec{k},\omega)}{\partial\vec{r}} = \gamma_\omega\phi(\vec{k},\omega)\\ &+i\left(\vec{k}\cdot\vec{v}_g-\omega\right)\phi(\vec{k},\omega)+\sum_{\substack{\omega=\omega_1+\omega_2\\ \vec{k}=\vec{k}_1+\vec{k}_2}} V^Q_{1,2}\phi(\vec{k}_1,\omega_1)\phi(\vec{k}_2,\omega_2).\end{aligned} \tag{3.20}$$

On the left hand side, the first term of Eq. 3.20 represents the change of the complex wave amplitude in time while the second is the convection in space at the group velocity. On the right hand side, the first term denotes the linear growth of the wave γ_ω. This physically is the rate at which energy is extracted from the background plasma as the mode propagates. The second term corresponds to the dispersion of the waves. The third term represents the change in the complex amplitude due to three-wave coupling interactions that satisfy $\vec{k} = \vec{k}_1 \pm \vec{k}_2$ and $\omega = \omega_1 \pm \omega_2$. The coefficient $V^Q_{1,2}$ is a weighting function for the strength of each three-wave interaction and is related to the second order dielectric response.

Eq. 3.20 is a framework for relating change in wave amplitude to linear growth and nonlinear contributions. To translate this result into a form that can be analyzed

experimentally, we take the Fourier transform with respect to time:

$$\vec{v}_g \cdot \frac{\partial \hat{\phi}_f}{\partial \vec{r}} = \left(\gamma_f + i\vec{k}_r \cdot \vec{v}_g\right) \hat{\phi}_f + \sum_{f=f_1+f_2} V_{1,2}^Q \hat{\phi}_{f_1} \hat{\phi}_{f_2}, \tag{3.21}$$

where we have introduced ϕ_f, the complex amplitude of the Fourier transform at frequency, $f = \omega/2\pi$ in the EDI spectrum. We note that in translating Eq. 3.20 to Eq. 3.21, we have made the approximation that if there is a set of frequencies f_1, f_2 that satisfies $f_1 \pm f_2 = f$, there is only one set of wavevectors, $\vec{k}_1, \vec{k}_2$, that satisfies $\vec{k}_1 \pm \vec{k}_2 = \vec{k}$. This is consistent with the form of the EDI that applies to our plasma and allows us to simplify the summation in Eq. 3.21 to frequency combinations.

As a next step, to arrive at a method for experimentally inferring the growth, we consider Eq. 3.21 in the context of the configuration shown in Fig. 3.6 where two electrostatic probes are separated in the azimuthal $\hat{y}$ direction by distance, Δy. These probes simultaneously measure the time-based Fourier spectrum at each location to yield $X_f = \hat{\phi}_f(y)$ and $Y_f = \hat{\phi}_f(y + \Delta y)$. Based on these two measurement locations, we can discretize Eq. 3.21 with respect to the azimuthal coordinate to find

$$Y_f = L_f X_f + \sum_{f=f_1+f_2} Q_f^{1,2} X_{f_1} X_{f_2}, \tag{3.22}$$

where we have defined linear and nonlinear transfer functions $L_f = \left(\left[\gamma_{f(y)}/v_{g(y)} + ik_y\right]\Delta y + 1\right)$ and $Q_f^{1,2} = (V_{1,2}^Q/v_{g(y)})\Delta y$. Here we have introduced the azimuthal linear growth rate, $\gamma_{f(y)} = \gamma_f - \mathrm{Re}\left(X_f^{-1}\left[v_{g(x)}\partial_x X_f + v_{g(z)}\partial_z X_f\right]\right)$. This reflects the fact that the observed change in the amplitude of each mode in $\hat{y}$ is a projection of the total growth rate from three dimensions. Finally, we multiply Eq. 3.21 by the complex conjugate

quantities, X_f^* and $X_{f_1}^* X_{f_2}^*$ respectively, to yield

$$Y_f X_f^* = L_f X_f X_f^* + \sum_{f=f_1+f_2} Q_f^{1,2} X_{f_1} X_{f_2} X_f^* \tag{3.23}$$

$$Y_f X_{f_1}^* X_{f_2}^* = L_f X_f X_{f_1}^* X_{f_2}^* + \sum_{f=f_1+f_2} Q_f^{1,2} X_{f_1} X_{f_2} X_{f_1}^* X_{f_2}^*.$$

The first equation is the complex form of a discretized wave energy equation. The second represents the third moment of the wave-dynamics, also known as the cross-bispectrum.

With experimental measurements of the moments in Eq. 3.23, the system can be solved for the linear and nonlinear transfer functions. In turn, from these values, we can infer key properties of the wave dynamics including the azimuthal growth rate, $\gamma_{f(y)} = (\mathrm{Re}[L_f] - 1)(v_{g(y)}/\Delta y)$ and the nonlinear power transfer function:

$$T_f = (v_{g(y)}/\Delta y)\mathrm{Re}\left[\sum_{f=f_1+f_2} Q_f^{1,2} X_{f_1} X_{f_2} X_f^*\right]. \tag{3.24}$$

This last term physically represents the energy flux transferred to the mode of frequency f by nonlinear coupling from other modes in the spectrum.

We solve the governing equations following the algorithmic approach developed by Ritz [82] and later modified by Kim [86]. We note here that while in this previous work, the governing equations were inferred from a spatial Fourier transform of Eq. 3.20, we have derived the governing equations in terms of the time-based Fourier transform. We adopted this approach because it was not possible to insert a sufficient number of probes in our small scale plasma to perform spatial Fourier transforms. Despite our use of a different transform, the form of equations remains the same and thus the same algorithm can be applied. To this end, this analysis method has two key requirements. The first is ensemble averaging the various moments in Eq. 3.23 over multiple measurements[85]. This reduces the stochastic noise such that the higher

order moments can be accurately resolved. The second requirement is that the ensemble averaged power spectra, $P_f = \langle X_f X_f^* \rangle \approx \langle Y_f Y_f^* \rangle$, are stationary between the two probe locations[86]. This assumption is justified by the azimuthal symmetry of the discharge (Fig. 3.6).

As a last step before we can leverage experimental data to solve the governing equations for key terms like L_f and T_f, we need an estimate of the group velocity of the waves. While in principle we could measure this group velocity directly from experimental measurements of the dispersion, $\omega(k_y)$, spatial aliasing from the probe spacing precluded a direct measurement of the wavenumbers of interest. This aliasing limitation is discussed at length in Ref. [15] and the previous section.

3.4.5 Design Guidelines and Probing Techniques

Based on the operating principles outline in the previous section we summarize several key design guidelines used to construct the wave probe, configure the measurement circuit, inject the probes into the plasma, and interpret the results. In terms of physical construction we choose the probe radius and length such that it was much longer than it was wide: $r/L = 1/10$. This kept the probe sheath at the tip small relative to length of the probe so Equation 3.1 remains valid. On the other hand, the assumptions about the thin-sheath can be violated. We note that for the the ratio of our probe radius to the Debye length (10-15 throughout the plume), there are regions where the ion collected current is in the so-called transitional sheath domain[70]. However, in applying the more complete expressions for ion saturation introduced in Ref. [70], we found this only led to an error of less than 15% compared to the thin sheath approximation. For the remainder of this work, we therefore assume $\tilde{i}/\bar{i} \approx \tilde{n}/\bar{n}$ valid to within $\sim$15%. Specifically, the probes consisted of 0.38 mm radius tungsten rods with an exposed length of 3.8 mm. This radius is also small compared to the width of the Hall thruster discharge channel which can help reduce perturbations to

the plasma as the probes are inserted into the plume[90]. Tungsten is used as the electrode because it can survive the high temperature expected in the Hall thruster acceleration zone. The rest of probe consists of telescoping alumina rods (Fig. 3.3 that insulate the wire connected to the tungsten tip from the plasma. From the probe the signal is passed through a double-shielded coaxial cable with low line inductance and capacitance, this helps shields the probe signal wire from spurious pick-up of noise. Finally, the circuit terminates inside an enclosed metal measurement box electrically connected to ground. Inside the measurement box the bias voltage to the probe supplied by four 9 Volt batteries connected in series and also in series with 100 Ohm low-inductance metal foil resistor. The combined -36V applied with batteries place the probe potential well below the typical floating voltages observed in Hall thrusters[44]. A metal foil resistor was chosen to allow high bandwidth measurements into the 10 MHz domain that might otherwise be attenuated from the relative high inductance in wire-wound resistors. The voltage drop across this resistor is measured by an Alazar ATS9462 16-bit digitizer sampled at 100 MHz. This allow for measurement of up to 50MHz signals based on the Nyquist criteria discussed in the previous section. Additionally, the dimensions of our probe, combined with the expected mean density level, provide a sufficiently large collected current to resolve less than 0.01% fluctuations in relative density with our data acquisition system. In theory, resolution of weaker fluctuations is possible with a larger probe area by making the probe tip longer, but this decreases the overall spatial resolution of the measurement.

The final probe dimensions for the experimental setup were chosen to meet the constraint that the probe can accurately measure the hypothesized plasma oscillations within the bit resolution of the digitizer circuit. Although our probe collects ion saturation current, the actual measurement is the voltage drop across a sensing resistor, typically ranging from 100 to 1000 Ohms. Therefore, the detection limit of the diagnostic for small amplitude oscillations is determined by the measurement

voltage resolution. As a general rule, we aim for the minimum expected signal size to be at least 10 times the bit limit to ensure that we have a smooth signal for Fourier analysis. The design equation is formulated as follows:

$$10V_{bit} < R_{sense}\frac{\tilde{i}_{sat}}{\bar{i}_{sat}} \exp -\frac{1}{2}en_{i0}A_s\sqrt{\frac{eT_e}{m_i}}. \tag{3.25}$$

where V_{bit} is the limit set by the digitizer, R_{sense} is the resistance of the sense resistor, and $\frac{\tilde{i}_{sat}}{\bar{i}_{sat}}$ is treated as an independent variable informed by prediction or simulation of the expected plasma oscillations. V_{bit} is fixed based on available hardware and R_{sense} has a limited allowable range for minimizing perturbations of probe voltage[70]. Therefore the probe area is sized to satisfy this relation based on the expected mean plasma density and normalized oscillation amplitudes. Increasing probe area is the only way of meeting this requirement outside of better measurement hardware, but there are two limits on the maximum probe size the constrain the design.

The first limitation involves a simple trade-off between spatial resolution and signal strength. Since we are using cylindrical Langmuir probes, we have the constraint that $r/L <= 1/10$. As we increase the probe area, both the radius and length must also increase, consequently reducing our spatial resolution because we are averaging the oscillations over the physical area of the probe tip. The second limitation stems from the effects of finite probe size on oscillation wavelengths that are on the order of or smaller than the probe diameter. For example, as illustrated in Figure 3.7, if the wavelength is significantly smaller than the probe, then the various peaks and troughs of the plasma oscillations will be averaged across the surface of the probe area, smoothing out and potentially obscuring the oscillations entirely. As discussed in the previous chapter, we expect the relevant plasma oscillations to be very small, on the order of millimeters or smaller. Therefore, it was highly likely that we would encounter this issue in our experiments. To address this, we performed a suite of simulations to infer how the effects of finite probe size might manifest in our measured

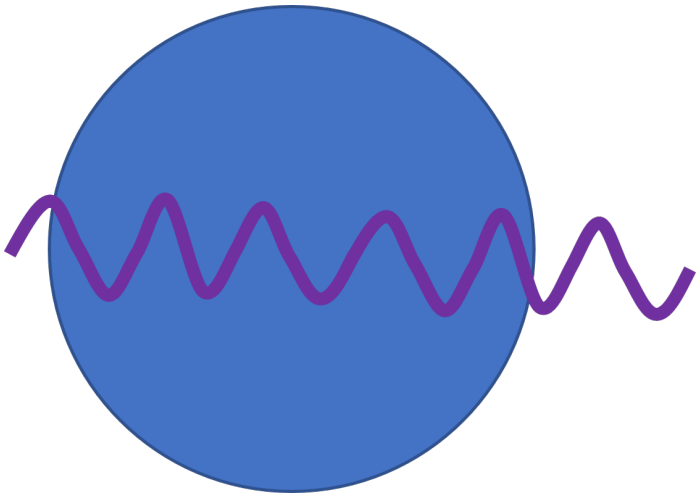

Figure 3.7: Example of plasma oscillations with wavelength smaller than geometry of measuring wave probe.

data.

Over a 3D grid we modelled two cylindrical wave probes arbitrarily spaced apart by several probe diameters, see Figure 3.8, and simulated a family of propagating plasma oscillations. To model the plasma oscillations we used Eqn.3.6 in reverse where we supplied a set of oscillation wavenumbers, frequencies/phase speed, and amplitude that represent a linear ion-acoustic like dispersion but with constant amplitude versus wavelength. For each time point we took the simulation ion saturation current that we would measure in experiment as the sum of the saturation current contribution from each grid point, noting that each grid point will have varying local density due the plasma oscillations. On top of this signal we also superimposed white noise to better reflect laboratory conditions. From this data we can reconstruct a simulated time-series of probe saturation current and perform the Fourier and Beall analysis outlined in the previous sections.

The resulting analysis shown in Figures 3.9 and 3.10 demonstrates several of the features discussed previously, such as aliasing around the edges of the wavenumber bins, but also a new behavior in the measured amplitude. While we specified a constant amplitude spectrum across wavenumber the simulation showed that once

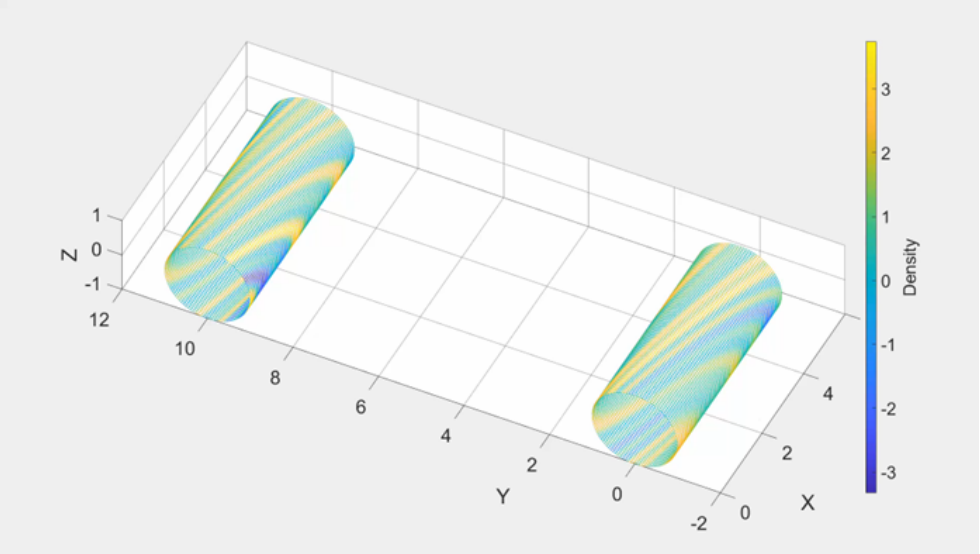

Figure 3.8: Simulated wave probes and plasma oscillations, spatial positions are normalized by probe radius and relative plasma density is scaled arbitrarily.

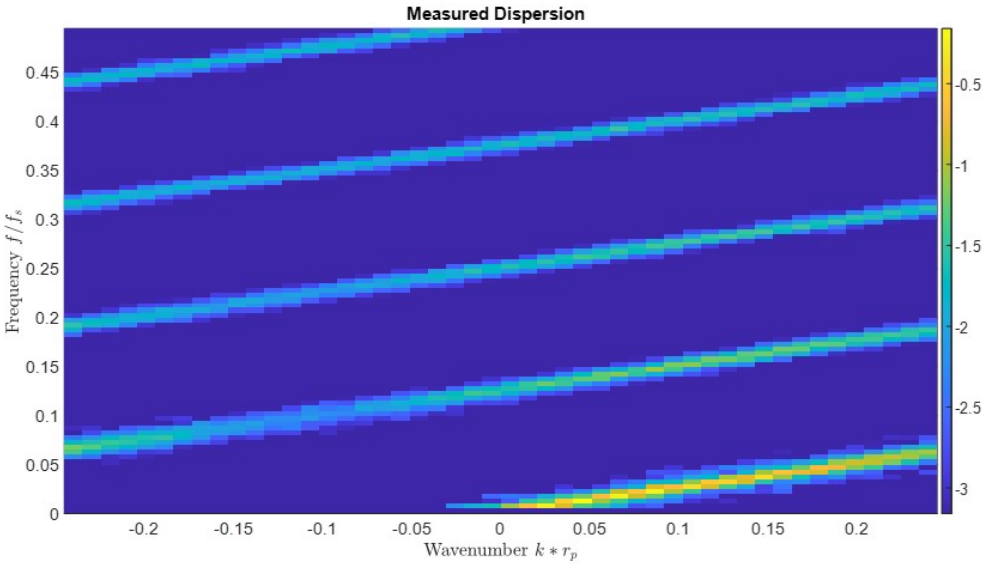

Figure 3.9: Beall plot for simulated ion-acoustic like wave propagating across two cylindrical probes. Frequency is normalized by the sampling frequency and wavenumber is normalized by probe radius.

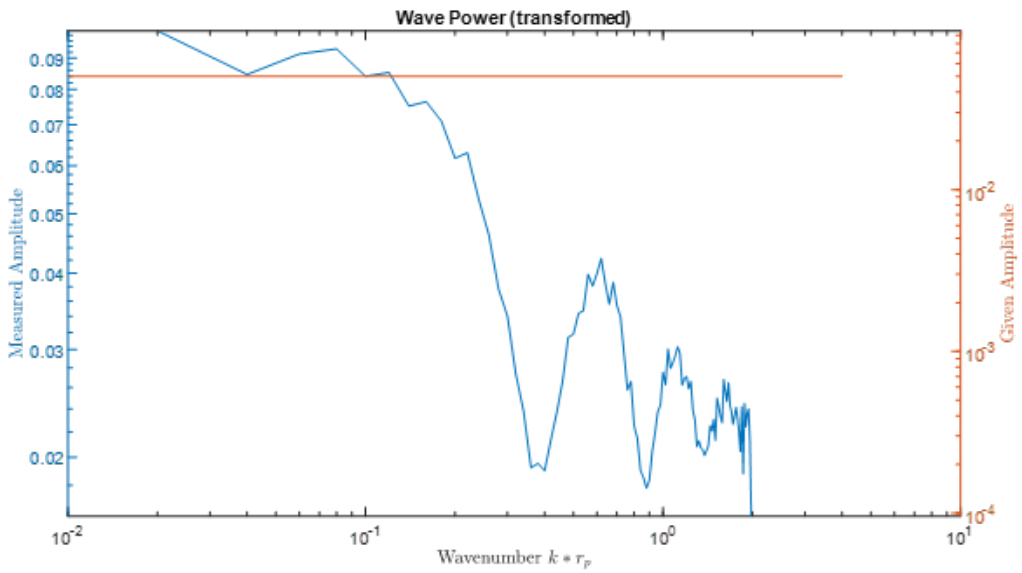

Figure 3.10: Power spectrum density for simulated ion-acoustic like wave propagating across two cylindrical probes. Frequency is normalized by the sampling frequency.

the wavenumber starts approaching $kr_p = 0.2$ the measured amplitudes begin to decay. This occurs before encountering resonance points near multiples of the probe diameter, where the amplitude is still diminished but to a lesser extent. Though even across the various resonances the peak amplitude is still decaying with increasing wavenumber. Since we expect the plasma oscillations of interest to have resonant like behavior this means any data must be reviewed to infer if the observed spectrum and amplitudes are due to plasma behavior or probe effects. In our experiments, we verified this at multiple occasions by using two probes with different radii and confirming that the measured spectra were the same amplitude for both probes. If we were observing effects of finite probe geometry then the spectra should have been noticeably different for each probe signal.

Finally, in order to provide spatially-resolved measurements, we implemented a high-speed injection technique to insert probes into the thruster discharge. Following Refs. [45, 57, 43], this high-speed reciprocating sampling helped limit probe damage that can result from prolonged exposure to the energetic near-field plasma and min-

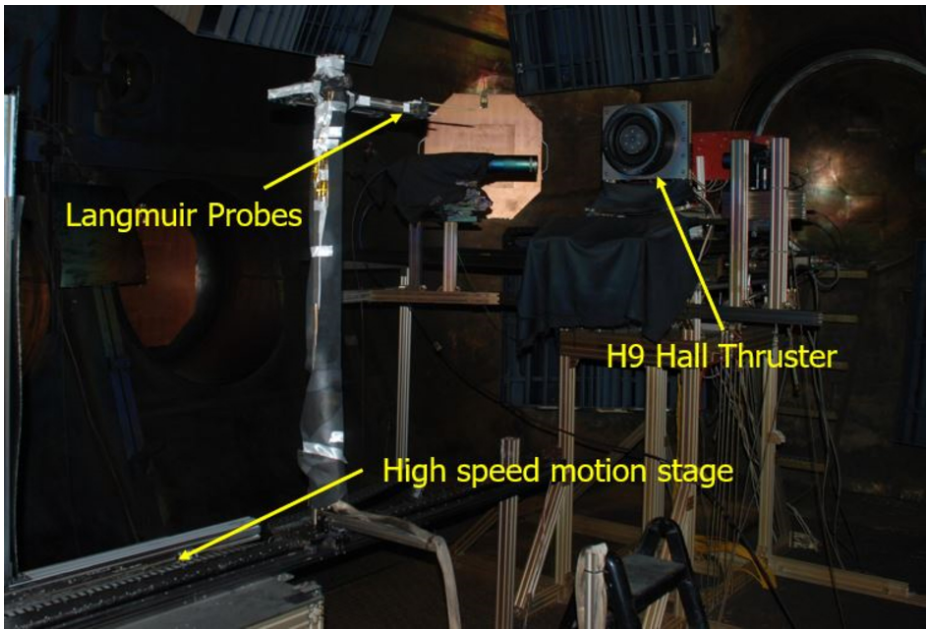

Figure 3.11: Photo of the H9 experimental setup in the Large Vacuum Test Facility. Diagnostics and motion stages are highlighted

imize perturbations to the plasma. The probes were mounted on a linear induction motion stage (Fig. 3.11) that translated from the exit plane of the thruster at 50 cm/s with the ion saturation current signal recording continuously at 100MS/s. For our studies, we typically injected our probes along the thruster channel centerline from a location of $z/L = 1$ to $z/L = 3$ where L denotes the length of the channel and z is the distance from the anode. Refs. [45, 57, 43] have shown that active probing can perturb thruster plumes. In order to assess whether the probes were impacting the plasma in this experiment, we monitored two key global properties of the discharge, the DC current and its oscillations, as the probes were inserted. The power spectrum of the discharge current did not change with respect to the position of the probes unless they were injected past the exit plane and into the discharge channel. For all results presented in this work we restricted our measurement domain only to the region downstream of the exit plane. We note, however, that as discussed in Jorns et al.[57], global metrics do not necessarily indicate that the plasma is undisturbed. It should be kept in mind that it is possible that the plasma in our configuration still was

impacted by the probe insertion. In addition to the high-speed injection method, we also collected wave fluctuation data at fixed positions between 0.5-1 channel lengths downstream of the exit plane. Here the probes were far enough from the thruster that they were able to sample data for longer periods without damage. These fixed position measurements yielded an order of magnitude more samples at a particular position than the high-speed method and thus provided higher spectral resolution. These probes focused on lower frequency oscillations and were sampled at 10MS/s. For both measurement methods the experiment was repeat with wave probes oriented in the axial, azimuthal, and radial direction.

3.5 Laser-Induced Fluorescence Measurements

When making comparisons between the measured wave properties and the theoretical form of the EDI it is necessary to estimate the plasma parameters in the EDI dispersion relation (Equation 2.24). Furthermore, when we calculate the wave-driven electron transport we need a baseline value to validate against. Due to the difficultly of using physical probes to directly measure several of these properties we employed laser-induced-fluorescence(LIF) diagnostics make these measurements. LIF is a technique commonly used for measuring the ion velocity distribution function in Hall thrusters[72, 83, 29, 20]. LIF operates by exciting a metastable state with a laser at wavelength λ_0 and measuring the emitted fluorescence. By varying the laser wavelength slightly from the transition wavelength some portion of the ion population will still fluoresce because ions with the correct velocity will Doppler shift the detuned laser wavelength to the proper transition. By measuring the signal as a function of detuned wavelength ion velocity distribution function(IVDF) can be determined. Additionally, by measuring the IVDF as several axial position and using an analysis technique developed at the University of Michigan, by Ethan Dale, several other plasma parameters can be inferred. We describe briefly here the analysis methodology

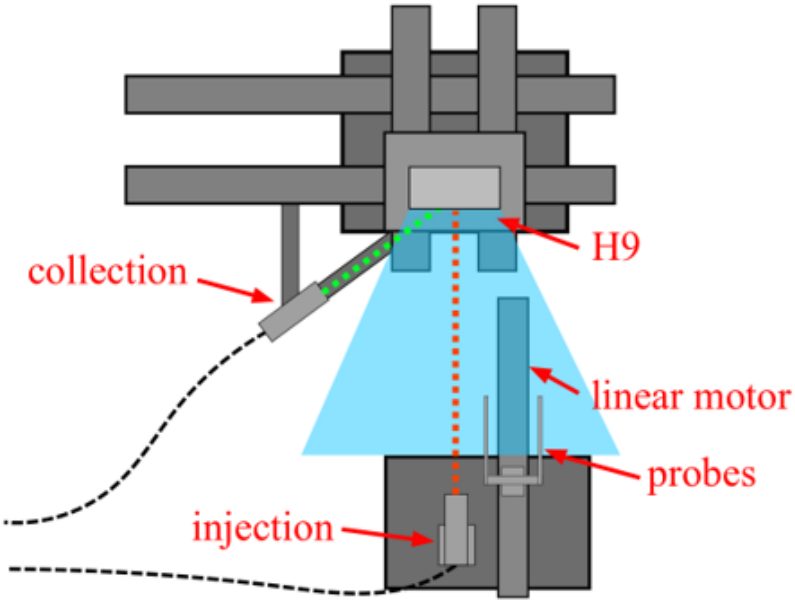

Figure 3.12: Experimental setup showing configuration of LIF diagnostics relative to the Hall thruster and wave probes.

noting that a complete description can found in Ref. [28].

This analysis method, known as the ion Boltzmann implicit solution method (IBIS), starts with the 1D ion Boltzmann equation where ionization collisions are considered:

$$\frac{\partial f}{\partial t} + u_i \frac{\partial f}{\partial x} + \frac{e}{m_i} E_x \frac{\partial f}{\partial u_i} = \left(\frac{\partial f}{\partial t}\right)_{iz}. \tag{3.26}$$

In this equation u_i is the axial ion velocity, E_x is the axial electric field, and the right most term is the time rate of change in the IVDF due to ionization. Assuming the IVDF is at steady state in time, higher order moments of the Boltzmann equation can be taken to yield equations containing several of the need plasma parameters:

$$\frac{\partial \overline{u_i} n_0}{\partial x} = n_0 f_{iz} \tag{3.27}$$

$$\frac{\partial \overline{u_i^2} n_0}{\partial x} - \frac{e}{m} n_0 E_x = 0 \tag{3.28}$$

$$\frac{\partial \overline{u_i^3} n_0}{\partial x} - 2\frac{e}{m} n_0 E_x \overline{u_i} = 3\frac{e}{m} T_n n_0 f_{iz} \tag{3.29}$$

Here $\overline{u_i}$ is the mean ion velocity and T_n is the temperature of the neutral xenon gas. With the spatial resolved LIF measurements, this system can be solved for E_x, f_{iz}, and $d\ln(n_0)/dx$. This last variable can then be integrated across the axial domain to determine the ion density if the density is known at one of the boundary point x_b:

$$n_0(z) = \exp\left[\int_x^{x_b} \frac{d\ln n_0}{dx}\right] + n_0(x_b) \tag{3.30}$$

This downstream density ($n_{i(0)}(x_b)$ is estimated with the wave probes that also function as ion saturation probes for measuring ion density. With this information, in addition to the value of the applied magnetic field, we can calculate an effective total electron collision frequency ($\nu_e = \nu_c + \nu_{AN}$) using Ohm's Law

$$\nu_e = \frac{\Xi \pm \sqrt{\Xi^2 - \left[2v_{ex(0)}B_r\right]^2}}{2\frac{m_e}{e}v_{ex(0)}} \tag{3.31}$$

where $v_{ex(0)}$ is the axial electron velocity and we define $\Xi = E_{x(0)} + \frac{\nabla q n_{e(0)} T_e}{n_{e(0)}} - \eta_i j_i$, where $\eta_i = m_i\nu_c/q^2 n_{i(0)}$ is the classical ion resistivity due to collisions and j_i is the ion current density. All parameters in Eq. 3.31 are determined from the solution of Eqs. 3.27-3.29 except for the classical collision frequency, axial electron velocity, and electron temperature.

We determine the electron temperature from the calculated ionization frequency f_{iz} using tabled values of the ionization rate $\xi_i(T_e) = f_{iz}/n_n$ where n_n is the neutral density (cf. Ref. [42]). Although, this technique requires an estimation of the neutral density profile. We calculate the neutral density using the conservation equations for the neutral fluid combined with our calculated ionization frequency and an estimate of the downstream neutral density. The boundary condition for the neutral density was guided by previous experimental measurements in literature[51].

The axial electron velocity is determined through the ion and electron continuity

equations. If the ions and electrons are restricted to one dimensional, axial, flow the electron current density is the difference between the total discharge current density j_d and the ion current density: $j_e = j_d - j_i$. While the ion current density is known from the measured beam velocity and plasma density, the discharge current is assumed to be the total discharge current (I_d) uniformly distributed over the channel area A_{ch} of the thruster: $j_d = I_d/A_{ch}$. Subject to these assumptions the electron velocity is given by

$$v_{ex(0)} = \frac{I_d}{n_{i(0)} A_{ch}} - v_{i(0)} \tag{3.32}$$

where we have assumed $n_{e(0)} \approx n_{i(0)}$ by quasi-neutrality.

Finally, the classical collision frequency is calculated using the Spitzer collision frequency equations for electron-neutral and electron-ion collisions(cf. Ref. [42]). Therefore, the IBIS method provides an estimate of anomalous collision frequency by subtracting the classical collision frequency from the calculated total collision frequency in Eq. 3.31. This serves as a baseline value we shall compare our wave-driven collision frequencies against. Additionally, the background plasma parameters determined by the IBIS method can be used to solve the dispersion relation of the EDI for estimating a theory-driven anomalous collision frequency.

3.6 Conclusion

In summary our experimental methods breakdown into three core components. First, we use ion saturation probes and Fourier analysis to determine the amplitude and dispersion of any waves present in Hall thruster plumes. This information allows us to identify what type of wave is present. Once the wave is identified we use the bispectral analysis technique of Ritz and Kim to infer the linear growth rate and any non-linear process governing the evolution of the observed instability. Finally, we use LIF measurements and the IBIS method to infer background plasma parameters.

Taken together these data sets allow for a calculation of the anomalous wave-induced electron collision frequency. The IBIS method also calculates the actual anomalous collision frequency for use in validate the results infered from the wave probe analysis.

CHAPTER IV

Investigation of High Frequency Instabilities in Hall Thruster Plume

4.1 Introduction

In this chapter, we present the results of wave probe study performed to investigate the dispersion relation of instabilities in the Hall thruster plume. First, we highlight the specifics experimental questions being addressed by this study. Second, we briefly review the experimental setup and note and differences from the general experimental setup described in Chapter III. Then present the spatial resolved measurements of power spectrum and dispersion.

Despite the growing body of correlational evidence pointing to the important role of the EDI for electron transport in Hall thruster, there are a number of questions about the nature of this instability in the Hall thruster that have yet to be addressed experimentally. Perhaps the most pressing is whether this wave actually exists in the so-called acceleration region of the thruster. This is a critical consideration since this zone, where the electric and magnetic fields are highest, is fundamental to the operation of Hall thrusters. It is where the majority of ion acceleration occurs. Understanding the mechanisms driving transport in this region is therefore paramount. With that said, although numerical simulations suggest that the EDI should be the

dominant contributor to electron transport in this critical region, experimental measurements have not been able to access it. Although there were a few Thomson scattering experiments that have measured supposed EDI[101], the results were results were incomplete as the accessible wavenumber range was limited, a peak in oscillation amplitude could not be found in the wavenumber domain, and all measurements were performed downstream in the downstream plume where the electric and magnetic fields are weaker. As a result, it ultimately is not known if the EDI exists in the acceleration zone, or even if it does appear in this region, it is not clear that it would exhibit the same features (dispersion and energy content) as those reported for measurements performed downstream. This is a crucial consideration as the shape of the wave spectrum and its dispersion both mediate the interaction of the EDI with the electrons. Faced with this uncertainty about the EDI in the acceleration zone, there is a pressing need for experimental efforts to examine the plasma oscillations in the thruster and to document if and how the measured properties are connected to previous experimental and numerical work on this problem. To this end, the goal of this work is to characterize the spatial evolution of the plasma oscillations–their energy content and dispersion—as a function of position in a Hall effect thruster.

4.2 Experimental Setup

Our general procedure in this experiment matches the wave probe methods outlined in Chapter III, and thus we only summarize the key components here. We employed a set of translating cylindrical Langmuir probes biased to ion saturation current to characterize the plasma oscillations in the plume of the H9 thruster. The probes consisted of 0.38 mm radius tungsten rods with an exposed length of 3.8 mm. the current collected on these probes is proportional to the ion density, $i_{sat} \propto n_i$ and therefore measures oscillations in plasma density. We injected multiple, spatially-separated probes into the plasma and measured correlations in their signals to infer

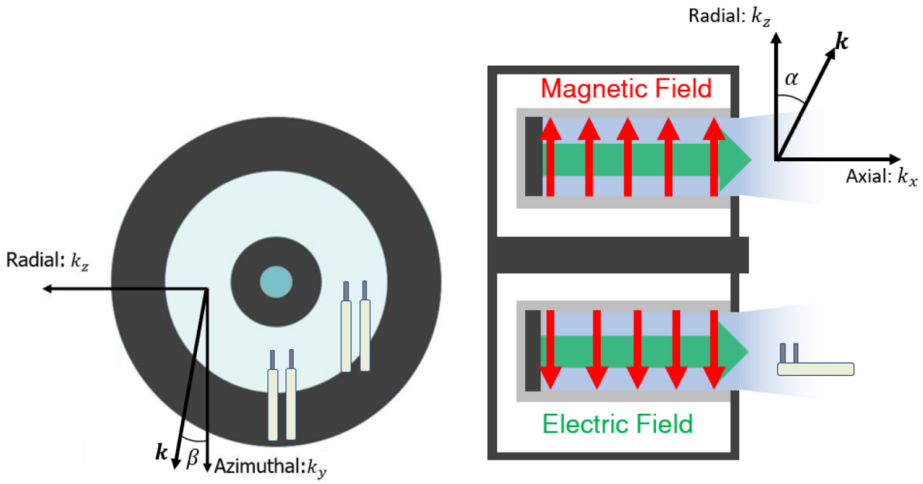

(a) (b)

Figure 4.1: Schematic of Langmuir probes during interrogation of each wavevector component: a) Azimuthal and radial b) Axial.

the dispersion of the fluctuations in ion saturation density. We employed two probes in three orientations for this purpose (see Fig.4.1) to measure the axial, radial, and azimuthal components of the oscillations. In each case, the tips were separated by 4.7 mm allowing direct measurement of wavenumbers between -688 and 688 rad/m. This separation (several Debye lengths) was dictated by the need to prevent the sheaths from the probes from overlapping.

In order to provide spatially-resolved measurements, we implemented a high-speed injection technique to insert probes into the thruster discharge. The probes were mounted on a linear induction motion stage that translated into plume of the thruster at 50 cm/s. Measurements performed using two techniques. The first with the ion saturation current signal recording continuously at 100MS/s. This long waveform is then binned into smaller waveforms as a function of the motion stage position. The allows high fidelity spatial resolved measurements of the power spectrum and dispersion relation. We injected these probes along the thruster channel centerline from a location of $z/L = 1$ to $z/L = 3$ where L denotes the length of the channel and z is the distance from the anode. Refs. [45, 57, 43] have shown that active probing can

perturb thruster plumes. In order to assess whether the probes were impacting the plasma in this experiment, we monitored two key global properties of the discharge, the DC current and its oscillations, as the probes were inserted. The power spectrum of the discharge current did not change with respect to the position of the probes unless they were injected past the exit plane and into the discharge channel. For all results presented in this work we restricted our measurement domain only to the region downstream of the exit plane. We note, however, that as discussed in Jorns et al.[57], global metrics do not necessarily indicate that the plasma is undisturbed. It should be kept in mind that it is possible that the plasma in our configuration still was impacted by the probe insertion. Our second measurement technique collected wave fluctuation data at fixed positions between 0.5-1 channel lengths downstream of the exit plane. Here the probes were far enough from the thruster that they were able to sample data for longer periods without damage. These fixed position measurements yielded an order of magnitude more samples at a particular position than the high-speed injection method and thus provided higher spectral resolution. As we will discuss, these probes focused on lower frequency oscillations and were sampled at 10MS/s.

4.3 Results

4.3.1 Spatially-resolved power spectra

We show in Fig. 4.2a an example of the raw ion saturation current collected by one of wave probes as it was injected along thruster centerline. The decrease in magnitude with normalized distance from the exit plane is an indication of the drop in density as the plume is expelled from the thruster. The properties of interest to us in this study, however, are the small-scale fluctuations that occur on top of this curve. In order to analyze these properties and relate them to spatially-resolved measurements

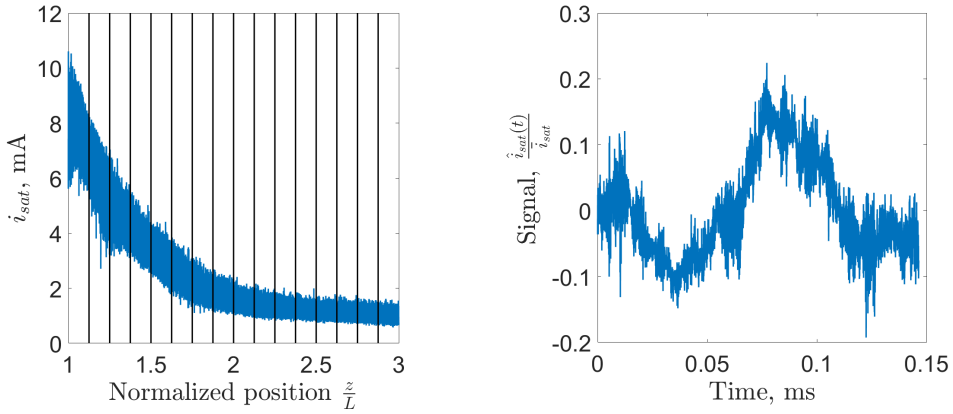

Figure 4.2: a) Ion saturation current as function of position during probe injection. An example of the spatial binning (vertical lines) used to generate spatially-resolved dispersion relations is shown. b) The relative density perturbations as function of time in one of the 200 time samples of a spatial bin.

of the wave properties, we employed the following analysis. First, we binned the data from each probe by axial location (shown notionally as vertical lines in Fig. 4.2a) into sixteen segments. We then subdivided the data in each bin into 200 sequential time segments and divided the signal by the time-averaged density in each sample ($\tilde{i}_{sat}/\bar{i}_{sat}$). Per our discussion from the previous section, this yielded an estimate of ($\tilde{n}_i/\overline{n}_i$). An example of one of these 200 time series from a spatial bin is shown in Fig. 4.2b. We next applied a Fourier analysis on each of the 200 time-varying signals in the spatial bin and averaged to yield a power spectrum of the average spectral content of the fluctuations at each spatial location. Figure 4.3 shows a sample result of this analysis, plotting the power spectrum intensity as a function of frequency and position in the plume where the distance from the anode (z) has been normalized by the length of discharge chamber (L).

As can be seen from Figure 4.3, the dominant feature consists of well-defined fluctuation bands in the MHz domain that are spaced approximately 3MHz apart up to 20MHz. Upstream of the peak magnetic field, denoted by the dashed black line at $z/L = 1.3$, the spectral content of the lower frequency harmonics is at its

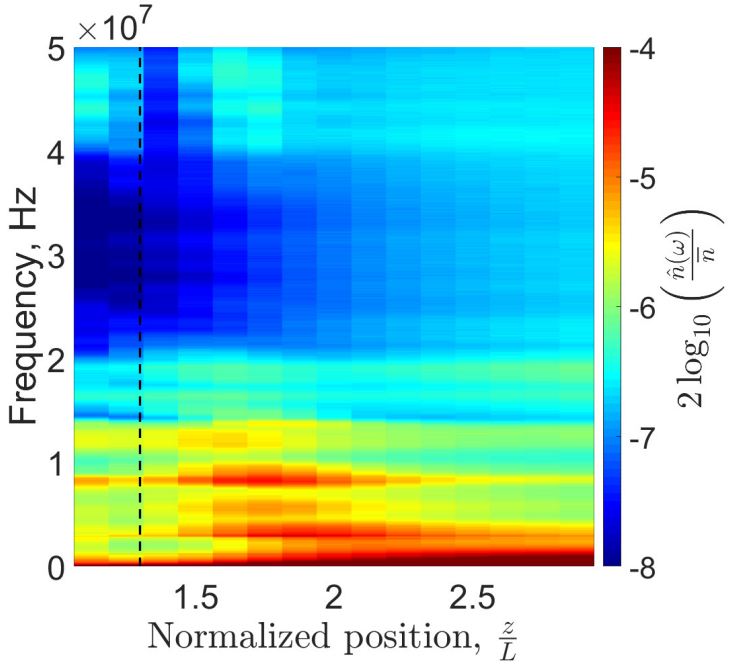

Figure 4.3: Power spectrum as a function of normalized position along channel centerline of the Hall thruster. Distance from the anode z is normalized by the discharge chamber length L. The location of the peak magnetic field at $z/L = 1.3$ is indicated by a dashed black line.

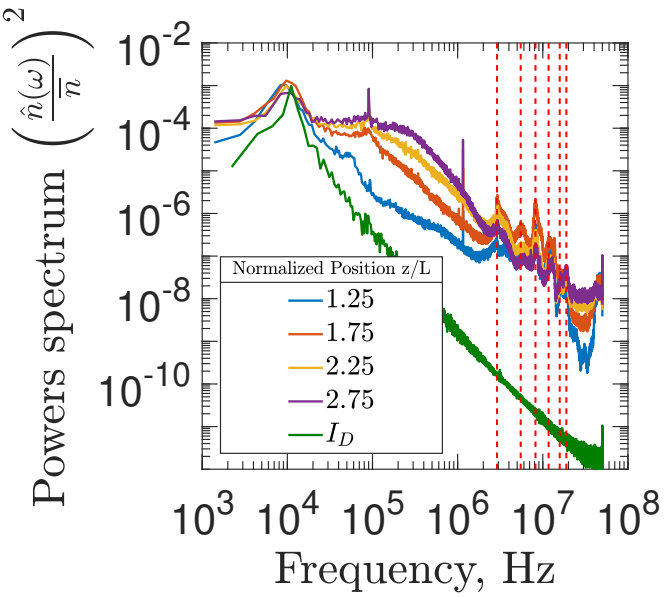

Figure 4.4: Power spectra along channel centerline using only 4 spatial bins. Megahertz peaks are highlighted with dashed red lines. The discharge current power spectrum is also shown for reference.

weakest and approximately constant as a function of position. Half a channel length downstream of the exit plane, the relative amplitudes of the megahertz fluctuations spike before decaying downstream and oscillations spanning the 100-500 kHz domain develop. The magnitude and spacing of these frequencies, which are below the local ion plasma frequency, is qualitatively consistent with the linear dispersion of the EDI introduced in Sec. II. This spectral content therefore is the central focus of this investigation. As an aside, we note that this plot also shows that there is spectral content in the vicinity of 45MHz before and after the location of peak magnetic field strength ($z/L = 1.3$), but this frequency is well above the ion plasma frequency which is considered the maximum for EDI oscillations. We therefore do not consider it further for this investigation. With that said, we do note that these oscillations occur in a similar frequency and wavenumber domain to previous high-frequency measurements of Lazurenko et al[67].

Due to the low spectral resolution of Figure 4.3, it is difficult to see unambiguously how the oscillations are changing at low (<1 MHz) frequencies. In order to better resolve the spatial evolution of spectral content in this region, we repeated our analysis with only four spatial bins. This yielded a finer frequency resolution of 1.4kHz. The resulting power spectrum in each bin is shown in Figure 4.4 where we have marked the resonances with red vertical lines. We now can see more clearly that the growth of low frequency broadband oscillations coincides with a decrease in power of the megahertz oscillations. We have also included for reference the power spectrum of the discharge current during probe injection in Figure 4.4. As discussed previous, the discharge current spectrum did not appreciably change in amplitude or spectral content during probe injection. Additionally, this result also illustrates that besides the breathing-mode oscillations at 10kHz, we do not observe the same high-frequency spectral content in the discharge current. This suggests that the wave probes are measuring plasma-borne modes. Lastly, although we see an evident sharp peak at 1

MHz in all of the results, this likely was electrical noise in the measurement circuit. Its unnormalized amplitude remained constant at all positions in the plume and was present even when the thruster was off.

While we reserve a full discussion of the implications of these findings for later., we note that these initial measurements already suggest that the EDI has a fundamentally different character in the acceleration region of the thruster as compared to the downstream. Indeed, we see in Fig. 4.4 that our measured spectrum downstream of $z/L = 1.75$ is dominated by a broadband, incoherent content between 100-500 kHz in agreement with previous experimental results that showed a broadband spectrum downstream. Moving upstream, where presumably the instability initially first grows due to the strong Hall drift in this region, we see that in fact the resonant structures in the megahertz domain become more dominant. This is consistent with initial linear growth and is in line with the simulation results that have been reported to date in 2D reduced dimensional kinetic models. Our results show an evident transition between these two states as function of position in the plume.

4.3.2 Spatially-resolved dispersion

Expanding on the conclusions from the previous section, we can apply additional analysis, known as Beall analysis, to the spatially-resolved ion saturation probe data to look for evidence of wave dispersion. Beall analysis follows from the cross-correlation Fourier analysis covered in Chapter III where if there is a wavenumber, k, along the line defined by the probes associated with oscillation frequency, ω:

$$k(\omega) = \frac{1}{\Delta x} \tan^{-1} \left[\frac{\mathrm{Im}(\mathcal{F}[i_{sat1}(t)]\mathcal{F}^*[i_{sat2}(t)])}{\mathrm{Re}(\mathcal{F}[i_{sat1}(t)]\mathcal{F}^*[i_{sat2}(t)])} \right], \tag{4.1}$$

where Δx is the distance between the probes, $\mathcal{F}, \mathcal{F}^*$ denotes the Fourier transform and its complex conjugate, and $i_{sat:1,2}$ is the ion saturation current from adjacent

probes 1 and 2. Following the approach of Beall et al.[6] that we discuss in-depth in Chapter III, we apply a histogram analysis to the same spatial and time bins from Figure 4.2 to generate intensity plots of frequency versus wavenumber at each spatial location. An example result taken from spatial location z/L = 1.5 is shown in Figure 4.5a with a frequency resolution of 22kHz and a wavenumber resolution of 27 rad/m^{-1}. The result in Figure 4.5a shows evident structure in the dispersion plots which are correlated with the well-defined resonances in the megahertz frequency range we noted in Figure 4.4. Indeed, at each band the wave is spread out across the wavenumber domain and in many cases appears to exhibit aliasing, i.e. phase wrapping on the k-axis. As we discussed in Chapter III this stems from cross-correlation having a finite range of directly measurable wavenumbers: $-\pi/\Delta x < k < \pi/\Delta x$. Oscillations with wavenumbers larger than the maximum value set by the probe spacing wrap around the wavenumber domain as they force in the measurable range of wavenumbers. This would suggest that the observed oscillations have dispersion, i.e. propagate, but the wavelengths are too small to resolve with our finite probe spacing. While aliasing in this context likely precludes us from making definitive comments on the dispersion (i.e. it is difficult to resolve any evident patterns), we return to a discussion of this in Section 4.4. where we show that the EDI could have a dispersion similar to the one we observe here.

We show in Fig. 4.5b dispersion relations at a location (z/L = 2) further downstream of the discharge exit. In this case, as expected from the power spectrum observations, the intensity plot is dominated by content at lower frequency. These plots with 22kHz frequency resolution do not have sufficient detail to resolve nuances in the dispersion structure, resulting only in an evident peak at the bottom of the Beall plot around $k = 200$ rad/m^{-1}. However, by using data from our fixed probes (mounted downstream) with higher spectral resolutions, we can appropriately resolve the dispersion features in this region. The Beall plots from this data are shown in

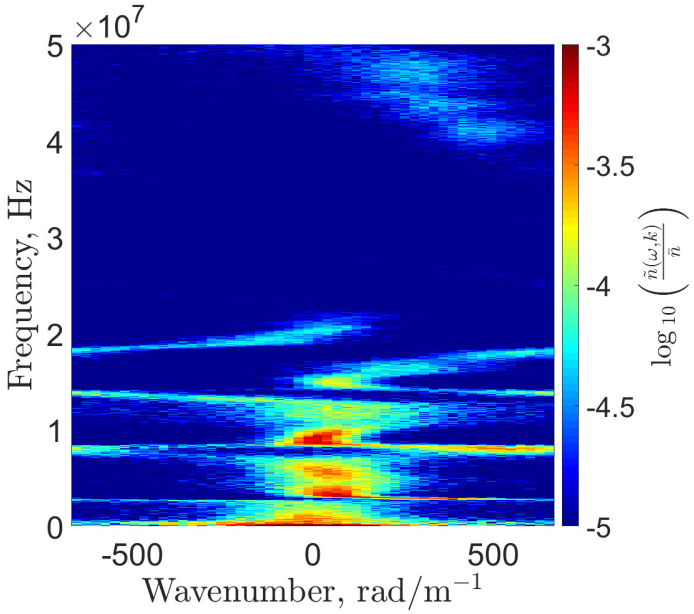

(a)

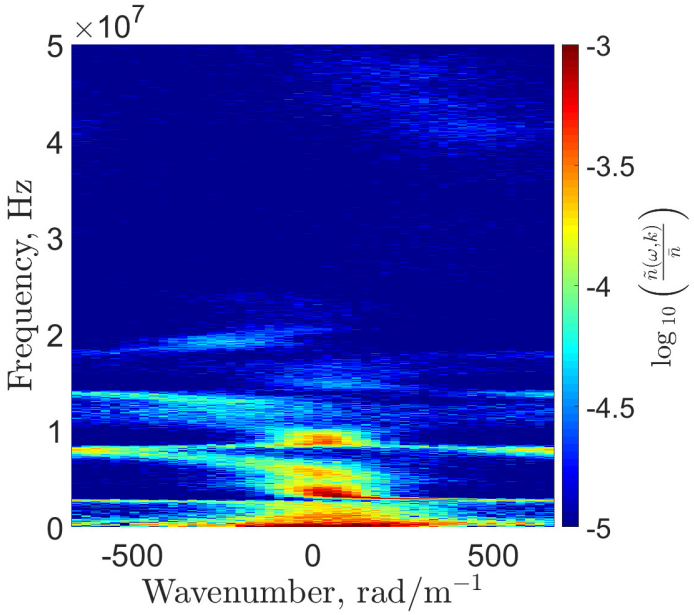

(b)

Figure 4.5: Beall plot for the azimuthal direction at (a) 1.5 L and (b) 2.0 L downstream of the anode and at channel centerline. The frequency resolution is 22kHz and the wavenumber resolution is 27 rad/m.

Figure 4.6 for each wave direction: azimuthal, axial, and radial, and show a linear dispersion in 50-500kHz domain. Although, this linear dispersion does not appear in the Beall plots until after z/L = 1.5, and upstream of this location there is no visible

dispersion in this frequency range. This linear behavior is consistent with the results of Tsikata et al. who reported a linear dispersion downstream[101, 100], though we note that our maximum resolve-able wavenumber is an order of magnitude lower than the ranges they reported. Physically, this result lends further support to the notion that the fundamental structure of the propagating oscillations changes with position, transitioning from the complex dispersion at higher frequency and small wavelength (Fig. 4.5a) to this more acoustic-like result downstream (Fig. 4.6a).

We can further quantify aspects of this acoustic-like dispersion by fitting lines to the intensity plots and multiplying the resulting slope by 2π to determine the wave speed. This yielded a phase velocity in each direction of 4, 10, and 50 km/s for the azimuthal, axial, and radial components respectively. This result suggests that the acoustic wave propagates primarily in the azimuthal direction but is tilted into the axial direction (α) by 20 degrees and into the radial direction (β) by -5 degrees; where negative wavenumbers denote propagation opposite the basis vector(see Figure 4.1). Functionally, this suggests that in addition to azimuthal propagation, the modes are also directed axially away from the thruster and radially inward. This stands in contrast to the work of Tsikata et al. [100] who measured that the modes propagate axially inward. The reason for this discrepancy is not known, though we note that physically, the fact that these acoustic modes in our measurements are directed away from the thruster is consistent with the notion that these oscillations are carried by the ions. In addition, the phase velocity in the azimuthal direction is commensurate with the ion sound speed which qualitatively is consistent with the EDI in the acoustic limit. This lends further support to the supposition that the modes have transitioned in this region to the acoustic limit.

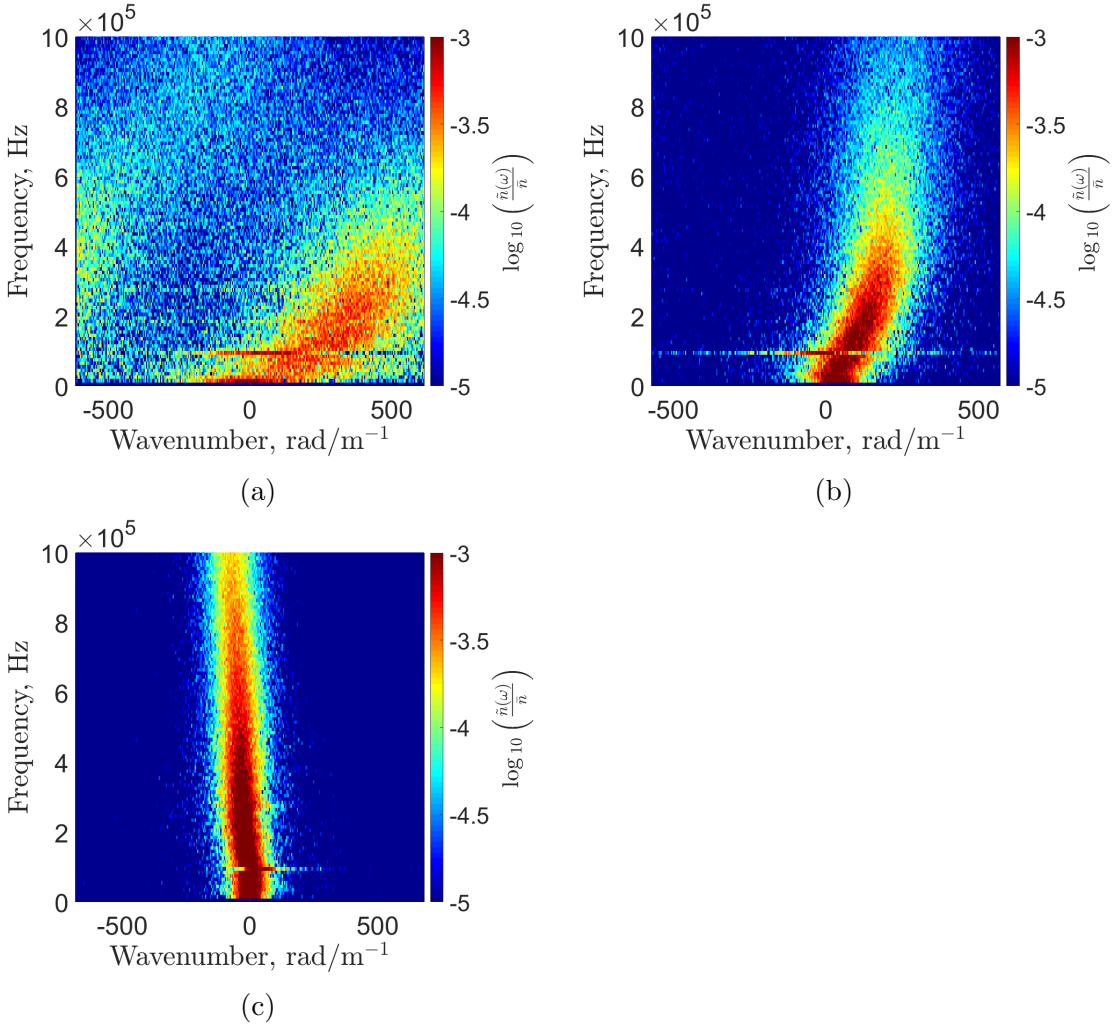

Figure 4.6: Beall intensity plots at z/L = 2 downstream of the thruster anode for each wavevector component: a) azimuthal, b) axial, c) radial. The frequency resolution is 5 kHz and the wavenumber resolution is 9 rad/m

4.4 Discussion

In light of the results presented in the previous section, we now can turn to the governing questions for this experiment: does the EDI exist in the acceleration zone, are its properties fundamentally different than EDI measurements downstream, and ultimately, how are the waves measured in these two zones connected? To this end, in the following section we begin by comparing the measured modes in the acceleration zone to the linear dispersion and then discuss the transition of the wave in the context of nonlinear transport across length-scales.

4.4.1 Comparison of measured dispersion and theory

We have shown the presence of two distinct oscillations: high-frequency resonant-like waves dominant near the exit plane and low frequency ion acoustic-like oscillations dominant further downstream. While we were able to demonstrate that the low-frequency content is comparable to the measured acoustic-like waves that have been reported in previous work, the nature of the high frequency modes at the exit plane is less evident. As discussed previously, while the frequencies are the right order of magnitude expected of EDI harmonics, the true wavenumber of our measured waves is likely obscured by aliasing effects and prevents a definitive comparison to the EDI. It is also important to acknowledge the possibility that these modes may be nonphysical–a result of probe induced effects. To this latter point, we recall that in monitoring the global metric for thruster operation, the discharge current, we found that the probe insertion did not change the oscillating character of the thruster. Moreover, this higher frequency content did not appear at any point in the discharge current power spectrum. This suggests that the measured waves are in fact a plasma borne mode. Even allowing for this fact, however, there is also the possibility that this plasma mode may be a response to the probe presence, e.g. an effect of sheath-induced oscillations. This does not seem consistent with the measurements since

qualitatively we anticipate that such sheath-related oscillations should appear on the time scale of sheath formation, i.e. the plasma frequency, whereas our measured frequencies were below this limit. With that said, however, we cannot categorically dismiss the possibility that these measured waves are probe-induced as we did not have an independent, non-perturbative mechanism to assess them. As we discuss in the following though, the mode number and dispersion content, if we attempt to correct for the aliasing, are physically consistent with the linear dispersion of the EDI.

To this end, we would expect that the short wavelengths of the EDI mode in this frequency range could not be measured directly with our setup. We thus cannot make a direct comparison or validation against the theoretical description. As an alternative, by using the known EDI dispersion relation with physically-informed assumptions about the local plasma parameters, we can calculate the expected harmonic frequencies of the EDI. Since we are able to measure these unambiguously we can compare the predictions to our measured results. If the numerically solved resonance frequencies closely match our measured values, we could take this as correlative evidence that high frequency oscillations are attributable to the EDI.

As a reminder for the Hall thruster plasma, the dispersion relation for the electron drift instability given by[32, 19]

$$\epsilon^{(1)} = 1 + k^2\lambda_{De}^2 + g\left(\frac{\omega - k_y V_d}{\omega_{ce}}, (k_x^2 + k_y^2)\rho^2, k_z^2\rho^2\right) - \frac{k^2\lambda_{De}^2\omega_{pi}^2}{(\omega - k_x v_{di})^2}, \tag{4.2}$$

where $g(\Omega, X, Y)$ is the Gordeev function defined as

$$g(\Omega, X, Y) = i\Omega \int_0^{+\infty} e^{-X[1-cos(\varphi)]-\frac{1}{2}\varphi^2+i\Omega\varphi} d\varphi. \tag{4.3}$$

ere ω is the oscillation frequency, ω_{ce} is the electron cyclotron frequency, ω_{pi} is the ion plasma frequency, $k = \sqrt{k_x^2 + k_y^2 + k_z^2}$ is the oscillation wavenumber, k_x is the

Table 4.1: Assumed plasma parameters for solution of EDI dispersion

$n_0 \times 10^{17}$ m^{-3}	T_e, eV	ω_{ce}, MHz	v_p, km/s	β, deg	$k_z\lambda_{de}$	V_d, km/s
6 - 12	20 - 40	257	16	20	0.005	$V_{the}/2$

wavevector component traveling in the axial direction, k_y is the component in the $E \times B$ direction, k_z is the component in the radial direction (along magnetic field lines), V_D is the azimuthal electron drift velocity, v_{di} is the ion beam velocity in the axial direction, λ_{De} is the Debye length, and $\rho = V_{the}/\omega_{ce}$ is the electron Larmor radius at thermal velocity $V_{the} = \sqrt{T_e/M_e}$ where T_e is expressed in terms of energy.

We elect to do this comparison between theory and experiment at conditions representative of the acceleration region. This is driven primarily by the theory that this is the region where the linear growth is expected to be highest (i.e. where the Hall drift, the driving source for the instability, is highest). We calculated the theoretical resonance frequencies at this location following the method used by Cavalier et al.[19] to solve the dispersion relation. There are several free plasma parameters in EDI dispersion relation that could affect the calculation of the resonant frequencies, but many can be estimated with reasonable assumptions based on previous Hall thruster measurements[78, 29]. We consider a range of densities and electron temperatures that could manifest in the acceleration region(Table 4.1), but fix all other quantities, except for the electron drift velocity V_d. The dispersion relation is extremely sensitive to the electron drift velocity and we adjusted this parameter until a best fit was achieved at about half the electron thermal speed which is of the order seen in simulations.[66, 9]. Finally, as we were unable to measure the radial wavenumber at high frequencies, for the theoretical dispersion we set the radial wavenumber (k_z) low enough to maintain distinct resonances. We used a value of $k_z\lambda_{De} = 0.005$, but the exact value was not important for this analysis as long as the resonances were still intact. This due to the real frequency at the resonances remaining constant with radial wavenumber.

The predicted EDI resonances from the analytical dispersion along with the measured resonant frequencies are presented in Figure 4.7. The error bars on the experimental data correspond to the full width half max of each resonance peak in the power spectrum(see Figure. 4.4), while the error bars for the numerical solution represent the range of possible results for the values listed in Table. 4.1. The markers for the numerical solution show the overall best fit for $n_0 = 6.5 \times 10^{17}$ m^{-1} and $T_e = 25$ eV. There is close agreement between experimental and numerical values across the 8 measured resonances with the numerical solution slightly over-predicting the frequency for the first few modes and slightly under-predicting at the highest modes. With that said, the close agreement across 8 mode numbers for a wide range of densities and temperatures and with an electron drift velocity closely matching values from simulations provides strong correlational evidence that the measured megahertz oscillations are EDI cyclotron resonances.

Despite this agreement between theory and experiment in the acceleration zone, there is one notable feature in the measured modes not anticipated by the linear theory: the invariance of the frequency values of the resonances. Indeed, the background plasma properties (most significantly the electron cyclotron frequency) vary as a function of spatial position, which would suggest from Eqn. 4.2 that in turn the resonant frequencies also should vary. This is not reflected in our measurements where the resonant frequencies remain relatively constant. While we do not have sufficient data to conclusively identify why this occurs—in particular we cannot see if the wavelength of the oscillation changes through the plume instead—there is a possible explanation from the measurements and underlying theory. Linear saturation should occur quickly in the acceleration region, and it is possible that further downstream, where the linear growth rate is significantly diminished by the lower electric field and $E \times B$ drift velocity, the wave no longer has the energy to grow at different resonant frequencies. This assumes that the original resonant frequencies still satisfy the real

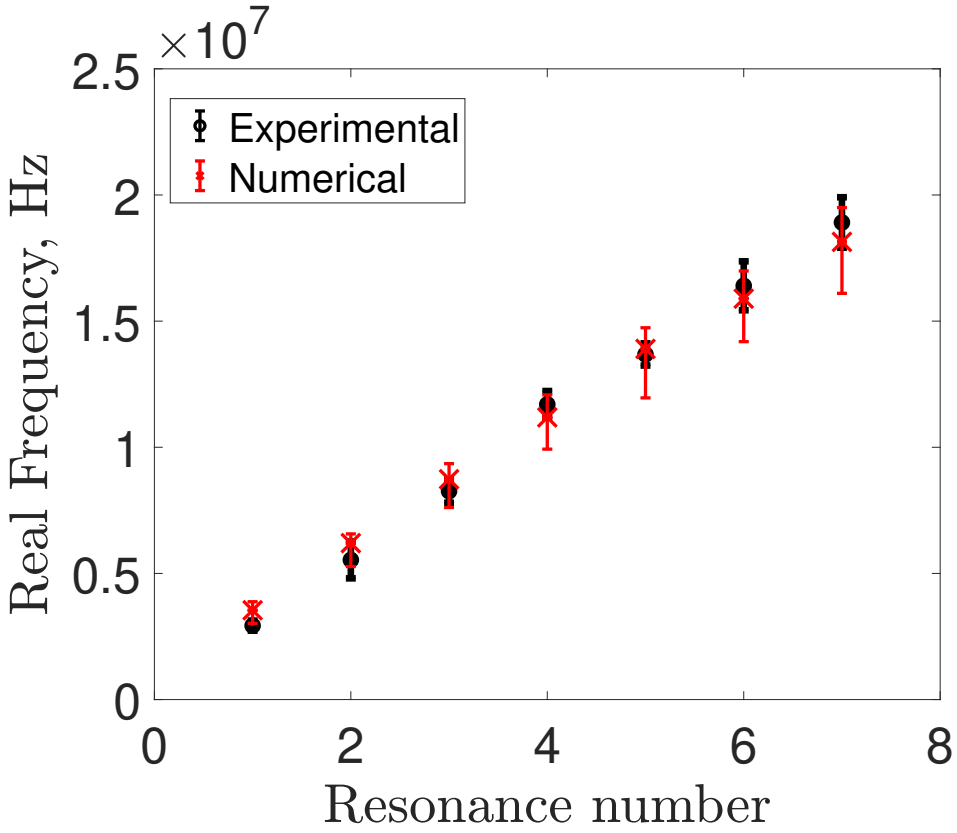

Figure 4.7: Comparison between experimentally measured resonance frequencies and numerical solutions for values typical of the acceleration zone (Table. 4.1)

component of the dispersion relation in the far-field. While our measurements are insufficient to determine the dispersion relation at every point in the plume we note that parameters typical of the far-field region ($T_e = 3$ eV, $n_0 = 1 \times 10^{17}$ m^{-3}, $v_p = 20$ km/s, $V_D = 50$ km/s, and $\omega_{ce} = 209$ MHz) yield a dispersion relation with a significantly reduced growth rate (Fig.4.8a) and a real frequency very close to the original resonances (Fig.4.8b).

With these caveats in mind, we ultimately conclude that at least correlationally, the measured modes in the acceleration zone appear to be EDI. Though, they exist with fundamentally different properties than the acoustic like EDI oscillations measured downstream. Indeed, the measured resonant-like waves actually seem to be more in line with the predictions of linear growth. This result physically is intuitive

given that this region, i.e. the region of maximum Hall drift, is likely where the modes originate in the thruster.

4.4.2 Quantifying transition from acceleration zone to downstream region

The previous two sections have shown that the observed waves appear to be consistent with the EDI either in both the resonant and the acoustic-like limit depending on where the measurement is made. The structure exhibits discrete wavelengths in the upstream region and broadband oscillations downstream. The former, as discussed above is consistent with the predictions of linear dispersion theory: the EDI power spectrum should be dominated by discrete frequencies corresponding to cyclotron resonances of the EDI. The latter state with its broadband character, however, is not intuitive and does not directly follow from linear theory. Indeed, even allowing for the case of finite k_z where the EDI becomes acoustic like resonances, the linear growth still has a maximum coincident with the ion plasma frequency. We do not see such a peak in the measured dispersion. With this in mind, we next turn to the question as to if and how the EDI in the acceleration zone is connected to this downstream state.

To this end, the hypothesis we propose here is informed by the work of Janhunen et al[55, 56]. The downstream state is the nonlinear result of an inverse energy cascade from cyclotron resonances of the EDI toward the lowest mode numbers and then into a long wavelength oscillation much larger than the fundamental resonance wavelength. Physically, in this process, two high frequency resonances "beat" against one another and couple energy between the resonances and the beat frequency of the two waves. This process effectively transfers energy to lower frequencies and thus larger lengthscales. For example, the m = 3 and m = 5 modes would beat together and transfer energy to the m = 2 mode. This wave-wave coupling process ultimately gives rise to a power law like decay in frequency spectrum. This hypothesis is supported by the many similarities between our measured power spectra as function

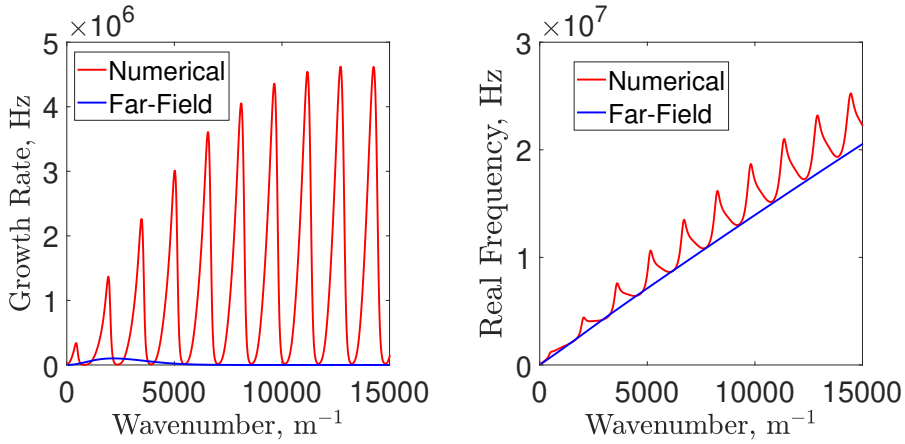

Figure 4.8: a) Growth rate and b) frequency for analytical solutions of the EDI dispersion relation. The red curves are the best-fit solution for the parameters typical of the acceleration zone ($n_0 = 6.5 \times 10^{17}$ m^{-1} and $T_e = 25$ eV) while the blue curves use values typical of the far-field plume: $T_e = 3$ eV, $n_0 = 1 \times 10^{17}$ m^{-3}, $v_p = 20$ km/s, $V_D = 50$ km/s, and $W_{ce} = 2 \times 10^8$ Hz, otherwise using the same parameters from Table 4.1.

of position (Figure 4.3) and the numerical results of Janhunen (Figure 14 in reference [56]) where the authors show the power spectrum as function of wavenumber vs time. Both show clear resonances at high wavenumber/frequency that gradually decay verses time/position as a low wavenumber/frequency oscillation appears. Since the simulation of Janhunen did not model the axial direction we interpret the temporal evolution of the EDI seen in 2D as equivalent to the spatial changes seen in our experiment as the instability evolves while being carried downstream by the beam plasma. This is supported by both the characteristic transient time of the beam plasma traveling from the acceleration region to where we observe the broadband low frequency oscillations and the time scale of the energy cascade seen in the simulation being on the order of μs.

We can expand on this interpretation quantitatively by examining the spatial evolution of the normalized wave-energy density, (W/n_0T_e). For electrostatic waves,

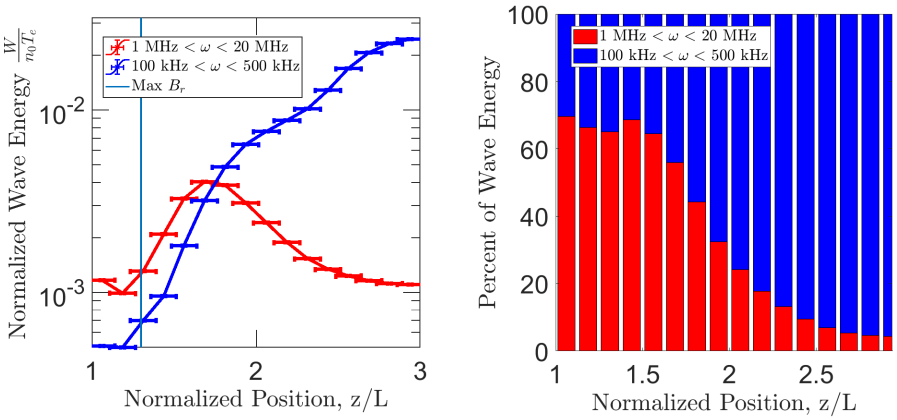

(a) (b)

Figure 4.9: The normalized wave energy density (a) and relative strength of modes(b) at various points in the plume of the H9 along channel centerline are shown relative to the location of peak magnetic field, denoted by the light blue vertical bar at z/L = 1.3. Frequencies between 1 and 20 MHz are from the resonances and frequencies between 100 and 500 kHz are due to the broadband acoustic oscillations.

this can be approximated as[87]

$$\frac{W}{n_0 T_e} = \sum_{\omega} \left(\frac{\phi(\omega)}{T_e} \right)^2, \tag{4.4}$$

where the summation is taken over the frequency domain corresponding to the wave of interest and $\phi(\omega)$ is the amplitude of plasma potential fluctuations. Physically, this represents the relative magnitude of energy in the oscillation range compared to the thermal background and is a measure of the relative strength of the oscillations. In order to relate this quantity to the parameters we measured, we note that the plasma density fluctuations for the electrostatic EDI waves can be related approximately as potential fluctuations by the Boltzmann response, $\tilde{n}/\overline{n} \approx \tilde{\phi}/T_e$. This allows us to write the normalized wave energy density exclusively as a function of our measured property $\tilde{n}/\overline{n}$ and eliminates the requirement of concurrent temperature and density measurements.

Armed with this definition, we show in Fig. 4.9a the normalized wave energy as

a function of position along channel centerline for both classes of oscillations that we have documented: the low frequency broadband (100-500kHz) and the resonances (1-20MHz). The first notable feature is that the wave energy density is a finite fraction (0.002) of the thermal energy density within the acceleration region. This suggests that the mode may have reached a saturated state, i.e. the wave growth is limited. This type of saturation is not unexpected in this region which is characterized by the strongest $E \times B$ drift. Indeed, reduced dimension numerical simulations have shown that when the electron drift is strong (i.e. a substantial fraction of the Mach speed), wave growth can be capped by effects such as ion wave trapping [64]. Downstream of the acceleration zone, we see that the energy in the spectrum undergoes a change coinciding with growth of the low frequency turbulence. In particular, upstream of the peak magnetic field (z/L = 1.3), where we anticipate the EDI will first onset due to the strong E $\times$ B drift, we see that the resonances are the primary source of wave energy. Immediately downstream of the peak magnetic field, both the low and high frequency modes grow together in strength until the high frequency waves reach a maximum at about z/L = 1.6. After this location two transitions occur. First, the low frequency broadband oscillations overtake the cyclotron resonances in terms of relative strength. This is indicated in Fig. 4.9b where the relative amplitude of the two oscillations are plotted with position. Second, as discussed in Sec. IV. this location is where the linear dispersion becomes visible in the Beall plots. After this point, the resonances decay in strength while the broadband oscillations continue to grow until z/L = 3. Although, as shown in Fig. 4.4 the first and third resonances are still visible downstream. These two figures thus show quantitatively the evident interplay in energy between the oscillations described in our hypothesis.

With that said, one interesting caveat to our interpretation is that we see that the resonant structure persists (Fig. 4.4) even when the broadband oscillations dominate. On the other hand, in previous experimental work, Tsikata et al did not record any

resonances even though they were measuring in the same frequency range. The work by Janhunen may offer a resolution. Our probes measure fluctuations in ion density while Thomson scattering instead measures electron fluctuations. According to this previous numerical work, the nonlinear cascade towards long wavelength is significantly stronger for electrons compared to the ions. While the ion oscillations retained their resonant modes at the end of the simulation, in the electrons the presence of all but the first mode had disappeared. Therefore, Thomson scattering measurements downstream of the acceleration region would lead to different observations than electrostatic probing, potentially without resonances.

From a practical perspective, if this inverse cascade is a real mechanism, our results have implications for the understanding and approach to modeling of the micro-turbulence that contributes to anomalous cross-field electron transport in Hall effect thrusters. Indeed, as the growth and saturation of the EDI appears to be a highly nonlinear process, it can be inferred that its interaction with the electrons (and thus its drag-inducing effect) similarly must be nonlinear. Any model capable of predicting the transport in a real thruster geometry must consider this effect, either modeling it explicitly with a full kinetic approach or developing closures for fluid approximations that reflect the inverse energy cascade across lengthscales. In particular, it is prudent that all future kinetic simulations must use grids that are sufficiently large to resolve our observed long wavelength oscillations.

In summary, the measured results correlationally support the hypothesis we have proposed. Within the acceleration region, the EDI develops with a linear growth, which results in discrete resonances from the EDI dispersion relation. As the instability propagates downstream, its properties are dominated by nonlinear effects that ultimately lead to broadband long wavelength oscillations. Thus, in addition to showing in the previous section that EDI likely exists in the acceleration zone, we have a plausible explanation for why and how the shape of the EDI power spectrum

is causally connected to downstream measurements.

4.5 Conclusion

In this Chapter we have presented the results of an investigation of the electron drift instability in a Hall thruster's near field plume and acceleration region. In light of previous experimental work that has been performed in studying this mode, the driving considerations for our study were trying to determine if the EDI actually exists in the thruster acceleration zone and how this EDI evolves as a function of position in the thruster. We have found that in the acceleration region, the EDI does exist and is characterized by cyclotron resonances of the EDI in the 1-20 MHz domain. This is consistent with the predictions from linear growth theory. In the downstream region, on the other hand, the power spectrum exhibits a fundamentally different character. The resonances still persist but the dominant feature is that the power spectrum is characterized by a broadband turbulent shape exhibiting an power law-like decay. While we have shown that both types of waves can be consistent with EDI waves–one in the discrete cyclotron resonance region and one in the acoustic limit–we have also sought to propose an explanation for how the two might be linked. To this end, we have proposed an explanation informed by previous numerical work[55, 56], which suggests that the downstream measurements are an evolved nonlinear state of the EDI which onsets in the upstream, acceleration zone. The resonances develop following linear growth in the acceleration zone and could undergo an inverse energy cascade in the downstream region that gives rise to the linear acoustic waves. We have plotted the evolution of the energy associated with the resonances and broadband turbulence to show correlationally that this type of interplay of energy across lengthscales may in fact occur. We theorize that this cascade, which is enhanced for electrons compared to ions, is responsible for the absence of resonances observed in Thomson scattering measurements reported in previous studies[101].

In the context of the central question for Hall thrusters about the role of instabilities in driving cross-field transport, this work ultimately offers new insight into the role of the EDI in these thrusters. The observation of its transition from linear growth to a turbulent state suggests that the growth of this mode and interaction with the plasma are ultimately a nuanced and complex process. Indeed, these nonlinear effects ultimately will need to be considered self-consistently for efforts to relate the EDI to the steady-state electron dynamics in these systems. In the next Chapter will apply the bispectral analysis techniques discussed in Chapter III to investigate these non-linear features and ultimate determine the cross-field transport induced by the EDI.

CHAPTER V

Determination of Instability Induced Cross-field Transport

5.1 Introduction

From the results of Chapter IV, it is clear that the electron drift instability is present in Hall thruster plumes, but there are several important questions that remain. Notably our results pointed toward the role of non-linear effects in the development the EDI. While there are a wide range of theories for these aspects of the EDI dynamics [32, 66, 55, 56, 15, 97], there has yet to be a direct experimental measurement of the linear growth and nonlinear wave coupling processes that govern the EDI spectrum. This lack of experimental data speaks to a broader problem commonly encountered in measuring wave dynamics in low temperature plasmas [58]: established methods based on length-scale bispectral analysis[82, 86], developed for higher energy density plasmas, do not translate well to space-based and low temperature systems. In light of these obstacles and the importance of understanding the processes that shape the EDI growth spectra, we present in this Chapter the results of an experimental utilizing a frequency-based bispectral analysis technique to make direct experimental measurements of the linear growth and nonlinear energy transfer of the EDI in a laboratory Hall effect discharge. Building on these results, we then

will apply this new data to directly calculate the wave-driven cross-field transport and answer the primary question of this thesis: Is the electron drift instability responsible for anomalous transport in Hall thrusters.

5.2 Determination of EDI induced cross-field electron transport

As highlighted throughout this work, the cross-field electron transport in Hall effect thrusters has yet to properly attributed to any specific mechanism, though there are many strong theories. While most electrons are trapped in an azimuthal Hall effect drift, classically some electron current parallel to the electric field, i.e in the cross-field direction, can result from particle-particle collisions, experiments have shown that the actual cross-field current is orders of magnitude higher [54, 7, 74].Practically, this lack of understanding has impeded the development of fully predictive Hall thruster models [7, 58]. In light of this limitation, several different theories have been proposed to date to explain the transport. These include processes related to Bohm diffusion as well as near-wall effects [74, 11, 4, 41, 73, 33]. There is a growing consensus, however, that the transport may largely be attributed to the formation of small-scale instabilities [10]. Recent kinetic simulations [63, 55, 56, 81, 9, 52, 60] and analytical models [32, 19, 64] have suggested that the high $E \times B$ velocity of the electrons results in the growth of the so-called electron drift instability (EDI). This EDI grows at the expense of electron momentum, resulting in an effective drag on this species. This force on the electrons, when combined with the radial magnetic field, promotes a cross-field drift. Indeed, numerical simulations have indicated that this effect may be sufficient to explain the anomalous transport. In parallel, experimental studies have confirmed that the EDI exists in the thruster plasma[101, 100, 12, 15]. However, despite this experimental evidence of the EDI, it has yet to be demonstrated if the

instability as measured in experiment is sufficient to explain the transport. The role of the EDI in real systems thus remains an open question.

In an effort to address this question, we employed in a previous work experimental measurements of the EDI wave amplitude combined with quasi-linear theory in an attempt to relate the EDI to an effective transport coefficient. We ultimately found, however, that we were not able to recreate the experimentally-measured transport[13]. We subsequently hypothesized this discrepancy might be attributed to an oversimplification in our approximation of the growth rate, i.e. the rate at which the EDI extracts energy from the Hall drift. Indeed, while we had employed the theoretical form of the growth rate based on a linear expansion of the dielectric response in a Maxwellian plasma, recent simulations have shown the growth and saturation of the EDI is highly non-linear in nature[55, 56, 97]. These nonlinear features in turn can lead to distortion of the electron velocity distribution function (EVDF) and cross-lengthscale coupling–both effects that can lower the magnitude of the growth rate and subsequent transport [32, 63, 64]. In light of these previous modeling results and our direct experimental observation that the EDI growth exhibits non-linear features (Chapter IV), we thus suspected we would need to amend our estimates for the growth rate in our calculations for EDI-induced transport. In this section will detail an experimental effort to directly measure the linear growth rates and non-linear energy exchange in the Hall thruster acceleration zone, the region of maximum axial electric field and ion acceleration.

5.2.1 Relating anomalous collision frequency to EDI properties

Figure 5.1 shows a representative geometry of a Hall effect thruster. This cylindrical crossed-field device features a radial magnetic field, $\vec{B} = B_r\hat{z}$, perpendicular to an applied axial electric field, $\vec{E} = E_{x(0)}\hat{x}$. This field configuration induces a $E \times B$ Hall drift of the electrons in the azimuthal direction, $\hat{y}$. Due to particle-particle colli-

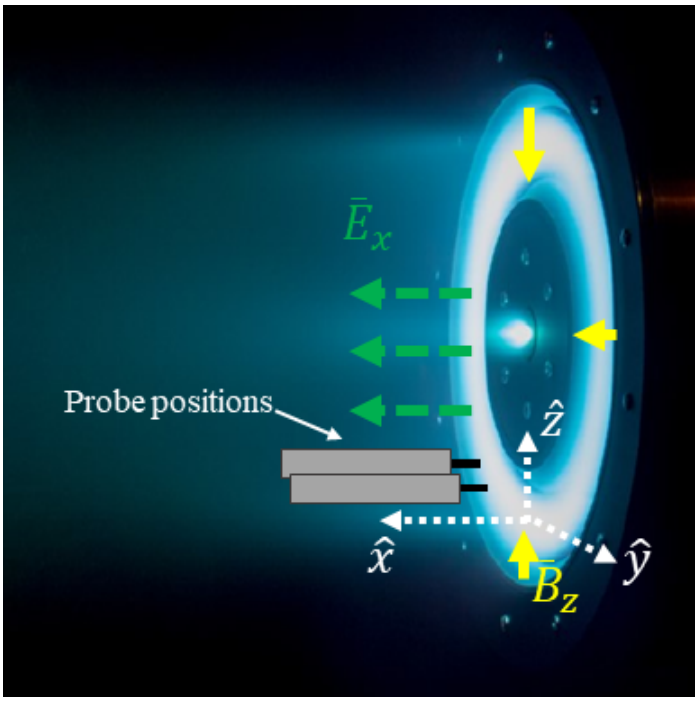

Figure 5.1: H9 Hall thruster shown with axial electric field ($\bar{E}$), radial magnetic field ($\bar{B}$), and probes placed in the $E \times B$ direction.

sions, electrons should exhibit some small mobility across magnetic field lines in the direction of the electric field. However, as discussed in the preceding, the observed electron transport levels are orders of magnitude larger than can be explained by collisions.

The cross-field transport of electrons can modeled starting with a drift-diffusion equation for electrons where we neglect electron inertia:

$$0 = -\frac{q^2}{m_e} n_e(\vec{E} + \vec{v}_e \times \vec{B}) - \frac{q}{m_e}\nabla(p_e) + \vec{j}_e \nu_c \tag{5.1}$$

Here m_e is electron mass, n_e is electron density, $\vec{j}_e$ is the electron current density, $\vec{E}$ and $\vec{B}$ are local electric and magnetic fields, $p_e = q n_e T_e$ is electron pressure where T_e is expressed in units of energy, ν_c is the classical electron collision frequency, and q is fundamental charge. The first term is the Lorentz force, the second is the pressure force, and the third is the effective drag due to particle collisions. We represent the electrostatic EDI waves as rapid perturbations in density, $n_e = \delta n_e + n_{e(0)}$ and

electric field, $\vec{E} = \delta\vec{E} + \vec{E}_0$, where δx terms denote the oscillating component against a background value x_0. We then phase average Eq. 5.1 over the time scale of the oscillation to yield

$$0 = \frac{q^2}{m_e}\left[\langle \delta n_e \delta\vec{E}\rangle + n_{e(0)}\vec{E}_0 + n_{e(0)}\vec{v}_e \times \vec{B}\right] - \frac{q}{m_e}\nabla(p_e) - \vec{j}_e\nu_c \tag{5.2}$$

In this equation, phase averaging has eliminated the oscillating components of n_e and $\vec{E}$ except for the term containing their product $\langle \delta n_e \delta\vec{E}\rangle$. If the density and electric field oscillations are in phase this term will be non-zero.

We next assume the steady state electric field is only is the axial direction ($\vec{E}_0 = E_{x(0)}\hat{x}$), the oscillating electric field induced by the EDI is in the azimuthal direction ($\delta\vec{E} = \delta E_y \hat{y}$), and the radial magnetic field strength is sufficiently large such that the electron cyclotron frequency ($\omega_{ce} = qB_r/m_e$)is much larger than the classical particle collision frequency to arrive at an equation for axial electron current density

$$j_{e(x)} = \frac{q^2 n_{e(0)}}{m_e \omega_{ce}^2}\left(E_{0(x)} + \frac{\nabla_x(n_{e(0)}T_e)}{q n_{e(0}}\right)\nu_e, \tag{5.3}$$

where we have defined a total electron collision frequency, $\nu_e = \nu_c + \nu_{AN}$. The latter parameter represents an effective anomalous collision frequency that arises from the action of the waves:

$$\nu_{AN} = -\omega_{ce}\frac{\langle \delta n_e \delta E_y\rangle}{n_{e(0)}E_{x(0)} + \nabla_x(n_{e(0)}T_e)}. \tag{5.4}$$

This definition underscores the fact that from a fluid, phase-averaged perspective, the propagation of the EDI can be represented as an enhanced transport coefficient for the electrons. Similarly, per the definition, we see that as the relative fluctuations in electric field and density from the waves increase, the wave-induced cross-field transport on the electrons will be higher. Physically, this scaling stems from the fact

that the growth of the EDI can be interpreted as an effective drag on the azimuthal drift in the plasma, which in turn promotes cross-field current.

In practice, it is prohibitively difficult in our plasma to measure fluctuating density and electric field simultaneously for the purpose of evaluating Eq. 5.4 directly. Instead, we follow a linearized theory for wave propagation where we assume the EDI oscillations can be represented as a summation over a spectrum:

$$\delta\vec{E} = -i\sum_{\vec{k}} \vec{k}\phi(\vec{k},\omega), \tag{5.5}$$

where $\phi(\vec{k},\omega)$ denotes the propagating oscillations in plasma potential associated with the wavenumber (k) and frequency (ω) of the electrostatic wave. We in turn invoke the eikonal approximation to write

$$\phi(\vec{k},\omega) = \hat{\phi}(\vec{k},\omega)\exp\left[i\left(\vec{k}\cdot\vec{r}-\omega t\right)\right], \tag{5.6}$$

where $\hat{\phi}(\vec{k},\omega)$ denotes the complex amplitude of the potential oscillation.

Following the technique of Davidson and Krall[31], we then can show from a linearization of the dielectric function of the plasma that averaging over the wave phase yields:

$$\langle\delta n_e \delta E_k\rangle = \sum_k \gamma_{e(k)} k_y k^2 \frac{\partial\epsilon_r^{(1)}(\vec{k},\omega)}{\partial\omega}|\hat{\phi}(\vec{k},\omega)|^2. \tag{5.7}$$

Here k_y denotes the component of the wavevector of the k^{th} mode in the Hall direction, $\epsilon_r^{(1)}(\vec{k},\omega)$ is the real component of the dielectric response of the wave to the first order, ω is the real component of the frequency, and we have performed the summation over a spectrum of oscillations associated with the EDI. We also have introduced the parameter $\gamma_{e(k)} = -\epsilon_{i(e)}^{(1)}(\vec{k},\omega)/(\frac{\partial\epsilon_r^{(1)}(\vec{k},\omega)}{\partial\omega})$, which is the linear growth rate of the

wave due to the electron contribution to the imaginary component, $\epsilon^{(1)}_{i(e)}(\vec{k},\omega)$, of the dielectric function to the first order. Physically, this latter parameter represents the rate at which electrons extract energy from the Hall drift.

As an additional simplification, we make the substitution $\phi(\vec{k},\omega)/T_e = \delta n_{i(k)}/n_{i(0)}$where T_e is the electron temperature in electron volts and $\delta n_{i(k)}$ is the variation in ion density associated with the k^{th} element of this spectrum of the EDI. This relationship is appropriate for the EDI dispersion [19] for cold ions, $T_i \ll T_e$, where T_i is ion temperature. Invoking this simplification, we can express Eq. 5.4 as

$$\nu_{AN} = \frac{\omega_{ce}}{E_{x(0)} + \frac{\nabla_x(n_{e(0)}T_e)}{n_{e(0)}}} T_e \lambda_{De}^2 \sum_k \gamma_{e(f)} k_{y(f)} k_f^2 \frac{\partial \epsilon_r^{(1)}(\vec{k},\omega)}{\partial \omega_r} \left| \frac{\delta n_{i(k)}}{n_{i(0)}} \right|^2, \quad (5.8)$$

where λ_{De} denotes the Debye length. This result shows that as the relative fluctuation in ion density increases (an indication of stronger waves), the effective drag on the electrons increases. Similarly, with a higher electron growth rate, i.e. rate at which the waves extract momentum from the Hall drift, the transport coefficient also increases.

As a final simplification, we note that while Eqn. 5.8 is formulated in terms of a summation over wavenumber, in practice, our experimental measurements are time-based Fourier transforms of density fluctuations. To translate this result into a form that is expermentally tractable, we assume that the relationship between frequency and wavenumber is approximately one-to-one such that the k^{th} wavenumber maps to a unique real frequency, $f = \omega/2\pi$. We therefore can make the substitutions $\delta n_{i(k)} \rightarrow \delta n_{i(f)}$ and $\gamma_{e(k)} \rightarrow \gamma_{e(f)}$ to find

$$\nu_{AN} = \frac{\omega_{ce}}{E_{x(0)} + \frac{\nabla_x(n_{e(0)}T_e)}{n_{e(0)}}} T_e \lambda_{De}^2 \sum_f \gamma_{e(f)} k_{y(f)} k_f^2 \frac{\partial \epsilon_r^{(1)}(\vec{k},\omega)}{\partial \omega} \left| \frac{\delta n_{i(f)}}{n_{i(0)}} \right|^2, . \quad (5.9)$$

This result ultimately is the expression we experimentally evaluate in order to relate

the EDI properties to cross-field transport in the Hall thruster.

5.2.2 Theoretical dispersion and growth of the EDI

In order to estimate the transport coefficient experimentally from Eq. 5.9, we require measurements of both the the dispersion and growth of the EDI. As a first order approach to determine this properties, we consider the theoretical form of the EDI dispersion that stems from a linearization of the Vlasov equation subject to the assumption of cold ions and Maxwellian electrons [32, 19]:

$$\epsilon^{(1)}(\vec{k},\omega) = 1 + k^2\lambda_{De}^2 + g\left(\frac{\omega - k_y V_{E\times B}}{\omega_{ce}}, (k_x^2+k_y^2)\rho^2, k_z^2\rho^2\right) - \frac{k^2\lambda_{De}^2\omega_{pi}^2}{(\omega - k_x v_{i(o)})} = 0 \quad (5.10)$$

where g(Ω, X, Y) is the Gordeev function, defined as

$$g(\Omega, X, Y) = i\Omega \int_0^{+\infty} e^{-X[1-cos(\varphi)]-\frac{1}{2}\varphi^2+i\Omega\varphi} d\varphi. \quad (5.11)$$

Here ω_{pi} is the ion plasma frequency, $k = \sqrt{k_x^2+k_y^2+k_z^2}$ is the oscillation wavenumber, $v_{i(0)}$ is the ion beam velocity in the axial direction, $V_{E\times B}$ is the azimuthal Hall drift of the electrons, and $\rho = V_{the}/\omega_{ce}$ is the electron Larmor radius at thermal velocity, $V_{the} = \sqrt{qT_e/m_e}$. We show in Fig. 5.2 example solutions to this dispersion relation, adapted from Ref. [19], for different assumed radial wavenumbers. In Fig. 5.10(a), we see the frequency is approximately linear but punctuated by periodic peaks. The first of these peaks corresponds to the so-called modified two-stream instability(MTSI)[55, 56] while the subsequent peaks are harmonics of the EDI related to the electron cyclotron resonance frequency by: $k_y = n\omega_{ce}/V_{E\times B}$, where n in the harmonic mode number. Fig. 5.10(b) shows the linear growth also exhibits peaks at the wavenumbers of the MTSI and cyclotron harmonics. This physically stems

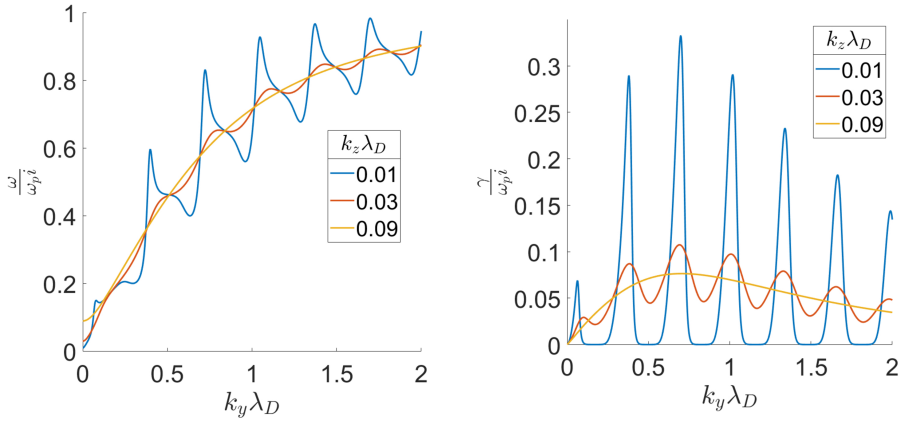

(a) (b)

Figure 5.2: Solutions of the EDI dispersion relation, adapted from Cavalier et al[19] with different radial wave components (k_z). Frequency (a) and growth rate (b) are normalized by the ion plasma frequency (ω_{pi}) and wavenumber is normalized by the Debye length(λ_{De}).

from the fact that these modes have the highest degree of coupling with the Hall drift at these resonances. As the the radial component of the wavenumber decreases, the peaks in both the real frequency and growth rate reduce in amplitude and ultimately disappear. In this limit, the EDI exhibits an ion-acoustic like dispersion [19].

Previous experimental work has shown that at high frequency (above 2 MHZ) and in regions downstream of the acceleration zone, the real components of the wave dispersion in a Hall thruster matches the EDI in the acoustic limit [101]. We also demonstrated in recent experimental work that this real part of this dispersion relation is consistent with measurements of the wave propagation in the thruster acceleration zone [15]. In light of these previous findings, we employ in this work the theoretical form of the real component of the dielectric response in the acoustic limit to evaluate Eq. 5.9. Given this dispersion has a one-to-one relationship between frequency and wavenumber, we similarly can justify the conversion we made in the preceding section.

On the other hand, with respect to the growth rate, previous numerical studies and our experimental work have shown that the linearized theory does not accurately

reflect the evolution of the EDI [66]. This disparity likely stems from nonlinear effects impacting the wave growth and the kinetic velocity distribution of electrons. With this in mind, while we still use the linear theory as a point of comparison for estimating the transport in this work, we discuss in the following section a methodology we developed to directly measure this growth rate.

5.2.3 Modelling non-linear processes of the EDI

As covered in Chapter III, our approach to measuring non-linear EDI wave dynamics is based on formulating a governing equation for the evolution of EDI wave amplitudes. We then use experimental measurements of these amplitudes and a bispectral analysis method adapted from the works of Ritz [82] and Kim [86] to infer the parameters in the wave equation that represent linear and nonlinear growth. While the full derivation of this method from first principles is provided in Chapter III we provide an abbreviated review here for clarity. Figure 5.1 shows the geometry of the Hall effect discharge we investigated with this approach. This device has azimuthal symmetry with an axial electric field and radial magnetic field. The resulting azimuthal $E \times B$ drift is the energy source for driving the EDI unstable. For our analysis, we adopt the local Cartesian coordinate system shown in Fig. 5.1. Where two electrostatic probes are separated in the azimuthal $\hat{y}$ direction by distance, Δy. These probes simultaneously measure the time-based Fourier spectrum at each location to yield $X_f = \hat{\phi}_f(y)$ and $Y_f = \hat{\phi}_f(y + \Delta y)$. Based on these two measurement locations, we generate an equation describing the linear and non-linear evolution of the waves

$$Y_f = L_f X_f + \sum_{f=f_1+f_2} Q_f^{1,2} X_{f_1} X_{f_2}, \tag{5.12}$$

where we have defined linear and nonlinear transfer functions:

$$L_f = \left(\left[\gamma_{f(y)}/v_{g(y)} + ik_y\right]\Delta y + 1\right) \tag{5.13}$$

$$Q_f^{1,2} = (V_{1,2}^Q/v_{g(y)})\Delta y \tag{5.14}$$

. Here we have introduced the azimuthal linear growth rate:

$$\gamma_{f(y)} = \gamma_f - \mathrm{Re}\left(X_f^{-1}\left[v_{g(x)}\partial_x X_f + v_{g(z)}\partial_z X_f\right)\right]) \tag{5.15}$$

. This reflects the fact that the observed change in the amplitude of each mode in $\hat{y}$ is a projection of the total growth rate from three dimensions. Finally, we multiply Eq. 5.12 by the complex conjugate quantities, X_f^* and $X_{f_1}^* X_{f_2}^*$ respectively, to yield

$$\begin{aligned} Y_f X_f^* &= L_f X_f X_f^* + \sum_{f=f_1+f_2} Q_f^{1,2} X_{f_1} X_{f_2} X_f^* \\ Y_f X_{f_1}^* X_{f_2}^* &= L_f X_f X_{f_1}^* X_{f_2}^* + \sum_{f=f_1+f_2} Q_f^{1,2} X_{f_1} X_{f_2} X_{f_1}^* X_{f_2}^*. \end{aligned} \tag{5.16}$$

The first equation is the complex form of a discretized wave energy equation. The second represents the third moment of the wave-dynamics, also known as the cross-bispectrum.

With experimental measurements of the moments in Eq. 5.16, the system can be solved for the linear and nonlinear transfer functions. In turn, from these values, we can infer key properties of the wave dynamics including the azimuthal growth rate, $\gamma_{f(y)} = (\mathrm{Re}[L_f] - 1)(v_{g(y)}/\Delta y)$ and the nonlinear power transfer function:

$$T_f = (v_{g(y)}/\Delta y)\mathrm{Re}\left[\sum_{f=f_1+f_2} Q_f^{1,2} X_{f_1} X_{f_2} X_f^*\right]. \tag{5.17}$$

This last term physically represents the energy flux transferred to the mode of fre-

quency f by nonlinear coupling from other modes in the spectrum.

We solve the governing equations following the algorithmic approach developed by Ritz [82] and later modified by Kim [86]. This analysis method has two key requirements. The first is ensemble averaging the various moments in Eq. 5.16 over multiple measurements[85]. This reduces the stochastic noise such that the higher order moments can be accurately resolved. The second requirement is that the ensemble averaged power spectra, $P_f = \langle X_f X_f^* \rangle \approx \langle Y_f Y_f^* \rangle$, are stationary between the two probe locations[86]. As discussed in Ref. [86], this technique is susceptible to several inaccuracies when applied to noisy experimental data. The Kim method improves on the Ritz technique by separating the measured spectral content into a summation of ideal terms driven solely by Equation 5.12 and non-ideal terms that come from both systematic errors and plasma processes that do not follow Equation 5.12:

$$X_f = \beta_f + X_f^{ni}, Y_f = \alpha_f + Y_f^{ni}. \tag{5.18}$$

Here β and α are the ideal terms and X^{ni} and Y^{ni} are the non-ideal terms. With the introduction of the non-ideal terms, an additional equation is needed for closure of the system of equations. Kim solved this closure problem by invoking a hypothesis of local stationarity: $\left\langle \alpha_f \alpha_f^* \right\rangle = \left\langle \beta_f \beta_f^* \right\rangle$. This is justified in our experiment by the azimuthal symmetry of the Hall thruster plasma. It was this Kim technique that we ultimately use to determined L_f and then $\gamma_{f(y)}$.

As a last step before we can leverage experimental data to solve the governing equations for key terms like L_f and T_f, we need an estimate of the group velocity of the waves. While in principle we could measure this group velocity directly from experimental measurements of the dispersion, $\omega(k_y)$, spatial aliasing from the probe spacing precluded a direct measurement of the wavenumbers of interest. We discussed this aliasing limitation at length in Chapter III and Ref. [15]. Ultimately, we were able

to conclude through an analysis of the resonant peaks in the power spectra that the dispersion of the oscillations in the test article we used for this study (Fig. 5.1)follows the real component of the theoretical EDI dielectric response [37, 40, 19]:

$$\epsilon^{(1)} = 1 + k^2\lambda_{De}^2 + g(\Omega, X, Y) - \frac{k^2\lambda_{De}^2\omega_{pi}^2}{(\omega - k_x v_p)^2}, \tag{5.19}$$

where g(Ω, X, Y) is the Gordeev function, $\Omega = (\omega - k_y V_d)/\omega_{ce}$, $X = (k_x^2 + k_y^2)\rho^2$, and $Y = k_z^2\rho^2$. Here V_D denotes the azimuthal electron drift, ω_{ce} is the electron cyclotron frequency, ω_{pi} is the ion plasma frequency,v_p is the ion beam velocity in the axial direction, λ_{De} is the Debye length, and $\rho = V_{the}/\omega_{ce}$ is the electron Larmor radius at thermal velocity $V_{the} = \sqrt{T_e/M_e}$ where T_e is expressed in terms of energy. To evaluate Eq. 5.10, we employed plasma parameters from previous studies of the test article we used for this study: $n_0 = 8 \times 10^{17} m^{-3}$, $\omega_{ce} = 53$ GHz, $V_D = 526$ km/s, $v_p = 14$ km/s, and $T_e = 15$ eV (see Chapter IV). Furthermore, we have assumed an axial wavenumber number of $k_x = k_y \sin(15^o)$ based on estimates of the wave propagation angle[101, 15] and a radial wavenumber of $k_z\lambda_{De} = 0.03$, where λ_{De} is the Debye length. This corresponds to a wavelength on the order of the channel width [89, 64, 95].

Fig. 5.3a) shows the dispersion inferred from the solution of Eq. 5.10 using these experimental measurements of background properties. The result is approximately linear with slight undulations at the cyclotron resonances: $k_y = n\omega_{ce}/V_d$, where n is the harmonic number. At wavenumbers below the first cyclotron resonance ($f <$ 2 MHz), the dispersion transitions to the so-called modified two-stream instability (MTSI) [55, 56]. We ultimately used the dispersion shown in Fig. 5.3a) to infer the group velocity in the azimuthal direction.

5.3 Measurement of non-linear dynamics and linear growth rate

We now turn to experimentally assessing the non-linear wave properties of the EDI. For our investigation, we employed the H9, a 9-kW class Hall effect thruster (Fig. 5.1) with approximately 30 cm diameter and 15 cm depth. We operated this system at a discharge voltage of 300 V and discharge current of 15 A on xenon gas and performed our experiments in a 6 m $\times$ 9 m vacuum facility. Base pressures during testing, as measured in the plane of the thruster, were 3×10^{-6} Torr-xenon. We used two ion saturation probes with a separation of 1 cm, following the method described in Ref. [15], to estimate oscillations in ion density. For the dispersion relation of the EDI [32] subject to the Hall thruster plasma properties it can be shown that these density measurements are a direct proxy for potential oscillations: $\hat{n}_i/n_{i0} \approx \hat{\phi}/T_e$, here $\hat{x}$ is the perturbed density or potential.

We placed the probes 6 mm downstream of the thruster exit plane, which was approximately 1-2 mm downstream of the location of peak $E \times B$ velocity. The probe signals were sampled at 100 MHz for 2 mega-samples, and then subdivided into 2000 realizations for ensemble averaging. As discussed in Ref. [15], this probing method relies on inserting an element into the plasma and thus may perturb the measurement. While we cannot preclude the possibility of probe-induced effects, we found thruster operation remained unchanged with probe insertion, and the features of the EDI spectra persisted in the downstream spatial locations where probe perturbations are expected to be less severe.

Leveraging these experimental methods, we first consider the ensemble averaged power spectra, $\langle X_f X_f^* \rangle$ and $\langle Y_f Y_f^* \rangle$ at each probe location. As Figure 5.3b) shows, the close correspondence between the two power spectra confirms our stationary assumption in this direction. Each spectrum in turn is characterized by broadband

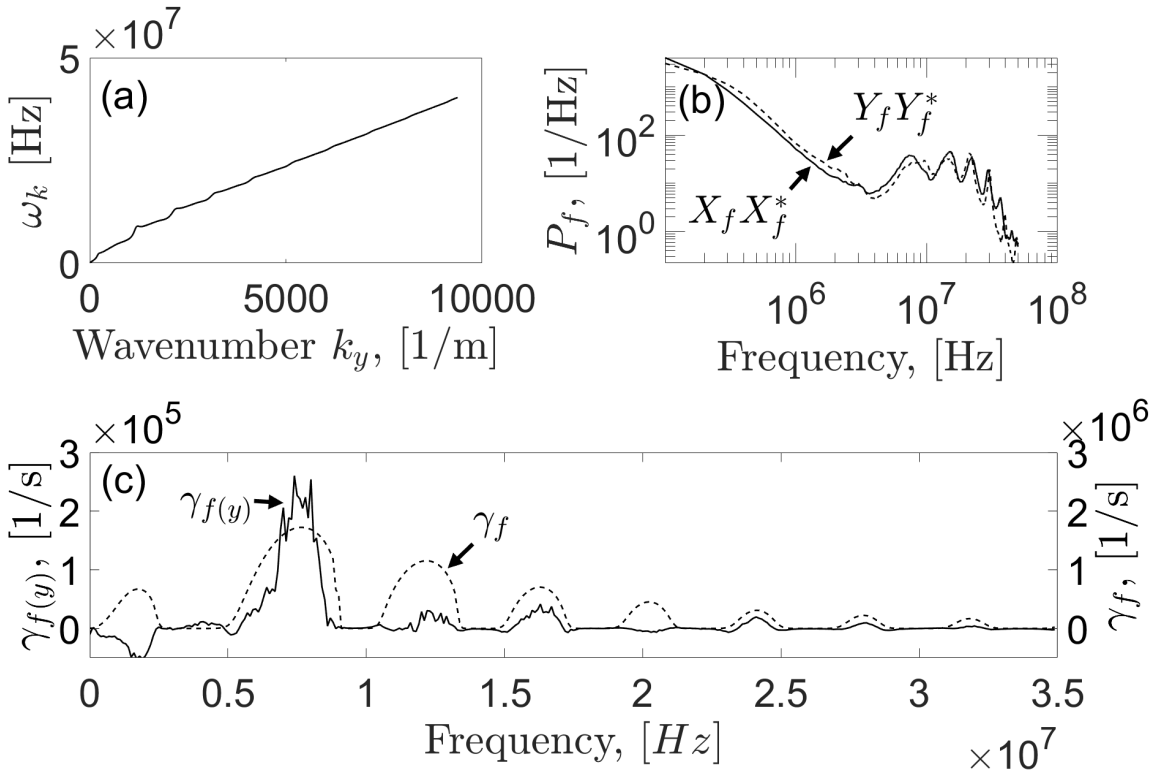

Figure 5.3: (a) Dispersion relation of the EDI at the probe location (b) Experimentally measured power spectra for both probe locations. (c) Comparison between the measured azimuthal growth rate $\gamma_{f(y)}$ (left axis) and the growth rate calculated from the dispersion relation γ_f (right axis).

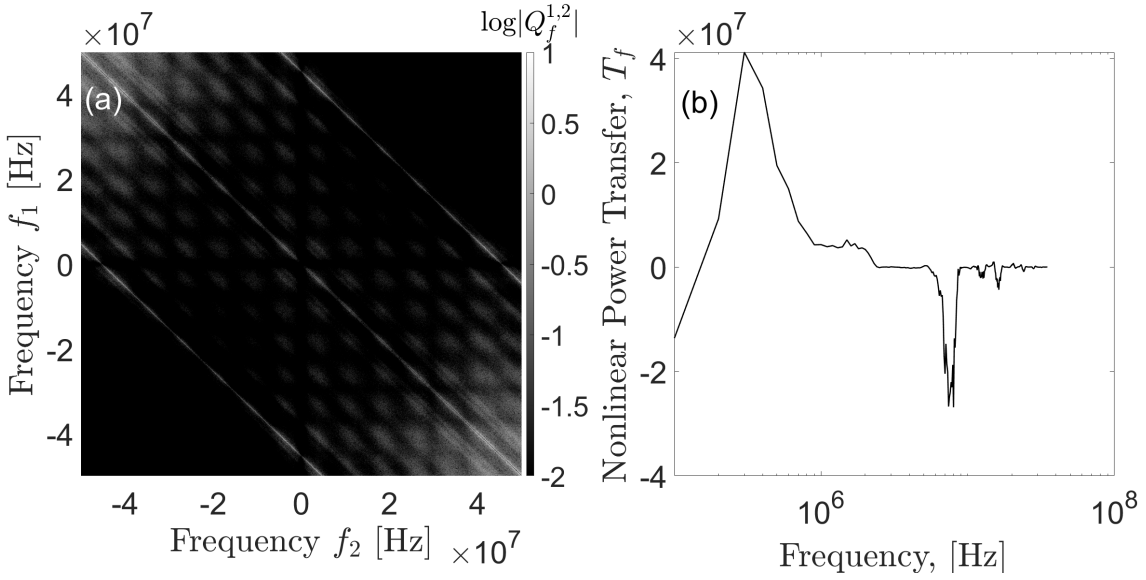

Figure 5.4: (a) Nonlinear power transfer function as a function of frequency. (b) Nonlinear transfer function ($|Q_f^{1,2}|$).

turbulence in the 100 kHz - 2 MHz range with discrete peaks spaced approximately 7 MHz in the high frequency range. We previously showed that these peaks are correlated with cyclotron resonances of the EDI (see Chapter IV).

Figure 5.3c) shows the azimuthal growth rate calculated from the adapted Ritz and Kim algorithm, $\gamma_{f(y)}$, compared to the growth rate predicted from the theoretical dispersion relation, γ_f, determined from Eq. 5.10. This result is, to the authors' knowledge, the first experimental measurement of EDI growth in this type of crossed-field device. We qualify this result though by noting we did not attempt to measure spatial gradients of the spectra in the axial and radial directions—finite values of these may lead to a difference in $\gamma_{f(y)}$ and γ_f. Regardless, we find a number of novel insights from the comparison of theory and measurement. First, there is qualitative agreement in the curve shapes—both trends exhibit peaked growth at several of the same frequencies. This is physically intuitive as these frequencies correspond to the cyclotron resonances where energy is most efficiently extracted from the plasma. Second, unlike the theoretical dispersion, the measured growth exhibits a negative value at the frequencies related to the MTSI ($f \sim 1.5$ MHz). This observation is a

departure from previous numerical studies of the MTSI where active damping was not observed, e.g [56]. Physically, our result suggests that the spectrum loses energy to the plasma at this smaller frequency/ longer length-scale. This damping could be attributed to a number of effects such as ion-neutral collisions or spatial gradients in the plasma preventing the propagation of long wavelength (low frequency) EDI/MTSI modes. Third, the magnitudes of the experimentally-measured azimuthal growth rates, $\gamma_{f(y)}$, are an order of magnitude smaller than the values inferred from the theoretical dispersion relation, γ_f.

We consider two limiting cases to interpret this last result. The first scenario is if spatial growth in the axial and radial directions is negligible compared to the azimuthal growth, $\gamma_f = \gamma_{f(y)}$. This is plausible as the instability's energy source is primarily in the $E \times B$ direction. In this case, our result would suggest there is a mechanism that maintains the shape of the theoretical growth but depresses the magnitude. Previous numerical studies on the EDI, for example, have proposed quasi-linear distortion of the electron distribution function by the waves may lead to such a result [63, 64]. As a second interpretation, we consider the case where there is finite spatial growth in the axial direction but neglect radial growth by symmetry. In this case, it can be shown that $\gamma_f \approx \gamma_{f(y)} + (v_p/2)P_f^{-1}\partial x P_f$—the total growth rate is the combination of the measurement and a contribution dictated by axial convection of wave energy. Assuming the typical gradient length-scales in the axial direction are on the order of 1 mm [15], the convective term could dominate such that $\gamma_f \approx (v_p/2)P_f^{-1}\partial x P_f$. This type of scaling, which is a major departure from linear theory, is consistent with previous numerical investigations where it was suggested that after quasi-linear distortion occurs, wave convection may dictate the growth [63, 64].

We next consider the nonlinear growth processes by showing in Figure 5.4a) the magnitude of the nonlinear transfer function ($|Q_f^{1,2}|$). The intensities in this result indicate the degree to which the frequency combination, f_1 and f_2, couples to a third

mode at $f_1 \pm f_2$. Negative frequencies in Figure 5.4a) denote taking the difference between f_1 and f_2. The near-zero amplitudes in the upper right and lower left quadrants generally indicate that there is no coupling from lower to higher frequency modes: $|f_1| + |f_2| > f_1, f_2$. There is an exception along the line where $f_1 + f_2 = 45$ MHz, but we suspect these results are non-physical as the spectral content in this region approached the noise floor. On the other hand, the intensities are largest with clearly defined peaks in the top-left and bottom-right quadrants and close to the -45° axis. The content in these regions indicates strong coupling from high to low order modes $|f_1|, |f_2| > f$. Physically, the combination of trends in Fig. 5.4a) are indicative of an inverse cascade where energy is non-linearly coupled from higher to lower frequency modes.

Fig. 5.4b) illustrates this inverse cascade explicitly by showing the total nonlinear power transfer rate, T_f. The negative peak at the high frequencies commensurate with the cyclotron resonances (f = 5-10 MHz) indicates that some of the energy that is linearly coupled into the waves from the plasma(Fig. 5.3c) is then transferred away through nonlinear processes. This energy is then deposited at the lower frequency range where the dispersion transitions into the MTSI (f < 2 MHz). This transfer is represented by the positive peak in T_f in this frequency range. The energy then is removed from the spectrum through linear damping (Fig. 5.3c). This experimental interpretation agrees with recent simulations that suggested the saturation of the EDI involves an initial linear growth of high frequency resonances followed by a nonlinear transfer of this energy to lower frequency oscillations[55, 56, 89]. Although, we note that comparisons to simulation are only appropriate for the final stationary state of the oscillations. Our experimental method only resolves the saturated state and cannot detect the different stages of evolution explored in Ref[56] before the instability reaches saturation.

In summary we have performed the first direct experimental measurements of

the nonlinear and linear growth of the EDI in a Hall thruster discharge. We in turn have shown that while the measured linear growth confirms the EDI is driven unstable by cyclotron resonances, there are notable departures from simple linearized theory. We also have found experimental evidence that a nonlinear energy cascade to lower frequencies and larger length-scales exists. Both of these experimental insights have direct implications for understanding the application-driven question of how this instability interacts with the fundamental plasma state. Indeed, in order to approximate "anomalous" wave-driven transport, we need to know both the effective growth rate and shape/magnitude of the power spectra [31]. As numerical simulations and experimental results have previously suggested, however, simple linear theory based on assuming a thermalized distribution is not sufficient to capture the actual growth rate[13]. Our experimental findings directly confirm this and moreover provide a potential path for directly estimating the wave-driven transport. By combining our measurements of the growth rate and power spectra, we can directly determine the degree of contribution of the waves to transport. Furthermore, the measurement of the growth rate as a function of position in the plasma could lead to simplified models of cross-field transport that would enable predictive modelling of crossed-field devices. To this point, one interpretation of our experimental results is that the growth rate may simply depend on wave convection. As was previously discussed in Ref. [64], this assumption may be leveraged to identify simple closure models. Finally, we remark that in order to make our measurements, we have used a technique adapted from previously derived bispectral analysis that is more conducive for use in low temperature plasmas with smaller devices. This same methodology, in principle, can be extended to a wide range of systems beyond the EDI to answer outstanding questions about the physics of transport-inducing instabilities.

Previous experimental efforts employing measurements of instability amplitudes to infer wave-driven electron transport showed disagreement with measured transport

levels[13]. It was theorized the discrepancies are due to a reliance on linear theory in the calculation of the wave driven transport while simulations indicate the growth and saturation of the EDI is very non-linear in nature[55, 56, 97]. The impact of the instability on transport is directly related to the magnitude of the instability's growth rate—the rate that energy is extracted from the electron $E \times B$ drift. Simulations have indicted that non-linear effects, such as distortion of the electron velocity distribution function (EVDF), can significant lower the magnitude of the growth rate[32, 63, 64]. Ref [63] demonstrated that these effects may be necessary to accurately predict the instability driven transport, using the growth rate from the quasi-linear dispersion relation consistently over-predicted cross-field transport. In the next section we apply experimentally measured growth rates to determine the cross-field transport due to the EDI in Hall thrusters.

5.4 Experimental Measurement of Collision Frequency

Building on the successful measurement of the non-linear wave properties of the EDI in the acceleration zone, a follow-up experiment was done to extend the measurement domain entirety of the near-field plume. This allows for calculation for the wave-induced transport as a function of position and is significantly more insightful than a singular value in the acceleration. As part of this new experiment some additional modifications were made to our model of EDI growth that allowed us to included additionally effects that were ignored in the previous experimental, such as growth along the axial direction. Furthermore, in order to validate our wave-induced transport value we needed to measure the actual cross-field transport in the thruster plume. In the sections we outline these changes to our model and experimental setup that enable us to measure and compare the EDI driven anomalous transport.

5.4.1 Modifications of the EDI growth model

As a reminder, in context of our experimental setup the Ritz and Kim technique allows us to calculate a term $\gamma_{f(y)}$, which we denote as the "azimuthal" growth and represents the projection of the total growth in the azimuthal direction:

$$\gamma_{f(y)} = \gamma_f - \frac{1}{2|X_f|^2}\left(\left[v_{g(x)}\partial_x|X_f|^2 + v_{g(z)}\partial_z|X_f|^2\right)\right]). \tag{5.20}$$

The "azimuthal" nomenclature stems from the fact that we are only measuring wave properties as they propagate in this direction. The other two terms in Eq. 5.20 represent the change in amplitude of the mode in the two directions orthogonal to the measurement.

Once we have measured the azimuthal growth rate, we in turn can relate it to the total growth rate through Eq. 5.20 provided we have measurements of the evolution of the magnitude of the wave amplitude as it evolves in the radial and axial directions. We neglect in this work the radial convective term due to symmetry but we do measure the change in power spectrum amplitude with axial location such that we approximate

$$\gamma_f = \gamma_{f(y)} + \frac{1}{2|X_f|^2}\left(v_{i(0)}\partial_x|X_f|^2\right)), \tag{5.21}$$

where we have made the assumption that for the EDI the axial group velocity is approximately the axial ion beam velocity[19]. As a final step, we remark that in the plasma, we measure the total growth rate of the waves. However, in order to determine the impact on the electron transport, we must isolate the electron contribution to the total growth rate: $\gamma_{e(f)} = \gamma_f + \gamma_{i(f)}$. This requires that we have an estimate for the ion contribution to the total growth.

In the near plume of Hall thrusters ion temperatures can become high enough that ion Landau damping terms, which are typically ignored in the EDI dispersion

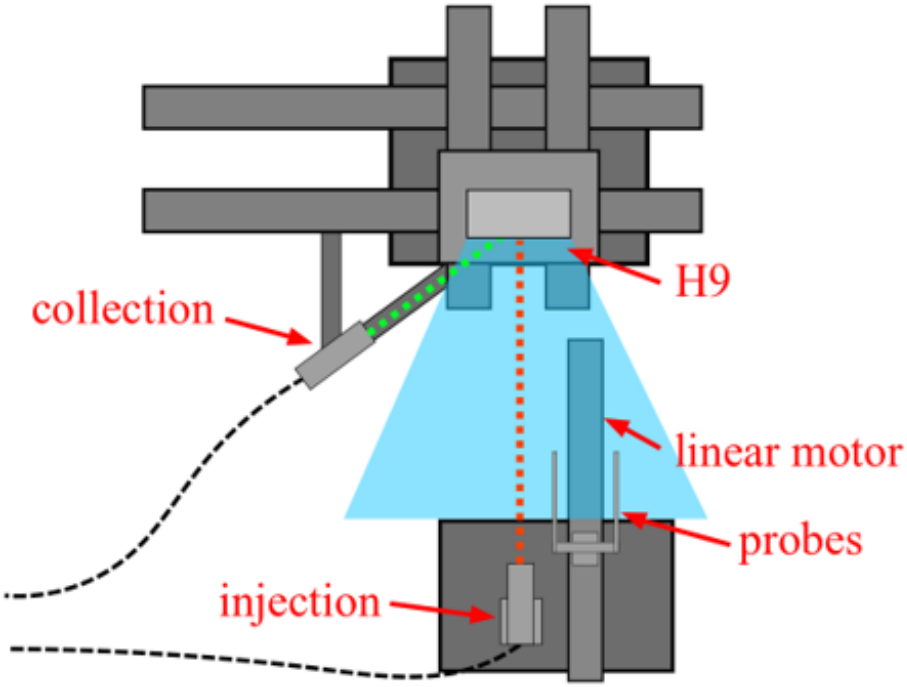

Figure 5.5: Schematic of experimental setup showing H9 Hall thruster installed in LVTF with LIF optics and wave probes mounted on a fast motion stage.

relation, could become significant[75]. We calculate the ion Landau damping rate as

$$\gamma_{i(k)} = -\sqrt{\frac{\pi}{8}} \frac{\omega_r(k)}{(1+k^2\lambda_D^2)^{3/2}} \left(\frac{T_e}{T_i}\right)^{3/2} e^{\left[\frac{-T_e}{2T_i(1+k^2\lambda_D^2)}\right]} \tag{5.22}$$

where we assume the ion temperature is 0.25 eV throughout the measurement domain.

In summary, the wave driven collision frequency is calculated using Eq. 5.4 where we determine the local plasma parameters using a LIF technique discussed in the following section, the growth rate and oscillation amplitude using high speed probes and the Ritz method, and lastly we estimate the wavenumber and real part of the dielectric function for the EDI as functions of frequency using Eq. 5.10. Finally, we estimate the electron growth rate from the measured azimuthal growth rate based after considering axial wave energy convection and ion Landau damping.

5.4.2 Diagnostics

We employed two core diagnostics in our experiment: ion saturation probes that measure the oscillations used in the Ritz and Kim method, and laser-induced fluorescence (LIF) used to measure the ion beam velocity. Additionally, we outline a technique used to infer the background plasma parameters and anomalous collision frequency from the LIF data.

5.4.2.1 Ion saturation probes

We employed two ion saturation probes for measuring the fluctuations in ion density. The probes consisted of 0.38 mm radius tungsten rods with an exposed length of 3.8 mm. These cylindrical probes were separated azimuthally by 1 cm and mounted on fast motion stages to quickly the inject the probes in the plume and minimize perturbative effects. The probes collected data at fixed locations along channel centerline from 0.125 to 0.75 channel lengths downstream of the thruster exit plane. The ion saturation probes are biased to -45V using batteries to collect only ion current. The current is read across a low-inductance and low-capacitance 100Ω resistor into a ATS9462 16-bit digitizer. The signal was sampled at 100 MHz for 2 Mega-samples and the resulting waveform was then subdivided into 2000 realizations for averaging. The fluctuations in ion saturation are then related to fluctuations in plasma potential by relate measured fluctuations in the ion saturation current to plasma density fluctuations for use in Eq. 5.4 as $\delta i/i_0 \approx \delta n_i/n_{i(0)}$.

As we discuss in Section III.B.3, the ion saturation probes also provide an estimate of the downstream plasma density for use as a boundary condition in calculating the axial ion density profile. We determine the ion density from the measured ion saturation current as

$$n_{i(0)} = \frac{i_{sat}}{eA_pC_s \exp(1/2)} \tag{5.23}$$

where A_p is the area of probe and $C_s = \sqrt{eT_{eV}/m_i}$ is the ion sound speed. The electron temperature is determined using the LIF technique covered in Section III.B.3. We will discuss in Section IV the uncertainties introduced with this equation that propagate to the calculation of anomalous collision frequency.

5.4.2.2 IBIS method

Following the works of Perez-Luna and Dale, we determine plasma density, electric field, electron temperature, ion beam velocity, and anomalous collision frequency non-invasively through laser-induced fluorescence (LIF) measurements[83, 29]. This analysis method, known as the ion Boltzmann implicit solution method (IBIS), starts with the 1D ion Boltzmann equation where ionization collisions are considered:

$$\frac{\partial f}{\partial t} + v_i \frac{\partial f}{\partial x} + \frac{e}{m_i} E_{x(0)} \frac{\partial f}{\partial v_i} = \left(\frac{\partial f}{\partial t} \right)_{iz}. \tag{5.24}$$

In this equation v_i is the axial ion velocity and the right most term is the time rate of change in the IVDF due to ionization. Assuming the IVDF is at steady state in time, higher order moments of the Boltzmann equation can be taken to yield equations containing several of the need plasma parameters:

$$\frac{\partial v_i n_{i(0)}}{\partial x} = n_{i(0)} f_{iz} \tag{5.25}$$

$$\frac{\partial v_{i(0)}^2 n_{i(0)}}{\partial x} - \frac{e}{m} n_{i(0)} E_{x(0)} = 0 \tag{5.26}$$

$$\frac{\partial v_{i(0)}^3 n_{i(0)}}{\partial x} - 2\frac{e}{m} n_{i(0)} E_{x(0)} \overline{v_i} = 3\frac{e}{m_i} T_i n_{i(0)} f_{iz} \tag{5.27}$$

Here $v_{i(0)}$ is the mean ion velocity and T_i is the temperature of newly born ions which we assume is equal to the neutral gas temperature. With the spatial resolved LIF measurements, this system can be solved for $E_{x(0)}$, f_{iz}, and $d\ln(n_{i(0)})/dx$. This last variable can then be integrated across the axial domain to determine the ion density

if the density is known at one of the boundary points x_b:

$$n_{i(0)}(x) = -\exp\left[\int_{x_b}^{x} \frac{d\ln n_{i(0)}}{dx}\right] + n_{i(0)}(x_b) \tag{5.28}$$

This downstream density ($n_{i(0)}(x_b)$) is estimated with the wave probes that also function as ion saturation probes for measuring ion density. With this information, in addition to the value of the applied magnetic field, we can calculate an effective total electron collision frequency ($\nu_e = \nu_c + \nu_{AN}$) using Ohm's Law

$$\nu_e = \frac{\Xi \pm \sqrt{\Xi^2 - \left[2v_{ex(0)}B_r\right]^2}}{2\frac{m_e}{e}v_{ex(0)}} \tag{5.29}$$

where $v_{ex(0)}$ is the axial electron velocity and we define $\Xi = E_{x(0)} + \frac{\nabla q n_{e(0)} T_e}{n_{e(0)}} - \eta_i j_i$, where $\eta_i = m_i\nu_c/q^2 n_{i(0)}$ is the classical ion resistivity due to collisions and j_i is the ion current density.

5.4.3 Results

In this section we present the results of our investigation, starting first with plasma parameters determined from the IBIS technique and then the wave estimated collision frequency. Here we will also provide a brief discussion on the sources of uncertainty in each diagnostic.

5.4.3.1 Background plasma properties

We show in Figure 5.6 four key plasma parameters inferred from the IBIS method—ion velocity, electron temperature, electric field strength, and plasma density—as a function of axial distance from the anode normalized by the channel length, L. As can be seen, the electron field is peaked downstream of exit plane of the thruster at $x/L = 1.1$. The majority of the ion acceleration subsequently occurs in this region of

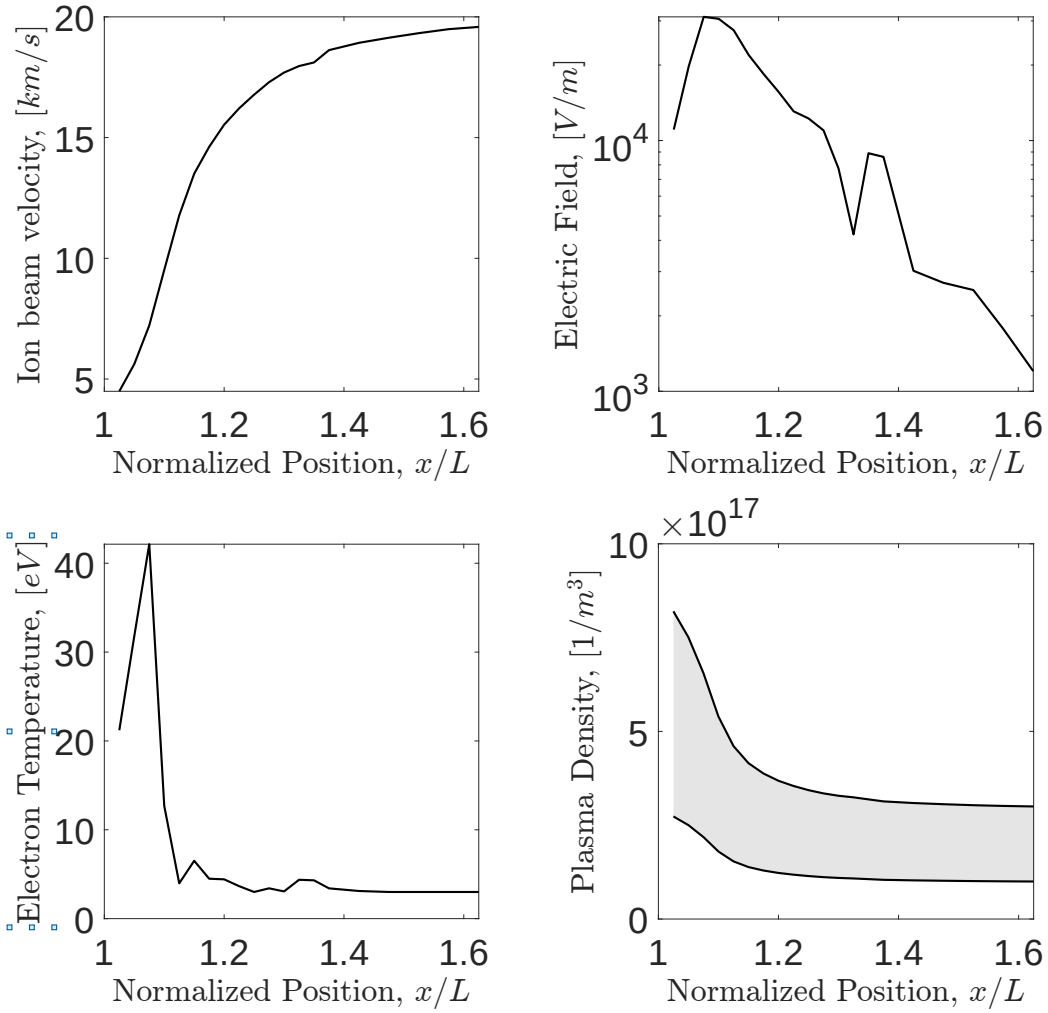

Figure 5.6: Plasma properties inferred from LIF measurements. a) Ion beam velocity, b) axial electric field, c) electron temperature, and d) ion density as a function of axial position normalized by the channel length where x/L = 1 is the exit plane of the thruster.

high electric field between $x/L \approx 1$ and $x/L \approx 1.4$. The majority of ionization occurs at the start of the acceleration zone, and due to Ohmic heating results in the sharp peak in electron temperature at this location. Similarly, the plasma density is peaked at the exit plane and decays downstream as the ions are accelerated and diffuse downstream. For the plasma density profile, we show a range of possible values stemming from different choices for the downstream boundary condition. We estimate a mean plasma density of $\approx 2 \times 10^{17}$ m^3 from our ion saturation probe and Eq. 5.23, but consider a range between $1 \times 10^{17} < n_e < 3 \times 10^{17}$ due to uncertainty. This uncertainty in the downstream density does not affect the other plasma parameters calculated with the IBIS method as they are calculated directly from the ion-moments. The only exceptions are the classical collision frequency that depends on ion density and the total collision frequency (Eq. 5.29) that depends on ion density in the estimation of the axial electron velocity. We discuss the influence of the uncertainty in density on these two parameters in the following section.

5.4.3.2 Wave properties

In this section we consider the two measured wave properties used in Eq. 5.4: the oscillation power spectrum $\left|\frac{\delta n_{i(f)}}{n_{i(0)}}\right|^2$ and electron growth rate $\gamma_{e(f)}$. We show the power spectrum inferred by the wave probes in Figure 5.7 at various positions in the plume. Here several distinct harmonics are visible starting at ~7MHz. From our work in Chapter IV. we know these are the frequencies corresponding to the electron cyclotron resonances of the EDI[15, 16]. Along the channel centerline, the oscillations are at their strongest in the acceleration zone and decay further downstream, but notably the oscillations appear to start trending up in strength at the end of the domain. Although, as we will show, the anomalous collision frequency is at its minimum value in the acceleration region despite the oscillations being strongest at this location.

The measured and theoretical electron growth rates, γ_e, are given in Fig. 5.8

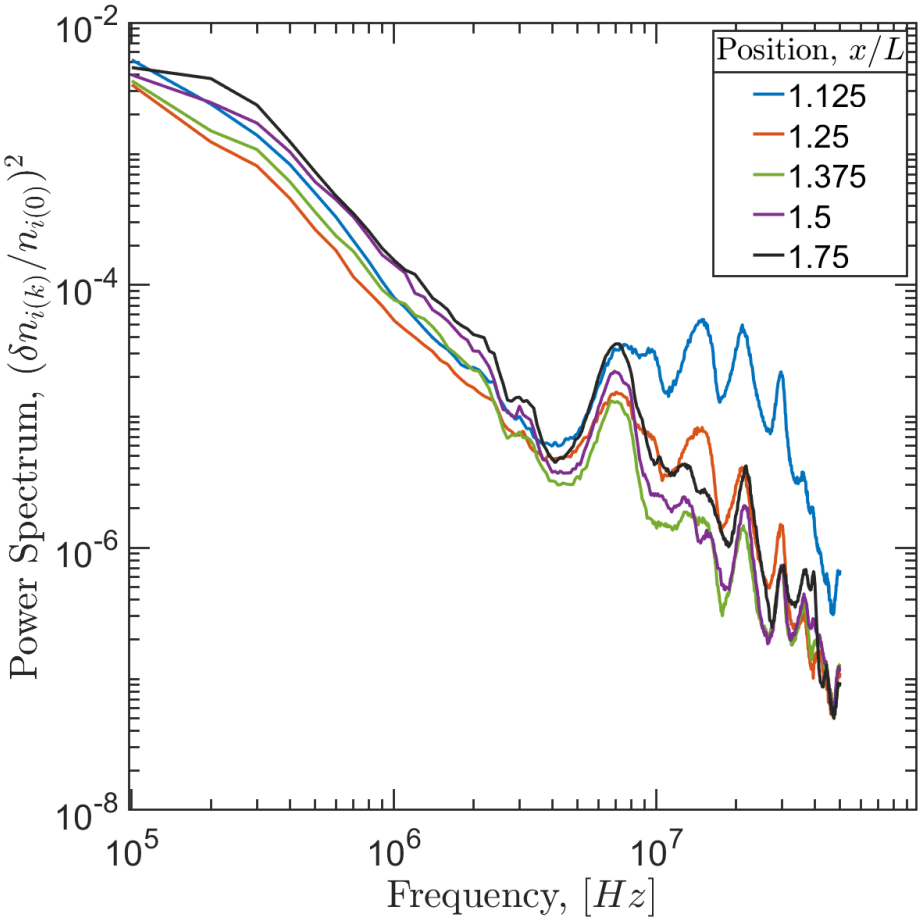

Figure 5.7: Power spectrum of density oscillations as measured by wave probes at various positions in the near-field plume.

for a location in the acceleration zone ($x/L = 1.25$) and in the downstream plume ($x/L = 1.75$). In these plots, the theoretical value is calculated from the dispersion relation (Eq. 5.10) and the measured value is calculated from the Ritz and Kim technique after considering axial energy convection (Eq. 5.21) and adding the ion Landau damping term($\gamma_e = \gamma_f - \gamma_i$). We also consider a result where we ignore ion damping. This is equivalent to assuming the total growth rate is solely due to the electron contribution ($\gamma_e \approx \gamma_f$).

In the theoretical growth rate curve, at the higher frequency there are small dips in growth rate within the cyclotron harmonics, e.g. $f \approx 16$ MHz in Fig. 5.8(a). These dips are the result of the binning method discussed in Section II.B. we use to convert between wavenumber and frequency space. Here, wavenumbers in the unstable cyclotron harmonics have the same real frequency as wavenumbers in-between the harmonics where the growth rate is low. The averaging within the frequency bin yields the dip in the growth rate curve. Additionally, the discontinuities in the measured growth rate, without the ion Landau damping term, correspond to frequencies where the total growth rate is near zero or negative—indicating the wave is damped at those frequencies.

In the acceleration region (Fig. 5.8(a)), the cyclotron harmonics are visible in both the theoretical and measured growth rates, and the amplitudes are generally comparable. Without the ion Landau damping term, the measured growth rate is weaker than the theoretical quasi-linear, but after adding ion Landau damping the measured value is larger than the theoretical. This contrasts our initial results in Section 5.1 that showed the azimuthal growth rate was almost order of magnitude lower than the theoretical value in this region and highlights the importance of considering axial wave energy convection and the ion contribution to the growth rate. In the downstream region, the measured electron growth rate, both with and without ion Landau damping, is significantly stronger than theoretical value. The smoothness of

the measured growth rate curve, with ion Landau damping, stems from the ion term being significantly larger than the total growth rate measured using the Ritz and Kim method ($|\gamma_i| >> |\gamma_f|$). As we show in the next section, the increased amplitude from the ion Landau damping term is necessary for calculating an accurate anomalous collision frequency.

5.4.3.3 Anomalous collision frequency

Using the methods described in Section 5.2, we calculate the anomalous collision with Eq. 5.4 using the measured power spectrum and growth rates shown in the preceding section along with background plasma parameters calculated from the IBIS technique and terms inferred from the real part of the theoretical EDI dispersion relation. When solving the dispersion relation we have assumed an axial propagation angle of 15 degrees ($k_x = k_y \sin(15^o)$) based on previous measurements[101, 15] and a radial wavenumber of $k_z \lambda_{De} = 0.02$. This radial wavenumber was selected such that the radial wavelength is on the order of the channel width—as observed in recent simulations[89, 64, 95, 56]. In Figure 5.9, we show possible collision frequency profiles using the measured electron growth rate, both with and without ion Landau damping, as well the quasi-linear result where we use the growth rate calculated from the theoretical dispersion relation (Eq. 5.10). We compare these results with the collision frequency determined from the IBIS method and the classical particle based collision frequency. As discussed in Section III.B.3, there is uncertainty in the density profile arising from different assumed boundary conditions for the downstream density in the IBIS method. We propagate the uncertainty by repeating our analysis and calculation of anomalous collision frequency for each possible density profile. For the wave driven collision frequency, the uncertainty propagates due to the dependence on density in the real part of the dispersion relation and the ion Landau damping term. For the collision frequency inferred from the IBIS technique, the uncertainty

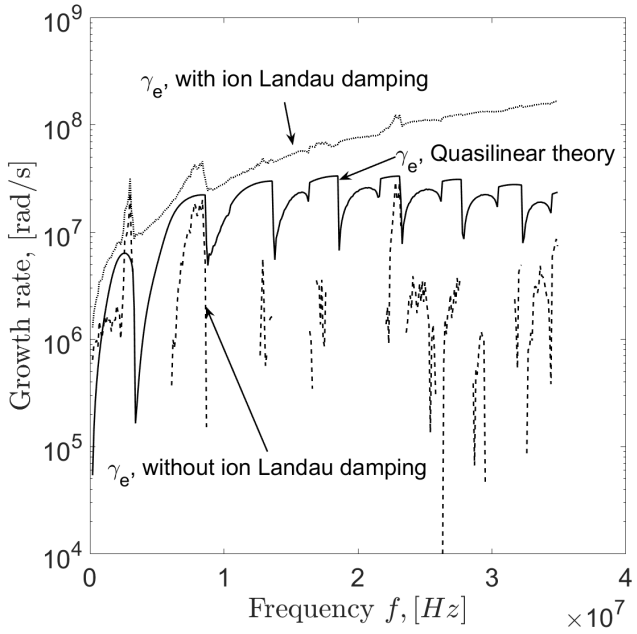

(a)

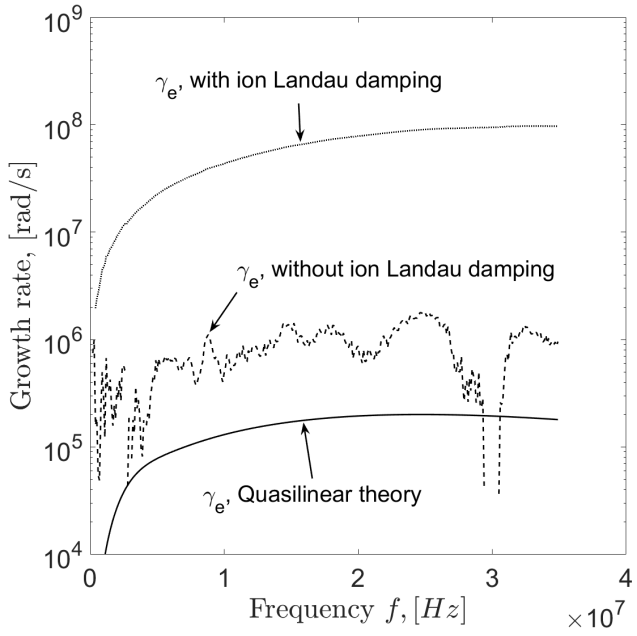

(b)

Figure 5.8: Measured and theoretical growth rates in the acceleration region x/L = 1.25(a), and downstream plume x/L = 1.75 (b). Two curves are shown measured growth rate, both with and without adding the ion Landau damping contribution. The growth rate labelled 'Quasilinear theory' is theoretical value determined from the solution of the dispersion relation, Eq. 5.10

comes from the influence of density in the estimation of the axial electron velocity (see Chapter 3).

The collision frequency profile inferred from the IBIS method has a minimum value approaching the order of the classical collision frequency at the location of peak electric field ($x/L = 1.125$) and then increases monotonically by over an order of magnitude going downstream. The theoretical result, using the quasi-linear growth rate, overestimates the collision frequency slightly at the acceleration zone but quickly decays to a roughly constant value downstream that significantly underestimates the collision frequency. Without considering ion Landau damping, the measured wave-driven anomalous collision frequency follows the same trend as the IBIS result, but under-predicts the anomalous collision frequency by roughly an order of magnitude. Although, there is slightly better agreement in the acceleration zone. After including ion Landau damping, the wave-driven result matches the IBIS values to within the uncertainty at nearly every axial position. We discuss possible reasons for these trends in the next section.

5.4.4 Discussion

As expected the collision frequencies determined using the theoretical growth rate from the EDI dispersion relation do not correlate with the actual collision frequency profile. For the acceleration zone this can be explained by non-linear effects that would lower the effective growth rate of the EDI, for example by changing the electron velocity distribution function. This type of effect has been previously demonstrated in simulations of the EDI in the Hall thruster channel[63, 64]. Downstream, where the theoretical result significantly under-predicts the collision frequency, the situation is more unclear. One potential explanation stems from the choice in radial wavenumber when calculating the dispersion relation. We assumed a wavenumber that was on the order of the channel width, but downstream this restriction does not necessarily hold.

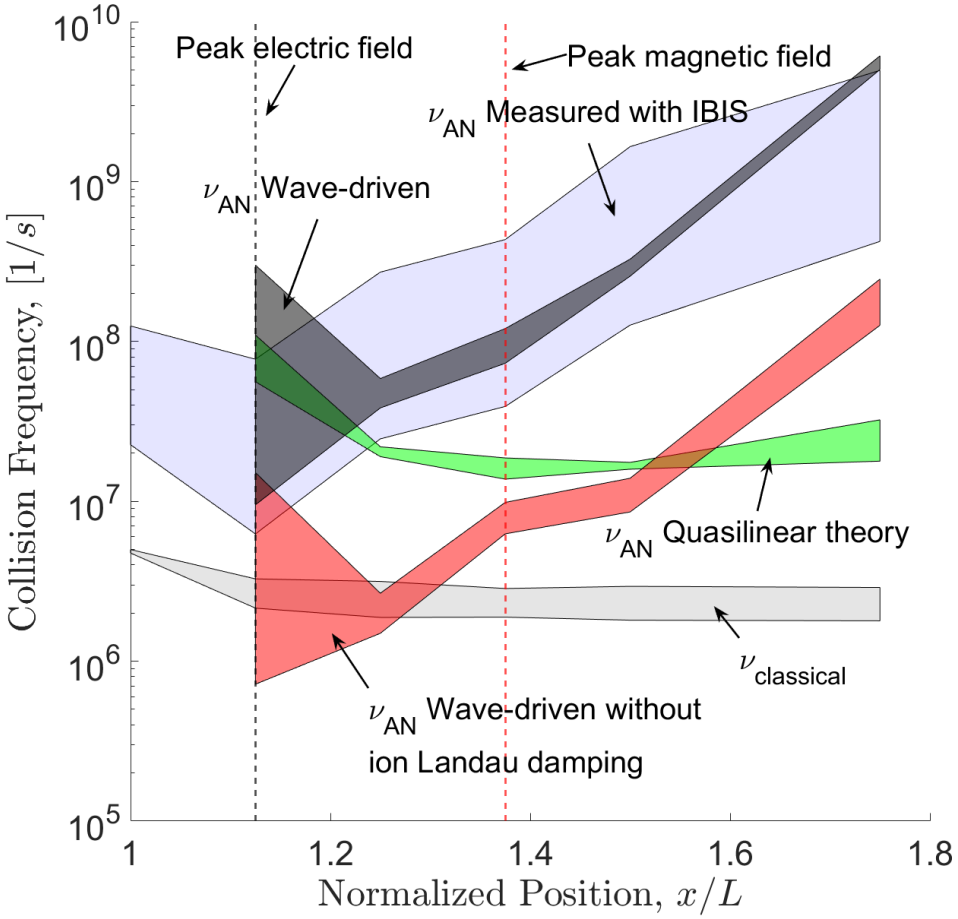

Figure 5.9: Anomalous collision frequency determined from LIF and wave measurements as a function of normalized position in the Hall thruster plume. Two wave-driven results are shown based on calculating the electron growth rate with and without including ion Landau damping: ($\gamma_e = \gamma_f - \gamma_i$ and $\gamma_e = \gamma_f$). The theoretical quasi-linear result using the growth rate calculated from Eq. 5.10 and the classical particle collision frequency are also shown for reference.

The radial wavenumber could be much smaller than at the acceleration zone. The magnitude of the quasi-linear growth rate strongly depends on the radial wavenumber and if the wavenumber is an order of magnitude smaller the growth rate would increase by a similar scale. We show this effect in Fig. 5.10 by plotting the peak growth for the theoretical dispersion at $x/L = 1.75$ for different values of k_z. This would raise the collision frequency profile up where the downstream value may be in agreement with the LIF measurements. It is possible that the radial wavenumber changes as the wave propagates downstream and would permit a large radial wavenumber at the acceleration zone and a small wavenumber downstream such that agreement with the measured IBIS collision frequency is possible everywhere in the plume, but experimental efforts to measure the radial wavenumber have proven difficult[15, 14].

Regardless of whether the theoretical values can be adjusted to better align with the measured collision frequencies, the result calculated using the growth rates inferred from Ritz and Kim method, and including ion Landau damping, strongly agree with the baseline IBIS result. While early in the acceleration region ion Landau damping is not extremely significant due to the locally high electron temperature, downstream the ion Landau damping amplitude entirely governs the calculated electron growth rate and anomalous collision frequency. If we assume the EDI is marginally stable, $\gamma_f \approx 0$, the anomalous collision frequency can be predicted solely by Eq. 5.22, the measured oscillations amplitudes, and estimates of the background plasma parameters. Furthermore, with the oscillation amplitude approximately constant in the downstream plume (see Fig. 5.7), the wave energy can be approximated as saturated. For example, the wave energy could be saturated at a fraction of the plasma thermal energy ($n_{e(0)}T_e$) or azimuthal drift energy ($m_e v_{e(y)}^2$). With these assumptions, the collision frequency can be determined almost solely with the local plasma parameters. This could lead to a reduced order model of a Hall thruster that accurately captures the effect of the EDI but without needing a high fidelity simulation of the electron

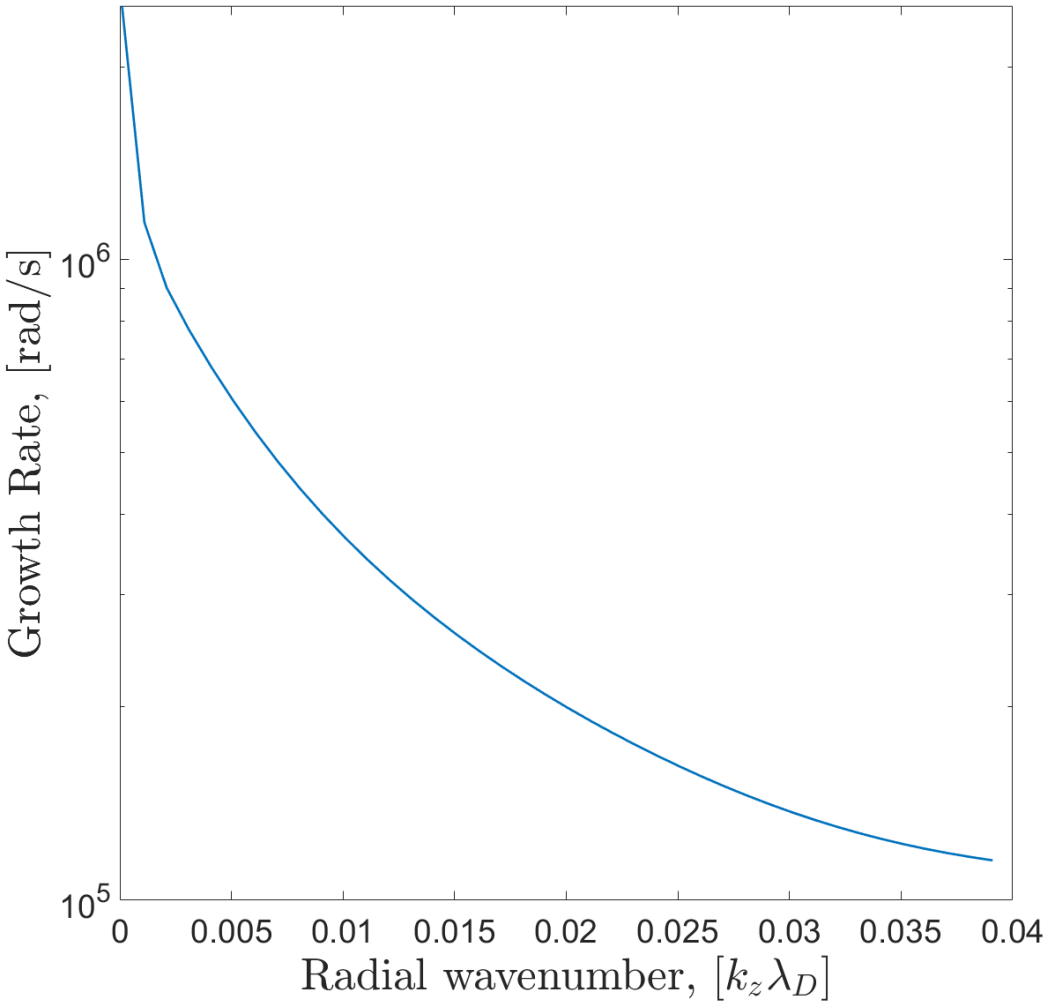

Figure 5.10: Maximum linear growth predicted for the EDI by solving the quasi-linear dispersion relation for the plasma parameters at the farthest downstream point ($x/L = 1.75$) over a range of possible radial wavenumbers (k_z)

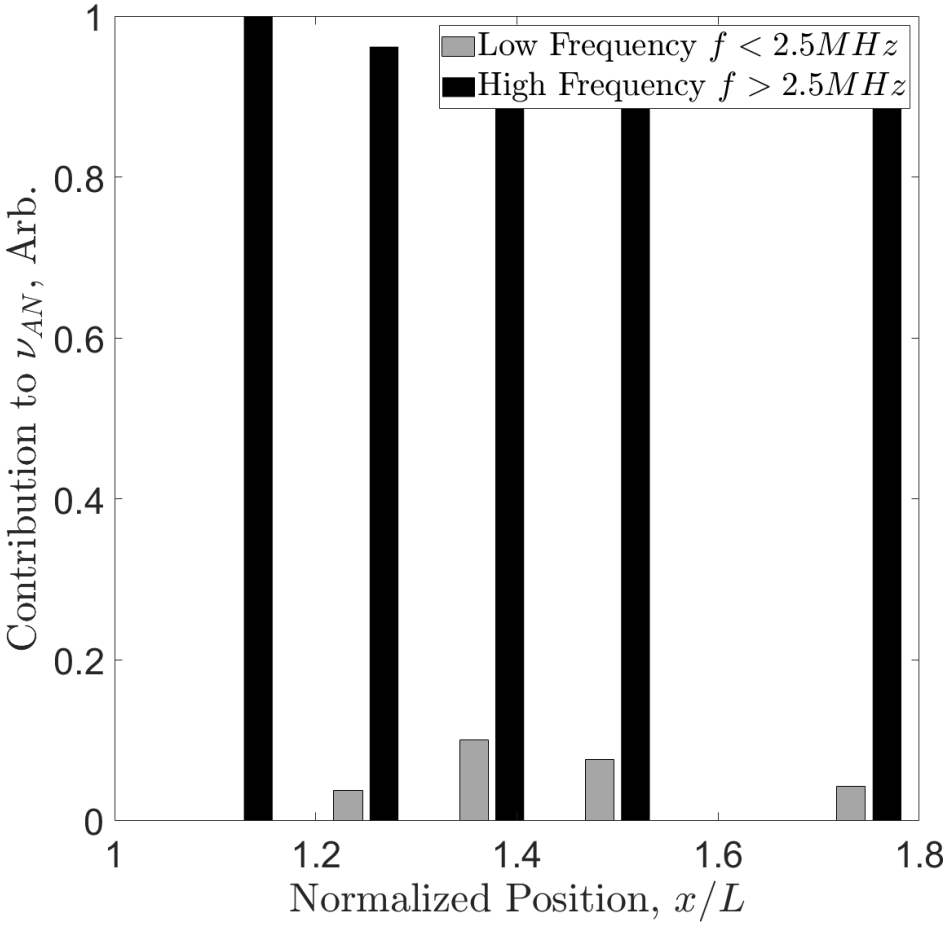

Figure 5.11: Relative contribution to anomalous collision frequency for low frequency oscillations ($f < 2.5MHz$) and high frequency oscillations ($f > 2.5MHz$) at various points in the plume.

population.

In the context of recent simulations of the EDI, our results validate the importance of the EDI on anomalous transport in Hall thrusters, but we highlight some key differences. While many simulations have demonstrated the EDI can be sufficient to explain the anomalous transport seen Hall thrusters, most of these simulations resolve the EDI with an ion-acoustic-like dispersion[63]. Only a subset of simulations have resolved the EDI with distinct harmonics[55, 56], and these works also predicted the non-linear cross-lengthscale energy exchange we observed in Ref. [16]. Although, while those simulations did predict EDI enhanced transport they observed most of the cross-field electron transport occurred at the low-frequency and long wavelength features of the EDI—the MTSI component discussed in Section II.B. In this work we observe most of the anomalous transport occurs due to the oscillations at the high frequency cyclotron harmonics. In Fig. 5.11 we show the relative contribution of to anomalous transport, in the case where we include ion Landau damping, due to oscillations at frequencies below 2.5 MHz, corresponding to the MTSI, and above 2.5 MHz that represent the cyclotron harmonics. The relative contribution is calculated by performing the summation in Eq.5.4 over the frequency range of interest and normalizing by the total summation. In the acceleration zone, there is virtually no influence of the MTSI frequencies on the cross-field transport. Looking downstream the low-frequency oscillations begin to play an increasingly important role, but the high frequency oscillations remain dominant. Although, we are limited in this experiment by the axial domain of the LIF measurements and cannot calculate collision frequency further than $x/L = 1.75$, and previous measurements of have shown the wave energy continues to increase at low frequency further downstream[15]. This implies that the low frequency waves could become dominant in the far-field plume.

5.5 Conclusion

We performed a novel calculation of wave driven anomalous collision frequency. We utilized a bispectral analysis technique and ion Landau damping model to infer the electron growth rate at several positions in the Hall thruster plume. We demonstrated that the measured growth rates are indicative of the electron drift instability, and through linear theory we used the measured growth rates to calculate a wave-driven anomalous collision frequency. The wave-driven collision frequency showed strong agreement with the true collision frequency profile inferred from LIF measurements. While our results validate the large body of simulation work that demonstrate the EDI controls the cross-field transport in Hall thrusters, there still remains some ambiguity between simulation and experiment. Most notably, our results show the anomalous transport is driven primarily by the EDI cyclotron harmonics while simulations show the transport is driven mostly by either an ion-acoustic-like form of the EDI or the low-frequency MTSI component. Finally, we highlight that our results could lead to simplified Hall thruster models that self-consistently capture the wave-driven transport without needing to resolve the EDI in high-fidelity simulations.

CHAPTER VI

Conclusions and Future Work

6.1 Summary of Work

Hall thrusters are currently the workhorse of the electric propulsion system due to their high efficiency, relatively simple design, and extensive testing heritage. Despite their widespread use and technological maturity, the fundamental physics governing Hall thruster operation remain unsettled, namely the anomalous cross-field electron transport. While several mechanisms have been proposed to address this enhanced transport, none have been successful in producing a model that can reliably and accurately simulate and predict Hall thruster performance. Recent simulation work has pointed toward instability-driven electron transport, but there has been virtually no experimental evidence to support this theory. In this work, we have used experimental techniques to develop a stronger understanding of both the nature of instabilities in Hall thrusters and their impact on cross-field transport.

First, we used ion saturation probes to measure the power spectrum and dispersion relation of plasma oscillations in the Hall thruster plume, and in particular at the acceleration zone. The measured dispersion relation was determined to be characteristic of the electron drift instability in a form with distinct cyclotron harmonics. This contrasted with previous results that expected the EDI dispersion relation to be ion-acoustic-like in nature. The spatially resolved power spectrum showed that as the

instability travels downstream, it undergoes an energy exchange across length scales where the cyclotron resonances appeared to give up their energy to oscillations at frequencies significantly below the fundamental cyclotron resonance, later identified as the modified two-stream instability.

We then applied quasi-linear theory to estimate the cross-field transport induced by the measured instabilities. We found that using quasi-linear theory with our measured wave amplitudes did not match the transport profile measured with laser-induced fluorescence. In light of this result, and some recent simulations that highlight the nonlinear nature of the EDI, we developed a bispectral analysis framework that could measure nonlinear wave-wave interactions in a Hall thruster plasma. This work revealed the highly nonlinear nature of the EDI, and in particular verified simulations that predicted an inverse energy cascade from the EDI cyclotron resonances to the low-frequency and long-wavelength MTSI. Additionally, this bispectral analysis technique was used to estimate the linear growth rate of the EDI. The measured linear growth showed substantial deviation from the measured growth in both form and amplitude. We next used the measured linear growth and different wave energy saturation models to estimate cross-field transport. This methodology yielded electron transport profiles that largely succeeded in matching the measured transport levels that simple quasi-linear theory failed to reproduce, and agreed well with the expected transport profile.

6.2 Impact of Work

At the beginning of our research, the root cause of anomalous electron transport in Hall thrusters was a decidedly unsettled question. A growing number of simulations were beginning to point towards plasma turbulence, and in particular the electron drift instability, but there was limited experimental backing for any of these theories. Our work set out to address these concerns and provide experimental insight into the

EDI and its effect on Hall thrusters. While it was a bold endeavor, we attempted to answer two short but difficult research questions: does the EDI exist in Hall thrusters, and is it responsible for anomalous transport?

6.2.1 Does the Electron Drift Instability exist in Hall thrusters

As a reminder, prior to this work, the only experimental evidence for the EDI came from a single series of Collective Thomson Scattering experiments[99] that, while incredibly encouraging, were still inconclusive and invited just as many new questions regarding the EDI in Hall thrusters as they answered. Chief among these questions were 1) At what frequencies and wavelengths is the EDI the strongest? and 2) Should the EDI exhibit an ion-acoustic-like dispersion for the conditions of the Hall thruster plasma? Our experimental research discussed in Chapter IV largely addressed most of these concerns.

Our use of high-speed electrostatic probes allowed us to resolve a wider spectrum of oscillations than were accessible to the Thomson Scattering diagnostic. While the previous efforts of Livtak[69] and Lazurenko[67] took similar experimental approaches with electrostatic probes, our diagnostic had several improvements that allowed us to measure a much larger region of the thruster, particularly probing directly into the acceleration zone, with greater signal resolution and resistance to perturbation of the thruster. Chapter III provided an overview of this high-speed diagnostic system that enabled most of the research data utilized throughout our work.

In Chapter IV, we used this new experimental diagnostic system to detect previously unmeasured plasma wave signatures. In the low-frequency domain, we presented the first measurement of an ion-acoustic-like wave that appears to grow well past the Hall thruster's acceleration zone and contains a significant amount of wave energy. Additionally, we discovered distinct high-frequency wave content with harmonic-like frequency spacing, with increasing wave energy closer to the acceleration zone.

Through a rigorous analysis of the EDI dispersion relation, we were able to confidently identify the high-frequency oscillations as the EDI with its cyclotron harmonics intact, in contrast to the Thomson scattering results from a few years prior. We presented several potential theories explaining this discrepancy, and more recently, simulations have shown agreement with our experimental results as the numerical models are refined and become more representative of the true thruster geometry and conditions. Additionally, our data gave confidence to novel simulation results that demonstrate the importance of non-linear dynamics in determining the final form of the EDI after growth and saturation. Most importantly, we concluded that the low-frequency wave we observed grows non-linearly through an inverse energy cascade from the high-frequency cyclotron harmonics.

Overall, our results provided a new perspective on the electron drift instability that will continue to be a valuable reference point as simulations and models develop further. Despite the limitations of our techniques, we were able to confidently answer our first research question with a firm yes: the EDI does exist in Hall thrusters. However, similar to the Thomson Scattering experiments, our research prompted just as many questions as it addressed, mostly centering around the little-explored non-linear nature of the EDI. In Chapter V, we addressed several of these questions and used that information to answer the second core research question of our work: Is the EDI that we measured sufficient to drive anomalous transport?

6.2.2 Does the Electron Drift Instability explain anomalous transport

Building on our promising early work where we were able to identify the electron drift instability through electrostatic probing methods, we then turned to determine how we can use our probe data to determine wave-induced electron transport. The electron drift instability is not the only mechanism that could drive enhanced transport, and it is not even the only instability present in Hall thrusters that could cause

wave-induced transport. In Chapters II and V, we presented our transport model linking the measured density perturbation amplitudes to anomalous electron transport, and it quickly became apparent that due to significant non-linearity governing the EDI, a simple linear model was insufficient.

We heavily used the Ritz and Kim bispectral analysis technique to determine the growth dynamics of the EDI and relate it to anomalous transport levels. While the numerical technique we applied is not novel, its usage in low-temperature and density plasmas is a new development. The bispectral analysis technique has been used extensively in the fusion plasma community for years to characterize plasma turbulence, but due to the sensitivity of the analysis method, it is not easily extendable to Hall thruster plasmas where the signal levels are weak at low density and the noise floor can be very high. In Chapter III, we discussed several features and experimental techniques employed to make our system robust enough to overcome these shortcomings that would otherwise doom the bispectral analysis to yield junk data. While we used the diagnostics and technique to study the EDI in Hall thrusters, it could be extended to allow new non-linear wave dynamics research in similar low-density plasma systems.

Through the use of the bispectral analysis system, we were able to both yield new insight into the non-linear behavior of the EDI and demonstrate that the EDI is very likely responsible for the observed anomalous electron transport. While there is still much work to be done before predictive Hall thruster modeling is fast, robust, and accurate, the results and models presented here move us closer towards the final goal. While we hope to have answered our central research questions—does the EDI exist in Hall thrusters and is it responsible for anomalous transport—this work has several limitations and has prompted more potential projects. In the next sections, we discuss the limitations of our research and present several thoughts on what future work may entail.

6.3 Limitations of this work

Despite the several new insights borne out of this research endeavor, there were several limitations to our experimental techniques and analysis methods that prevent our conclusions from being completely definitive. At the heart of all of our experimental investigations, we relied primarily on electrostatic probes being inserted directly into the thruster plume to record plasma waves. While we provide significant detail in Chapter III about our efforts to minimize any potential perturbations of the system, due to the complexity of the plasma system, it is impossible to fully characterize what effect our diagnostic tools have on the plasma instabilities. Furthermore, most of the waves we were analyzing possess length-scales smaller than what our probe can directly measure (see the anti-alias discussion in Chapter III). While a significant amount of work and modeling was presented in Chapter IV to give confidence in our results, it would be more conclusive if we could directly probe the relevant length-scales, but this is currently not possible, even for laser-based diagnostics.

Another limitation that might be more significant for interpreting our results and comparing them to previous experiments is the specifics of the unit under test. As we mention throughout this work, we performed our experiments on a magnetically shielded Hall thruster, while virtually all previous research was conducted on unshielded thrusters. We know that there are important differences in the dynamics between shielded and unshielded thrusters beyond the ability to reduce erosion. Most notably, the spoke mode commonly seen in unshielded thrusters is absent in shielded configurations. In addition, the location and amplitude of key features such as peak electric field and electron temperature differ, which can have a major influence on instability development. While we assert that our results should hold in general for thrusters of any configuration, given the ubiquitous nature of anomalous electron transport, it is important to consider that system-level changes to the thruster may alter dynamics of the various processes that could lead to enhanced transport or even

just their relative strength. Furthermore, in the context of future development, our results are most applicable since most new thrusters will almost certainly be built in shielded configurations given the advantages.

Finally, in the process of analyzing the EDI, we have made numerous assumptions and restrictions about the system in order to make it tractable. For example, numerous restrictions were applied to formulate the EDI dispersion relation used in our work, and various assumptions were made that allow the Ritz and Kim method to be applicable to the Hall thruster plasma. These assumptions, and many more discussed throughout this work, are necessary for any progress to be made but bring us a step further away from the true physics, and it is not clear how that might impact our conclusions, even in very subtle ways. Due to the difficulty in designing experiments that do not require such assumptions, many of these questions will have to be left to the realm of numerical simulations as they continue to advance and can better represent the real system.

6.4 Future Work

Our findings in this work prompt several further experimental projects. While we have sufficiently identified the EDI in our wave probe measurements, we must highlight that all these experiments were performed at only one thruster operating condition. There lies the possibility that at some other conditions, the EDI is no longer the dominant instability in the thruster plume, or even if it is ubiquitous for all operating conditions, the nature of its dispersion relation may change in a significant way. Due to the sensitivity of the EDI dispersion relation to a plethora of plasma parameters, such an experiment would require significant time to perform and would yield a mountain of data to process and interpret. Despite these challenges, it is possible that such an analysis might provide significant insight into the nature of the instability and make tremendous progress towards the development of simplified

and predictive Hall thruster models.

Further work may utilize better diagnostics that eliminate much of the uncertainty in invoking so many assumptions in the formulation of our wave-induced transport model. In particular, the use of incoherent Thomson scattering could directly measure the electron velocity distribution function for use in both measuring cross-field transport and calculating the dispersion relation with minimal assumptions. The slope of the EVDF may also provide greater insight into the saturation mechanisms of the EDI, although this would require a much higher velocity resolution than what is available with current Thomson scattering diagnostics.

Finally, as noted in Chapters IV and V, the radial wavenumber of the EDI is of high importance in predicting the EDI dispersion and growth rate, but our attempts to measure the dispersion in this direction using Beall techniques have not been successful. While it is unclear why measurement in this direction has been so unexpectedly challenging, perhaps due to the strong gradient in plasma parameters along the radial axis, a definitive measurement of the radial wavenumber would put to rest several uncertainties involved in this current work. Perhaps advances in coherent Thomson scattering diagnostics that can measure a much wider range of wavenumbers could fill this gap.

BIBLIOGRAPHY

BIBLIOGRAPHY

[1] J C Adam, J P Boeuf, N Dubuit, M Dudeck, L Garrigues, D Gresillon, A Heron, G J M Hagelaar, V Kulaev, N Lemoine, S Mazouffre, J Perez Luna, V Pisarev, and S Tsikata. Physics, simulation and diagnostics of hall effect thrusters. *Physics of Plasmas*, 50(12):124041, 2008.

[2] J C Adam, A Heron, and G Laval. Study of stationary plasma thrusters using two-dimensional fully kinetic simulations. *Physics of Plasmas*, 11(1):295, 2004.

[3] E. Ahedo, J. M. Gallardo, and M. Martınez-Sanchez. Effects of the radial plasma-wall interaction on the Hall thruster discharge. *Physics of Plasmas*, 10(8):3397–3409, 07 2003.

[4] S Barral, K Makowski, Z Peradzyński, N Gascon, and M Dudeck. Wall material effects in stationary plasma thrusters. ii. near-wall and in-wall conductivity. *Physics of Plasmas*, 10(10):4137, 2003.

[5] Serge Barral and Eduardo Ahedo. Low-frequency model of breathing oscillations in hall discharges. *Phys. Rev. E*, 79:046401, Apr 2009.

[6] J M Beall, Y C Kim, and E J Powers. Estimation of wavenumber and frequency spectra using fixed probe pairs. *Physics of Plasmas*, 53:3933, 1982.

[7] J P Boeuf. Tutorial: Physics and modeling of hall thrusters. *Physics of Plasmas*, 121(1):011101, 2017.

[8] J. P. Boeuf and L. Garrigues. Low frequency oscillations in a stationary plasma thruster. *Journal of Applied Physics*, 84(7):3541–3554, 10 1998.

[9] J P Boeuf and L Garrigues. E x b electron drift instability in hall thrusters: Particle-in-cell simulations vs. theory. *Physics of Plasmas*, 25:061204, 2018.

[10] J P Boeuf and A Smolyakov. Preface to special topic: Modern issues and applications of e x b plasmas. *Physics of Plasmas*, 25(6):061001, 2018.

[11] C Boniface, L Garrigues, G J M Hagelaar, J P Boeuf, D Gawron, and S Mazouffre. Anomalous cross field electron transport in a hall effect thruster. *Applied Physics Letters*, 89(16):161503, 2006.

[12] Z A Brown and B A Jorns. Dispersion relation measurements of plasma modes in the near-field plume of a 9-kw magnetically shielded thruster. In *35th International Electric Propulsion Conference*, 2017.

[13] Zachariah Brown and Benjamin Jorns. Experimental measurements of the contribution of plasma turbulence to anomalous collision frequency in a hall thruster. In *AIAA Propulsion and Energy 2021 Forum*, 2021.

[14] Zachariah Brown and Benjamin A. Jorns. Spatial evolution of plasma waves in the near-field of a magnetically shielded hall thruster. In *2018 Joint Propulsion Conference*, 2018.

[15] Zachariah A. Brown and Benjamin A. Jorns. Spatial evolution of small wavelength fluctuations in a hall thruster. *Physics of Plasmas*, 26(11):113504, 2019.

[16] Zachariah A. Brown and Benjamin A. Jorns. Growth and saturation of the electron drift instability in a crossed field plasma. *Phys. Rev. Lett.*, 130:115101, Mar 2023.

[17] David Byers and John Dankanich. A Review of Hall Effect Thruster Facility Effects. In *29th International Electric Propulsion Conference, Ann Arbor, MI IEPC-2009-079*, 2009.

[18] Matthew P. Byrne, Parker J. Robert, and Benjamin A. Jorns. Coupling of electrical and pressure facility effects in hall effect thruster testing. In *37th International Electric Propulsion Conference, Cambridge, MA IEPC-2022-377*, 2022.

[19] J Cavalier, G Lemonie, N amd Bonhomme, S Tsikata, C Honore, and D Gresillon. Hall thruster plasma fluctuations identified as the exb electron drift instability: Modeling and fitting on experimental data. *Physics of Plasmas*, 20:082108, 2013.

[20] Vernon H. Chaplin, Benjamin A. Jorns, Alejandro Lopez Ortega, Ioannis G. Mikellides, Ryan W. Conversano, Robert B. Lobbia, and Richard R. Hofer. Laser-induced fluorescence measurements of acceleration zone scaling in the 12.5 kW HERMeS Hall thruster. *Journal of Applied Physics*, 124(18):183302, 11 2018.

[21] Francis Chen. *Introduction to Plasma Physics and Controlled Fusion*. Plenum Press, New York, NY, 2 edition, 1984.

[22] Shinatora Cho, Kimiya Komurasaki, and Yoshihiro Arakawa. Kinetic particle simulation of discharge and wall erosion of a hall thruster. *Physics of Plasmas*, 20(6):063501, 2013.

[23] Shinatora Cho, Hiroki Watanabe, Kenichi Kubota, Shigeyasu Iihara, Kenji Fuchigami, Kazuo Uematsu, and Ikkoh Funaki. Study of electron transport

in a hall thruster by axial–radial fully kinetic particle simulation. *Physics of Plasmas*, 22:103523, 2015.

[24] E Y Choueiri. Plasma oscillations in hall thrusters. *Physics of Plasmas*, 8:1411, 2001.

[25] S E Cusson, R R Hofer, R B Lobbia, B A Jorns, and A Gallimore. Performance of the h9 magnetically shielded hall thrusters. In *35th International Electric Propulsion Conference*, 2017.

[26] Sarah E. Cusson, Ethan T. Dale, Benjamin A. Jorns, and Alec D. Gallimore. Acceleration region dynamics in a magnetically shielded Hall thruster. *Physics of Plasmas*, 26(2):023506, 02 2019.

[27] Sarah E Cusson, Benjamin A Jorns, and Alec D Gallimore. Non-invasive in situ measurement of the near-wall ion kinetic energy in a magnetically shielded hall thruster. *Plasma Sources Science and Technology*, 28(10):105012, oct 2019.

[28] Ethan Dale. *Investigation of the Hall Thruster Breathing Mode*. PhD thesis, University of Michigan, 2019.

[29] Ethan T. Dale and Benjamin A. Jorns. Non-invasive time-resolved measurements of anomalous collision frequency in a hall thruster. *Physics of Plasmas*, 26(1):013516, 2019.

[30] John W. Dankanich, Mitchell Walker, Michael W. Swiatek, and John T. Yim. Recommended practice for pressure measurement and calculation of effective pumping speed in electric propulsion testing. *Journal of Propulsion and Power*, 33(3):668–680, 2017.

[31] R.C. Davidson and N.A. Krall. Anomalous transport in high-temperature plasmas with applications to solenoidal fusion systems. *Nuclear Fusion*, 17:1313, 1977.

[32] A Ducrocq, J C Adam, and A Heron. High-frequency electron drift instability in the cross-field configuration of hall thrusters. *Physics of Plasmas*, 13(10), 2006.

[33] C L Ellison, Y Raitses, and N J Fisch. Cross-field electron transport induced by a rotating spoke in a cylindrical hall thruster. *Physics of Plasmas*, 11(1):013503, 2012.

[34] Y V Esipchuk and G N Tilinin. Drift instability in a hall-current plasma accelerator. *Sov. Phys. - Tech. Phys. (Engl. Transl.); (United States)*, 21:4, 4 1976.

[35] J M Fife and M Martin-Sanchez. Two-dimensional hybrid particle-in-cell (pic) modeling of hall thrusters. In *Proceedings of the 24th International Electric Propulsion Conference*, 1995.

[36] John Fife, Manuel Martinez-Sanchez, James Szabo, John Fife, Manuel Martinez-Sanchez, and James Szabo. A numerical study of low-frequency discharge oscillations in hall thrusters. In *33rd Joint Propulsion Conference and Exhibit*, 1997.

[37] D. Forslund, R. Morse, C. Nielson, and J. Fu. Electron cyclotron drift instability and turbulence. *The Physics of Fluids*, 15(7):1303–1318, 1972.

[38] L. Garrigues, G. J. M. Hagelaar, C. Boniface, and J. P. Boeuf. Anomalous conductivity and secondary electron emission in Hall effect thrusters. *Journal of Applied Physics*, 100(12):123301, 12 2006.

[39] L. Garrigues, J. Pérez-Luna, J. Lo, G. J. M. Hagelaar, J. P. Boeuf, and S. Mazouffre. Empirical electron cross-field mobility in a Hall effect thruster. *Applied Physics Letters*, 95(14):141501, 10 2009.

[40] S. Peter Gary and J. J. Sanderson. Longitudinal waves in a perpendicular collisionless plasma shock: I. cold ions. *Journal of Plasma Physics*, 4(4):739–751, 1970.

[41] N Gascon, M Dudeck, and S Barral. Wall material effects in stationary plasma thrusters. i. parametric studies of an spt-100. *Physics of Plasmas*, 10(10):4123, 2003.

[42] D. Goebel and I. Katz. *Fundamentals of Electric Propulsion: Ion and Hall Thrusters*. John Wiley and Sons, 2008.

[43] L Grimaud, A Pétin, J Vaudolon, and S Mazouffre. Perturbations induced by electrostatic probe in the discharge of hall thrusters. *Review of Scientific Instruments*, 87:043506, 2016.

[44] J. M. Haas. *Low-perturbation interrogation of the internal and near-field plasma structure of a Hall thruster using a high-speed probe positioning system*. PhD thesis, University of Michigan, 2001.

[45] James Haas, Gregory G. Spanjers, James McFall, and Ronald A. Spores. An investigation of electrostatic probe perturbations on the operational characteristics of a hall thruster and on the measurement of local plasma parameters. In *Proceedings of the 34th AIAA/ASME/SAE/ASEE Joint Propulsion Conference and Exhibit*, 1998.

[46] G. J. M. Hagelaar, J. Bareilles, L. Garrigues, and J. P. Boeuf. Two-dimensional model of a stationary plasma thruster. *Journal of Applied Physics*, 91(9):5592–5598, 04 2002.

[47] G. J. M. Hagelaar, J. L. Bareilles, Garrigues, and J.-P. Boeuf. Role of anomalous electron transport in a stationary plasma thruster simulation. *Journal of Applied Plasma Physics*, 93:67, 2003.

[48] Workshop on ExB Plasmas for Space and Industrial Applications, Toulouse, France, 2017.

[49] R R Hofer, S E Cusson, and R B Lobbia. The h9 magnetically shielded hall thruster. In *35th International Electric Propulsion Conference*, 2017.

[50] Richard R Hofer, Ira Katz, Ioannis G Mikallides, Dan M Goebel, Kristina K Jameson, Regina M Sullivan, and Lee K Johnson. Efficacy of electron mobility models in hybrid-pic hall thruster simulations. In *Proceedings of the 44th AIAA/ASME/SAE/ASEE Joint Propulsion Conference*, 2008.

[51] Wensheng Huang, Alec D. Gallimore, and Richard R. Hofer. Neutral flow evolution in a six-kilowatt hall thruster. *Journal of Propulsion and Power*, 27(3):553–563, 2011.

[52] A. Héron and J. C. Adam. Anomalous conductivity in hall thrusters: Effects of the non-linear coupling of the electron-cyclotron drift instability with secondary electron emission of the walls. *Physics of Plasmas*, 20(8):082313, 2013.

[53] Morozov A I and Savelev V V. Theory of the near-wall conductivity. *Plasma Phys. Rep*, 27:570–575, Jul 2001.

[54] G S Janes and R S Lowder. Anomalous Electron Diffusion and Ion Acceleration in a Low-Density Plasma. *Phys. Fluids*, 9:1115, 1966.

[55] S Janhunen, A Smolyakov, O Chapurin, D Sydorenko, I Kaganovich, and Y Raitses. Nonlinear structures and anomalous transport in partially magnetized e×b plasmas. *Physics of Plasmas*, 25(1):011608, 2018.

[56] S Janhunen, A Sydorenko, D Sydorenko, M Jimenez, I Kaganovich, and Y Raitses. Evolution of the electron cyclotron drift instability in two-dimensions. *Physics of Plasmas*, 25(8):082308, 2018.

[57] Benjamin A Jorns, Dan M Goebel, and Richard R Hofer. Plasma perturbations in high-speed probing of hall thruster discharge chambers: Quantification and mitigation. In *51st AIAA/SAE/ASEE Joint Propulsion Conference*, 2015.

[58] Igor D. Kaganovich, Andrei Smolyakov, Yevgeny Raitses, Eduardo Ahedo, Ioannis G. Mikellides, Benjamin Jorns, Francesco Taccogna, Renaud Gueroult, Sedina Tsikata, Anne Bourdon, Jean-Pierre Boeuf, Michael Keidar, Andrew Tasman Powis, Mario Merino, Mark Cappelli, Kentaro Hara, Johan A. Carlsson, Nathaniel J. Fisch, Pascal Chabert, Irina Schweigert, Trevor Lafleur, Konstantin Matyash, Alexander V. Khrabrov, Rod W. Boswell, and Amnon Fruchtman. Physics of e x b discharges relevant to plasma propulsion and similar technologies. *Physics of Plasmas*, 27(12):120601, 2020.

[59] I Katz, A L Ortega, B A Jorns, and I G Mikellides. Growth and saturation of ion acoustic waves in hall thrusters. In *52nd AIAA Joint Propulsion Conference*, 2016.

[60] Ira Katz, Vernon H Chaplin, and Alejandro L Ortega. Numerical studies of hall thruster acceleration region electron transport. In *2018 Joint Propulsion Conference, AIAA Propulsion and Energy Forum*, 2018.

[61] Justin W. Koo and Iain D. Boyd. Computational model of a hall thruster. *Computer Physics Communications*, 164(1):442–447, 2004. Proceedings of the 18th International Conferene on the Numerical Simulation of Plasmas.

[62] Justin W. Koo and Iain D. Boyd. Modeling of anomalous electron mobility in Hall thrusters. *Physics of Plasmas*, 13(3):033501, 03 2006.

[63] T Lafleur, S D Baalrud, and P Chabert. Theory for the anomalous electron transport in hall effect thrusters: I. insights from particle-in-cell simulations. *Physics of Plasmas*, 23:053502, 2016.

[64] T Lafleur, S D Baalrud, and P Chabert. Theory for the anomalous electron transport in hall effect thrusters: Ii. kinetic model. *Physics of Plasmas*, 23:053503, 2016.

[65] T. Lafleur and P. Chabert. The role of instability-enhanced friction on 'anomalous' electron and ion transport in hall-effect thrusters. *Plasma Sources Sci. Technol.*, 27:015003, 2017.

[66] T Lafleur, P Chabert, and A Bourdon. Anomalous electron transport in hall-effect thrusters: Comparison between quasilinear kinetic theory and particle-in-cell simulations. *Physics of Plasmas*, 25:061202, 2018.

[67] A Lazurenko, G Coduti, S Mazouffre, and G. Bonhomem. Dispersion relation of high-frequency plasma oscillations in hall thrusters. *Physics of Plasmas*, 15:034502, 2008.

[68] Andrei A. Litvak and Nathaniel J. Fisch. Rayleigh instability in Hall thrusters. *Physics of Plasmas*, 11(4):1379–1383, 03 2004.

[69] Andrei A Litvak, Yevgeny Raitses, and Nathaniel J Fisch. Experimental studies of high-frequency azimuthal waves in hall thrusters. *Physics of Plasmas*, 11:1701, 2004.

[70] Robert B. Lobbia and Brian E. Beal. Recommended practice for use of langmuir probes in electric propulsion testing. *Journal of Propulsion and Power*, 33(3):566–581, 2017.

[71] Thomas Marks and Benjamin Jorns. Modeling anomalous electron transport in Hall thrusters using surrogate methods. In *37th International Electric Propulsion Conference, Cambridge, MA IEPC-2022-344*, 2022.

[72] S. Mazouffre, D. Gawron, and N. Sadeghi. A time-resolved laser induced fluorescence study on the ion velocity distribution function in a Hall thruster after a fast current disruption. *Physics of Plasmas*, 16(4):043504, 04 2009.

[73] M S McDonald and A D Gallimore. Parametric investigation of the rotating spoke instability in hall thrusters. In *32nd International Electric Propulsion Conference*, 2011.

[74] N B Meezan, W A Hargus, and M A Cappelli. Anomalous electron mobility in a coaxial hall discharge plasma. *Physics Review E*, 62(2):026410, 2001.

[75] Ioannis G. Mikellides, Benjamin Jorns, Ira Katz, and Alejandro Lopez Ortega. Hall2de simulations with a first-principles electron transport model based on the electron cyclotron drift instability. In *52nd AIAA/SAE/ASEE Joint Propulsion Conference*, 2012.

[76] Ioannis G Mikellides, Ira Katz, Richard Hofer, and Dan Goebel. Magnetic shielding of walls from the unmagnetized ion beam in a hall thruster. *Applied Physics Letters*, 102(2):023509, 2013.

[77] Ioannis G Mikellides, Alejandro Lopez Ortega, Vernon H Chaplin, and John Steven Snyder. Facility pressure effects on a hall thruster with an external cathode, ii: theoretical model of the thrust and the significance of azimuthal asymmetries in the cathode plasma. *Plasma Sources Science and Technology*, 29(3):035010, mar 2020.

[78] Ioannis G Mikelliedes, Ira Katz, Richard R Hofer, and Dan M Goebel. Design of a laboratory hall thruster with magnetically shielded channel walls, phase iii: Comparison of theory with experiment. In *48th AIAA/ASME/SAE/ASEE Joint Propulsion Conference and Exhibit*, 2012.

[79] B Nold, T T Ribeiro, Ramisch, Z Huang, H W Müller, B D Scott, and U Stroth. Influence of temperature fluctuations on plasma turbulence investigations with langmuir probes. *New Journal of Physics*, 14:063022, 2012.

[80] David Y. Oh, Steve Collins, Tracy Drain, William Hart, Travis Imken, Kristina Larson, Danielle Marsh, Dhack Muthulingam, John Steven Snyder, , Denis Trofimov, Linda T. Elkins-Tanton, Ian Johnson Peter Lord, and Zack Pirk. Development of the psyche mission for nasa's discovery program. In *36th International Electric Propulsion Conference, Vienna, Austria IEPC-2019-192*, 2019.

[81] A L Ortega, I Katz, and V H Chaplin. A first-principles model based on saturation of the electron cyclotron drift instabiity for electron transport in hydrodynamic simulations of hall thruster plasmas. In *35th International Electric Propulsion Conference*, 2017.

[82] Ch P. Ritz, E J. Powers, and Roger Bengtson. Experimental measurement of three-wave coupling and energy cascading. *Physics of Fluids B: Plasma Physics*, 1, 01 1989.

[83] J Pérez-Luna, G J M Hagelaar, L Garrigues, and J P Boeuf. Method to obtain the electric field and the ionization frequency from laser induced fluorescence measurements. *Plasma Sources Science and Technology*, 18(3):034008, jul 2009.

[84] Astrid L. Raisanen, Kentaro Hara, and Iain D. Boyd. Two-dimensional hybrid-direct kinetic simulation of a Hall thruster discharge plasma. *Physics of Plasmas*, 26(12):123515, 12 2019.

[85] Ch.P. Ritz and E.J. Powers. Estimation of nonlinear transfer functions for fully developed turbulence. *Physica D: Nonlinear Phenomena*, 20(2):320–334, 1986.

[86] J S. Kim, Roger Durst, Ray Fonck, Eduardo Fernandez, Andrew Ware, and P W. Terry. Technique for the experimental estimation of nonlinear energy transfer in fully developed turbulence. *Physics of Plasmas*, 3:3998–4009, 11 1996.

[87] R. Z. Sagdeev and A. A. Galeev. *Nonlinear Plasma Theory*. New York: Benjamin, 1969.

[88] Michael J. Sekerak, Ben Longmier, Alec Gallimore, Wensheng Huang, Hani Kamhawi, Richard R. Hofer, Benjamin Jorns, and James E. Polk. Mode transitions in magnetically shielded hall effect thrusters. In *50th AIAA/ASME/SAE/ASEE Joint Propulsion Conference*, 2014.

[89] M. Sengupta and A. Smolyakov. Mode transitions in nonlinear evolution of the electron drift instability in a 2d annular e x b system. *Physics of Plasmas*, 27:022309, 2 2020.

[90] Natalia Sternberg and Valery Godyak. Plasma density perturbation caused by probes at low gas pressure. *Physics of Plasmas*, 24(9):093504, 2017.

[91] T. H Stix. *Waves in Plasmas*. AIP Press, 1992.

[92] D. G Swanson. *Plasma Waves*. Academcic Press, Inc., 1989.

[93] F. Taccogna and L. Garrigues. Latest progress in Hall thrusters plasma modelling. *Reviews of Modern Plasma Physics*, 3(1):12, July 2019.

[94] F. Taccogna, S. Longo, M. Capitelli, and R. Schneider. Particle-in-cell simulation of stationary plasma thruster. *Contributions to Plasma Physics*, 47(8-9):635–656, 2007.

[95] Francesco Taccogna, Pierpaolo Minelli, Zahra Asadi, and Guillaume Bogopolsky. Numerical studies of the ExB electron drift instability in hall thrusters. *Plasma Sources Science and Technology*, 28(6):064002, jun 2019.

[96] F Taccognam, R Schneider, S Longo, and M Capitelli. Kinetic simulations of a plasma thruster. *Plasma Sources Sci. Technol.*, 17:024003, 2008.

[97] Arash Tavassoli, Andrei Smolyakov, Magdi Shoucri, and Raymond J. Spiteri. Nonlinear regimes of the electron cyclotron drift instability in vlasov simulations. *Physics of Plasmas*, 29(3):030701, 2022.

[98] G N Tilinin. High-frequency plasma waves in a hall accelerator with an extended acceleration zone. *Sov. Phys. - Tech. Phys. (Engl. Transl.); (United States)*, 22:8, 8 1977.

[99] S Tsikata. *Small-Scale Electron Density Fluctuations in the Hall Thruster, Investigated By Collective Light Scattering*. PhD thesis, Ecole Polytechnique X, 2009.

[100] S Tsikata, C Honore, N Lemoine, and D M Gresillon. Three-dimensional structure of electron density fluctuations in the hall thruster plasma: E x b mode. *Physics of Plasmas*, 17(11):112110, 2010.

[101] S Tsikata, N Lemoine, V Pisarev, and D M Gresillon. Dispersion relation of electron density fluctuations in a hall thruster plasma, observed by collective light scattering. *Physics of Plasmas*, 16(3):033506, 2009.